DIPLOMA THESIS

SEISMIC IMAGING AND SCATTERING IN HETEROGENEOUS MEDIA - NUMERICAL STUDY AND ANALYTICAL APPROACHES

written by

Lasse Rabenstein

Department of Geophysics[1]
Institute of Geological Sciences
Freie Universität Berlin

March 3, 2006

---

[1] Malteserstr. 74-100, 12249 Berlin, Germany

Abstract

The purpose of this thesis is to improve the understanding of wave propagation and scattering in statistically heterogeneous isomeric and anisomeric media in order to ease the interpretation of frequency filtered and migrated seismogram sections.

For this purpose we performed numerical studies of seismic wave propagation in models containing a deep reflector in the presence of a heterogeneous overburden. Furthermore an analytical solution of the backscattering coefficient for anisomeric heterogenous media is given.
Different heterogeneous overburdens are realized by exponential and Gaussian 'Auto Correlation Functions'. The numerical simulation is based on a finite difference code and outputs synthetic seismogram time sections recorded at the model surface. We processed the synthetic time section in order to obtain for different frequency ranges a set of 'Kirchhoff' migrated depth sections. We analyse the depth sections in terms of image quality of the deep reflector and in terms of scattered energy in the image of the heterogeneous zone. The scattering energy is simply determined by the average squared amplitude in a window which borders the heterogeneous zone. A comparison with analytical results for the scattering coefficient, obtained by the first order Born approximation, concludes this work.

We notice that the size and shape of images of heterogeneities is strongly dependent on frequency. The quality of a reflectorimage below such heterogeneities depends mainly on two parameters of the overburden: the standard deviation of the velocity fluctuation and the ratio of horizontal to vertical correlation length. For large ratios the heterogeneities are considered anisomeric and the deep reflector is distinctly imaged. With increasing standard deviation and decreasing ratio the reflector image becomes diffuse and finally it disappears entirely. In strongly anisomeric media this behaviour is frequency independent but in isomeric media we can improve the reflector image for frequencies with according wavelengths smaller than the correlation length. The numerically determined scattering energy is not correlated with the analytical solution of the scattering coefficient. The part of scattered waves, which caused the image of the heterogeneous overburden, is too small to separate it from other effects like common reflections. The Born approximation predicts strong forward scattering in anisomeric cases, where the reflector is visible, and strong backscattering in isomeric cases, where the image of the reflector is of bad quality. A detailed spectral analysis reveals self averaging effects in the power spectra of sections recorded in anisomeric media.

Contents

Chapter 1

Introduction

In this thesis we use a combination of numerical and analytical approaches in order to understand the problems of imaging and the processes of scattering in statistically heterogeneous isomeric and anisomeric media. In the first chapter we introduce the four main focuses and explain the motivation and structure of this work.

1.1 Main Focuses of this work

Imaging

Seismic imaging or migration is the process of transforming the near surface information (i.e. ground movement) recorded by seismometers into images of subsurface structures. Seismic energy propagates from a source through the subsurface, where it is scattered, reflected and refracted at structures of different densities or seismic velocities, to an array of seismometers. The seismometers record the travel time from the source to the receiver and hence provide information about the velocity structures in the subsurface, which can be correlated to the geologic structures. In unmigrated seismogram sections the data are gathered with respect to the observation point. The challenge in seismic migration is to locate and identify the boundaries where the energy is reflected and refracted. Over the last decades several migration techniques have been developed (e.g. Yilmaz, 1987; Sheriff and Geldart, 1999). They are differentiated in geometrical methods and methods based on the solution of the wave equation (e.g. 'Frequency Wavenumber migration' (Gazdag, 1978) or 'Finite Difference Migration' (Claerbout, 1970) or

'Kirchhoff Migration' (Schneider, 1978)). All of these methods propagate the recorded signal back in time and space to the appropriate subsurface location. In this thesis we use the method of 'Kirchhoff prestack depth migration' which is based on an integral solution of the wave equation.

Reflection Image Spectroscopy - RIS

As long as the considered medium is homogeneous, all migration techniques provide similar results. In reality, the earth is in most cases highly heterogeneous. Scales of heterogeneity in the earth's crust range from several centimetres to hundreds of kilometres, which causes significant frequency dependent scattering (Sato and Fehler, 1998). Consequently, seismic images of the earth's crust vary for different frequencies and we can no longer assume a frequency independent wave propagation. Therefore our approach is to generate for different frequency ranges a series of migrated depth sections. This approach is referred to as 'Reflection Image Spectroscopy' (RIS)(Buske et al., 2004; Yoon, 2005). The RIS technique enables the characterisation of seismic images in terms of scatterer concentration and its length scales.

Finite Difference modelling of wave propagation in heterogeneous media

The Finite Difference (FD) method is suitable for solving differential equations in a numerical way. The numerical solution of the elastodynamic wave equation enables a complete simulation of a propagating elastic wave field in a given medium (e.g. Virieux, 1986; Saenger, 2000). We have constructed models containing a deep reflector in the presence of a heterogeneous overburden. The heterogeneous zone in the model is defined by velocity fluctuations. In order to give the heterogeneities a known statistical distribution a certain 'Auto Correlation Function' (ACF) is used. Heterogeneities with an exponential and a Gaussian ACF are considered in this thesis. In order to control the statistics of the heterogeneities we vary three parameters of the ACF, the standard deviation as well as the correlation lengths in horizontal (x) direction and vertical (z) direction. The standard deviation σ defines the amplitude of the fluctuations and the correlation lengths a_x and a_z the scale of the heterogeneities in x and z direction. For $a_x \neq a_z$ our medium is referred to as anisomeric.

Seismic scattering

The importance of scattering in seismic wave propagation was recognised more than 35 years ago by focusing the interests on coda waves in seismological records. The existence of coda waves is commonly accepted as direct evidence for seismic scattering at heterogeneities within the earth (Sato and Fehler, 1998). Scattering is classified into different scattering regimes according to the ratio of the wavelength to the size of the heterogeneity (Wu and Aki, 1988). If the size is comparable with the wavelength Mie scattering dominates. Scattering on heterogeneities much smaller than the wavelength is referred to as Rayleigh scattering and for heterogeneities much larger than the wavelength the laws of geometrical optics are valid. Mie scattering is also referred to as resonance scattering, as the strongest scattering can be observed for this regime. Many theoretical approaches to the description of scattering processes exist (Ishimaru, 1978). In this work we use the single scattering approximation to the wave equation, based on the Born approximation for elastic media. With this approach Wu and Aki (1985) derived a general ensemble averaged formulation for the scattering power which can be applied to both, isomeric and anisomeric random media. In this thesis the approach is used to understand the effects which are observed in the computed wave fields.

1.2 Motivation of this work

The purpose of this thesis is to improve the understanding of wave propagation and scattering in statistically heterogeneous isomeric and anisomeric media in order to ease the interpretation of RIS seismogram sections.

The RIS method has already been applied to the ANCORP reflection seismic data set from the Central Andes (ANCORP Working Group, 1999; Buske et al., 2002) in the work of Yoon (2005). We perform numerical simulations in a model with a geometry based on the results of the ANCORP profile, including a deep reflector in the presence of a heterogeneous overburden. We record the propagated wave field at the model surface to simulate a situation similar to real reflection seismic experiments. RIS is applied to the synthetic seismogram sections in order to obtain, for several frequency ranges, Kirchhoff migrated depth sections. One focus is on the quality of the image of the deep reflector for different frequencies in dependence on the statistical parameters of the heterogeneous overburden. Another focus is on the energy, which is scattered within the heterogeneous zone in the depth image. The idea is to find a connection between this energy for different frequency ranges and the horizontal correlation length of the heterogeneous medium. Furthermore we use known approaches, based on the single scattering Born approximation, in order to derive a solution of the scattering coefficient for an arbitrary isomeric or anisomeric medium. The idea is to find similarities between the backscattering coefficient and the energy in the image of the heterogeneous zone.

1.3 Structure of this work

Fig. 1.1 gives an overview about the structure of this thesis.

Chapter 2.1. describes the geometry of the used models in detail including the model parameters and the characteristics of the heterogeneous medium. The concept of 'Auto Correlation functions' (ACF) and their usage for a quantitative characterisation of the medium is described. Furthermore basics of the forward FD modelling code are summarised and illustrated with the help of wave field snapshots. The chapter concludes with a presentation of synthetic seismogram sections for different media.

Chapter 2.2. introduces the processing steps which are necessary for the application of the RIS method. Among information about features of the used bandpass filters, a 'whitening' procedure to correct for the actual frequency bandwidth of the used source wavelet will be explained. The heterogeneous medium and the scattering phenomena which occur will be discussed as a linear filter which affects the input wavelet. Then a short introduction to Kirchhoff prestack depth migration is given, which we apply to transform the filtered and whitened seismogram time sections into the corresponding migrated depth sections. Special attention will be paid to the quality of the image in relation to the statistical parameters of the heterogeneous overburden.

In **Chapter 2.3.** we analyse the migrated RIS sections in order to gain insights into the energy distribution within the image of the heterogeneous overburden for different frequency ranges. In detail we obtain the average amplitude square of an ensemble of samples located in the image of the heterogeneous overburden.

In **Chapter 3.** we give an overview about different scattering regimes. We introduce the Born approximation as a suitable approach for an analytical solution of the scattering coefficient. A detailed derivation of this solution for anisomeric 2D media is presented and discussed referring to the numerical studies. We illustrate the solution of the scattering coefficient for heterogeneous media similar to those in the numerical part of this thesis. A comparison between numerical and analytical results concludes this chapter.

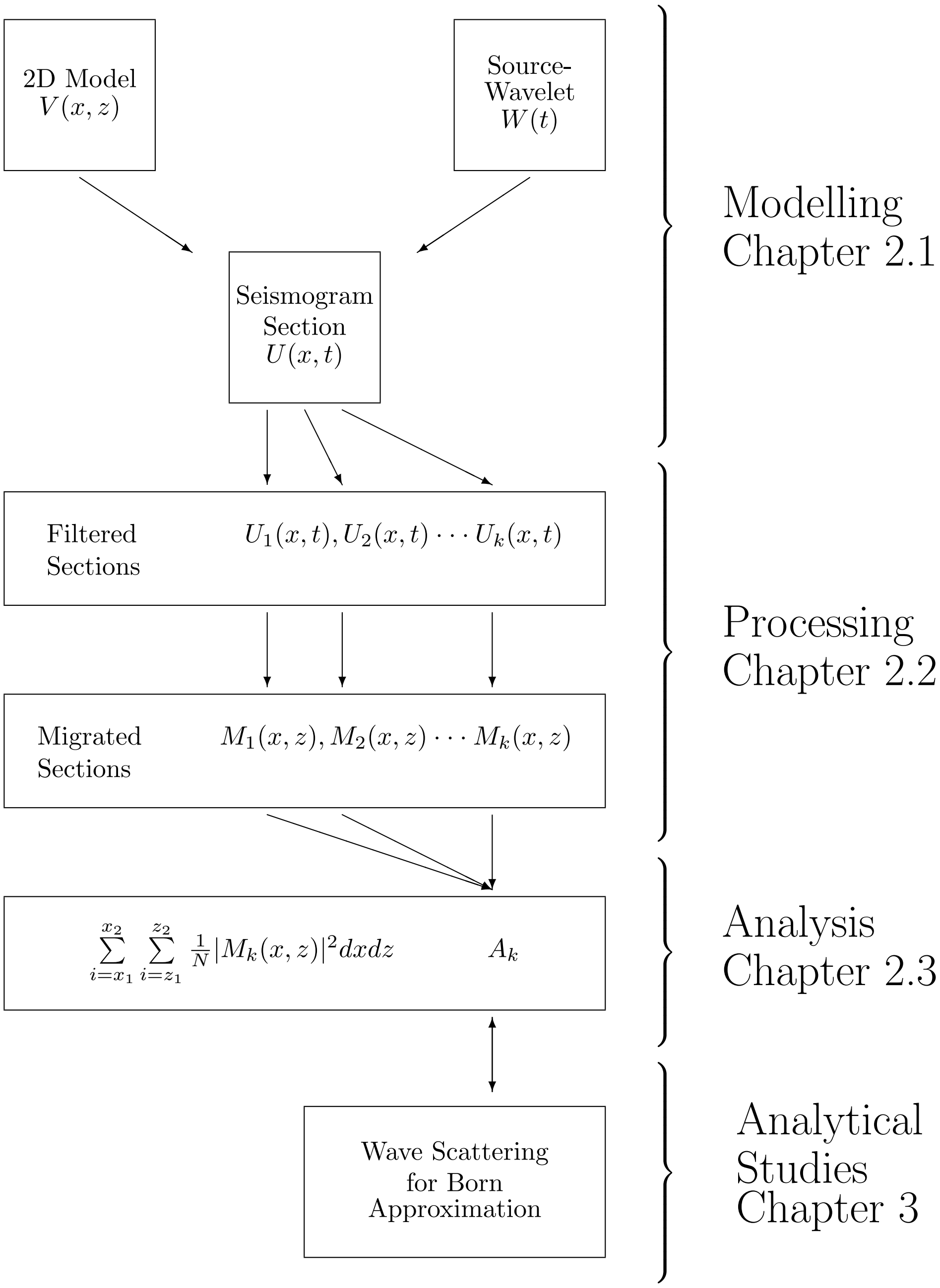

Figure 1.1: Workflow diagram: In chapter 2.1 2D models are created and a source wavelet functions as a model input in order to produce synthetic seismogram sections. In chapter 2.2 these sections are frequency filtered by k different band pass filters. All k filtered time sections are migrated to k depth sections. In chapter 2.3 we determine scattering energies from the depth sections in order to compare them with analytical results of the scattering coefficient in chapter 3.

Chapter 2

Numerical Studies

2.1 Modeling

2.1.1 Model Geometry

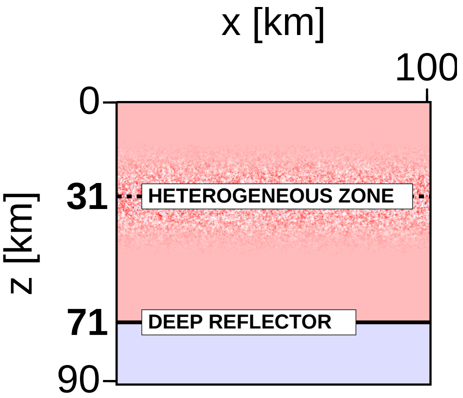

Figure 2.1: Schematical image of the model geometry

The model geometry is set up according to the ANCORP data set in order to take into account the imaging problems which have occurred there. A boundary at 71 km depth represents the subducted plate as a sharp reflector and a heterogeneous zone centered around 31 km depth simulates intercrustal inhomogeneities (Fig. 2.1). The dimensions of the model are 101 km in x-direction and 91 km in z-direction. The upper layer has a P-wave velocity of 6 km/s and the lower layer of 8 km/s. With a v_p/v_s ratio of $\sqrt{3}$ the S-wave velocity is 3.564 km/s for the upper part and 4.618 km/s for the lower part, respectively. In the heterogeneous zone the velocity fluctuates around the homogeneous background velocity (see section 2.1.2.). The medium density was determined after the empirical Nafe-Drake relation (Ludwig et al., 1970):

$$\rho = 1.755 + 0.155 v_p \; [g/cm^3]. \tag{2.1}$$

According to equation (2.1) the density for the upper layer is $\rho_1 = 2685$ kg/m^3 and $\rho_2 = 2995$ kg/m^3 for the lower layer respectively.

2.1.2 Random Media

The heterogeneous zone consists of a constant homogeneous background velocity V_0, in our case $V_0 = 6$ km/s for P-waves, and a fluctuating velocity δV. For a certain position $\vec{r}$ the velocity is given by

$$V(\vec{r}) = V_0 + \delta V(\vec{r}) = V_0[1 + \xi(\vec{r})] \tag{2.2}$$

where ξ is the fractional velocity fluctuation. We assume that the average fluctuation over all positions is zero:

$$\langle \xi(\vec{r}) \rangle = 0 \tag{2.3}$$

and consequently the average velocity is equal to the background velocity:

$$V_0 = \langle V(\vec{r}) \rangle. \tag{2.4}$$

Furthermore the velocity fluctuation ξ was multiplied with a depth dependent weighting factor

$$\tilde{\xi}(z) = \xi(z) \cdot exp[-\frac{(z - z_0)^2}{A^2}] \tag{2.5}$$

where z_0 and A are 31 km and 20 km respectively. Equation (2.5) is a Gaussian function. Therefore A can be considered as the normal deviation and z_0 as the expectation value. For $z = z_0 = 31$ km we obtain $\tilde{\xi} = \xi$. The full width at half maximum (FWHM) is an expression of the extent of $\tilde{\xi}(z)$, given by the difference between the two values of z at which $\tilde{\xi}(z)$ is equal to half of its maximum value, and is FWHM $= \sqrt{2\ln 2}\ A \approx 23.548$ km. The first step to generate $\xi(\vec{r})$ is to produce a random field based on a random function $F(\vec{k})$. $F(\vec{k})$ was realized by a random number generator (Press et al., 1993). The period of $F(\vec{k})$ is of the order of 10^8. Furthermore we want to give $\xi(\vec{r})$ a defined distribution. Therefore we must introduce the concept of 'Auto Correlation Functions' (ACF) and 'Power Spectral Density Functions'

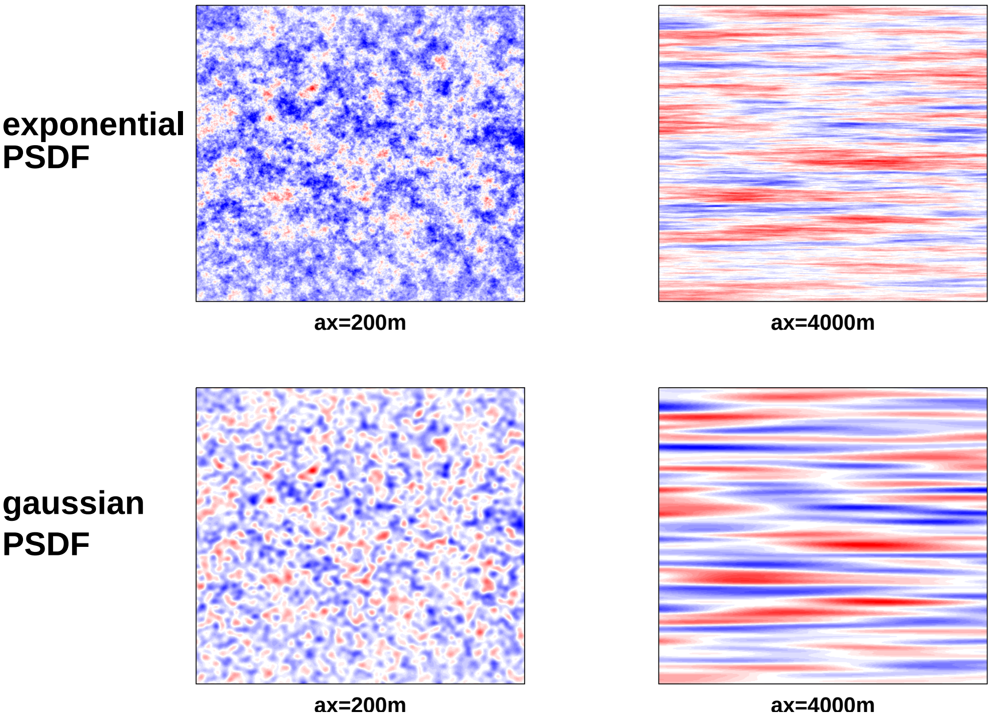

Figure 2.2: Examples for Gaussian and exponentially distributed random media for different correlation lengths a_x=200m and a_x=4000m. a_z is constantly 200m

(PSDF). The ACF can be used as a statistical measure of the spatial scale and the magnitude of heterogeneities in the medium. It is defined by

$$R(\vec{r}) = \langle \xi(\vec{r'})\xi(\vec{r'}+\vec{r})\rangle \tag{2.6}$$

It denotes the average over an ensemble of fluctuation values. We assume that $R(\vec{r})$ is stationary which means that it is independent of $\vec{r'}$. For the creation of $\xi(\vec{r})$ we use the Fourier transform of the ACF which is the fluctuation spectrum or the PSDF or $P(\vec{k})$

$$P(\vec{k}) = \iint R(\vec{r})e^{ik\vec{r}}dxdz \tag{2.7}$$

where $\vec{k}$ is the wavenumber vector. $\xi(\vec{r})$ is obtained by the Fourier transform of the product of $P(\vec{k})$ and $F(\vec{k})$:

$$\xi(\vec{r}) = \frac{1}{2\pi^2} \iint F(\vec{k}) \sqrt{P(\vec{k})} e^{-i\vec{k}\vec{r}} dk_x dk_z \tag{2.8}$$

As R is proportional to ξ^2 the same holds for P. Hence the square root of P is necessary in equation (2.8).

There are several forms of PSDF. In this thesis random media with two different PSDF are used (see Fig. 2.2):

1. Exponential:

$$P^{2D}_{exp}(k_x, k_z) = \frac{\sigma^2(a_x a_z)}{2\pi(1 + k_x^2 a_x^2 + k_z^2 a_z^2)^{\frac{3}{2}}} \tag{2.9}$$

2. Gaussian:

$$P^{2D}_{gauss}(k_x, k_z) = \frac{\sigma^2(a_x a_z)}{4\pi} e^{-\frac{k_x^2 a_x^2 + k_z^2 a_z^2}{4}} \tag{2.10}$$

where σ is the standard deviation of the velocity fluctuation and takes values between 0 and 1, a_x is the correlation distance in x-direction, a_z is the correlation distance in z-direction and k_x and k_z are the x and z components of $\vec{k}$. The correlation distance is a measure of the spatial variation of heterogeneities. The a_x/a_z ratio determines the grade of anisometry within the medium. A Gaussian PSDF describes media with long wavelength components and an exponential PSDF characterises media dominated by short wavelengths. In this thesis a_z is 200 m and a_x varies from $50 - 6000$ m. For large a_x the model can be considered as a quasi horizontally layered medium (1D) (Fig. 2.2).

2.1.3 Model Setup

The model dimension (see Chapter 2.1.1.) is realized by a total amount of 4000 grid points in x-direction and 3640 grid points in z-direction. The horizontal and vertical distance between the grid points is 25 m. All model parameters are illustrated in Fig. 2.3. On every grid point we define three parameters: the density ρ, the P-wave velocity V_p and the S-wave velocity V_s. For the excitation of a propagating wave field we use a pressure point source. This source is located at x=37.5 km and z=1.025 km. Due to the pressure point source only P-waves are radiated. Nevertheless S-waves will be created as well, due to conversion scattering. On 252 positions on the right hand side of the source point, between x=37.7 km and x=62.9 km every 100 m, we

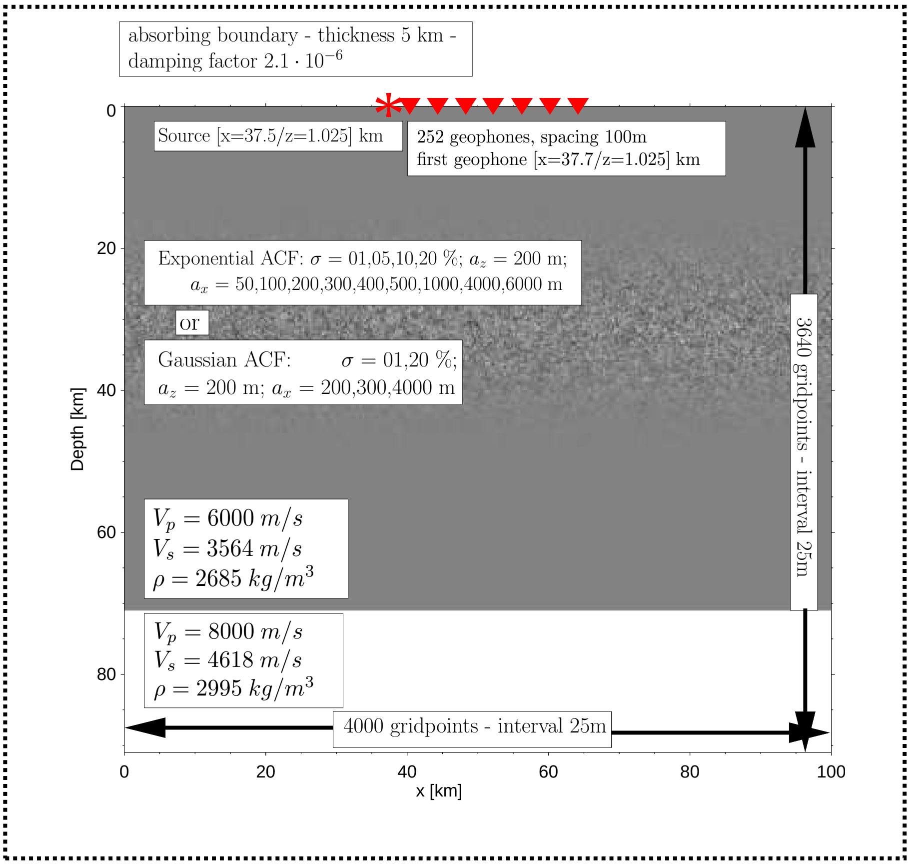

Figure 2.3: Model overview and the most important parameters

record the displacement in x and z direction. For further studies in this thesis we only consider the z-component of the displacement. Furthermore we use absorbing boundary conditions. The model is surrounded by a 5 km thick zone (200 grid points), where the wave field is damped by a factor of $2.1 * 10^{-6}$. This does not avoid boundary reflections completely, but is sufficient for this studies. The model setup is the same throughout this thesis.

2.1.4 FD computation

The wave field propagation was calculated by solving a system of isotropic elastodynamic wave equations:

$$\rho \frac{\partial^2 u_x}{\partial t^2} = \frac{\partial \sigma_{xx}}{\partial x} + \frac{\partial \sigma_{xz}}{\partial z} + \frac{\partial \Delta \sigma_{xx}}{\partial x},$$

$$\rho \frac{\partial^2 u_z}{\partial t^2} = \frac{\partial \sigma_{xz}}{\partial x} + \frac{\partial \sigma_{zz}}{\partial z} + \frac{\partial \Delta\sigma_{zz}}{\partial z} \qquad (2.11)$$

with u_x, u_z as the components of the displacement vector and $\sigma_{xx}, \sigma_{zz}, \sigma_{xz}$ as the components of the stress tensor. $\Delta\sigma_{xx}$ and $\Delta\sigma_{zz}$ are the normal stresses added by the pressure point source. Furthermore we set $\Delta\sigma_{xx} = \Delta\sigma_{zz}$. The excitation of the pressure point source is realized by the following equation:

$$\Delta\sigma_{zz}(t) = -2A(t - t_0)e^{-\alpha(t-t_0)^2} \qquad (2.12)$$

where A=100, α=4000 and t_0=0.04. The shape and the parameters of this input signal are shown in Fig. 2.4. The input signal has a total duration of 0.09 s and a sampling interval of 10^{-3} s. The dominant frequency of the wavelet is about 13 Hz. For the upper layer this results in a dominant P-wavelength of 480 m.

Displacement and stress are related by Hooke's law

$$\begin{aligned} \sigma_{xx} &= (\lambda + 2\mu)\frac{\partial u_x}{\partial x} + \lambda \frac{\partial u_z}{\partial z}, \\ \sigma_{zz} &= (\lambda + 2\mu)\frac{\partial u_z}{\partial z} + \lambda \frac{\partial u_x}{\partial x}, \\ \sigma_{xz} &= \mu \left(\frac{\partial u_x}{\partial z} + \frac{\partial u_z}{\partial x} \right) \end{aligned} \qquad (2.13)$$

where λ and μ are the elastic Lamé parameters.

For the numerical solution of equation (2.11) a 'Finite Difference' (FD) scheme was used (Virieux, 1986). The basic idea is to discretise the wave

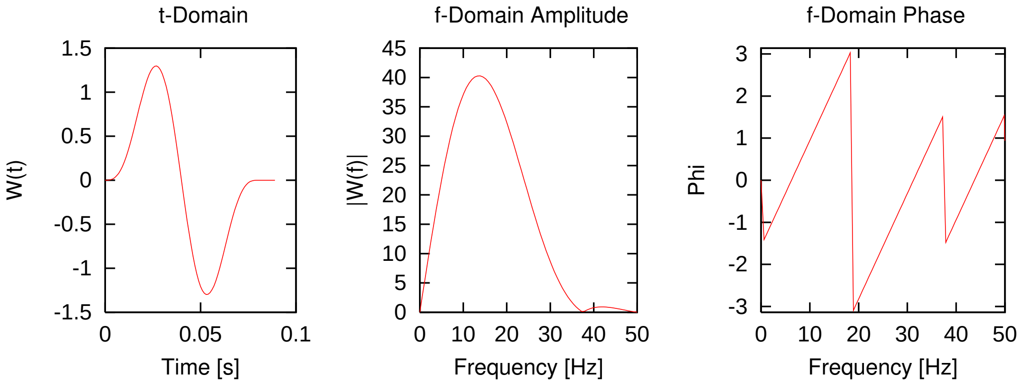

Figure 2.4: The signal in time domain and frequency domain (amplitude and unwrapped phase spectrum.

equation with the corresponding parameters $\rho(\vec{r})$, $\mu(\vec{r})$, $\lambda(\vec{r})$ and $u(\vec{r},t)$ in space and time. The spatial discretisation is realized by the input model grid. On every grid point we define ρ, μ and λ. Since we have seismic velocities as the input parameters instead of Lamé parameters we have to consider the following relations:

$$v_p^2 = \frac{\lambda + 2\mu}{\rho} \quad \text{and} \quad v_s^2 = \frac{\mu}{\rho}. \tag{2.14}$$

Furthermore we have to discretise the spatial derivative of the displacement field and of the stress tensor by determining a FD differential operator D defined by

$$\frac{\partial}{\partial r} := D_r \tag{2.15}$$

A simple example for a first order partial derivative would be the following:

$$D_x u(x,y,z,t) := \frac{1}{\Delta x}[u(x+\Delta x, y, z, t) - u(x,y,z,t)] \tag{2.16}$$

D_x differs from the analytical derivative due to a finite Δx. The error depends mainly on the number of neighbouring grid points we include in our operator. Equation 2.16 shows an operator of the first order which takes into account only one neighbouring sample in the forward direction. Higher accuracy can be obtained by using a centered scheme including more than two samples in the forward and backward direction. For the numerical simulation in this thesis a staggered grid (Saenger, 2000) and a spatial differential operator of the eighth order has been used, in both directions, x and z. For the calculation of the time derivative we obtain a discrete expression for the displacement field at a time $t + \Delta t$. An expansion of $u(\vec{r}, t + \Delta t)$ into a Taylor series yields

$$u(\vec{r}, t+\Delta t) = 2u(\vec{r},t) - u(\vec{r}, t-\Delta t) + \Delta t^2 \frac{\partial^2 u(\vec{r},t)}{\partial t^2} \tag{2.17}$$

with

$$\frac{\partial^2 u(\vec{r},t)}{\partial t^2} = \frac{1}{\rho(\vec{r})} D_r \sigma_{ij}(\vec{r},t) \tag{2.18}$$

where σ_{ij} denotes the stress tensor. Equation 2.17 is a Taylor expansion of the second order, which is commonly sufficient and is used in this thesis. As we can see the only information necessary is the displacement field at the times t and $t - \Delta t$. The FD scheme executes the following work flow every time step:

1. Calculation of $\frac{\partial^2 u(\vec{r},t)}{\partial t^2}$ including spatial derivatives and the input signal.

2. Calculation of $u(\vec{r}, t + \Delta t)$.
3. Rearrange memory: $u(\vec{r}, t - \Delta t) := u(\vec{r}, t)$ and $u(\vec{r}, t) := u(\vec{r}, t + \Delta t)$.

For a duration of 30 s and a sampling interval of 0.001 s this work flow is executed 30.000 times for every model realization. The calculation of $u(\vec{r}, t)$ in every time step is executed for every grid point.

Due to the approximative character of the differential operator and the Taylor expansion, there are two more facts that have to be considered for obtaining correct results, the *stability criterion* and *numerical dispersion.* For an inadequate combination of Δt and Δx one can observe an exponential increase of amplitudes with every time step. An adequate combination can be obtained by the stability criterion which depends on the chosen FD scheme. For the staggered grid it is as follows (Virieux, 1986; Levander, 1988)

$$v_p(\frac{\Delta t}{\Delta h}) \leq 1/(\sqrt{3}\sum_{k=1}^{n} |c_k|). \tag{2.19}$$

In this equation $|c_k|$ denote the difference coefficients (Holberg, 1987) and Δh denotes the grid spacing. Numerical dispersion is a measure for the phase error, which can not be eliminated completely. To minimise it one has to define enough samples per wavelength, otherwise the calculated velocity differs significantly from the velocity defined in the input model. A commonly used dispersion criteria is

$$\frac{v_{min}/f_{max}}{\Delta h} > 3.0. \tag{2.20}$$

With $v_{min} = 4800$ m/s, $f_{max} = 30$ Hz and $\Delta h = 25$ m the used setup lies within the dispersion criteria (6.4 > 3.0) and a dispersion correction is not necessary.

In addition to seismogram sections the FD program outputs snapshots of the propagating wave field $u(\vec{r}, t)$. Fig. 2.5 and 2.6 display snapshots for times of t=10, t=20 and t=30 seconds. We display snapshots for an isomeric model (a_x=200m, a_z=200m) and for an anisomeric model (a_x=4000m, a_z=200m) for an exponential as well as a Gaussian PSDF. The following paragraph gives a description of Fig. 2.5 and 2.6. All images are equally scaled.

Description of Fig. 2.5 (exponential medium):

10 seconds

anisomeric case: In the upper left corner a snapshot of the wave field after 10 seconds of propagation in a strong anisomeric media is illustrated. The heterogeneous zone and the deep reflector are marked by dashed lines. We observe a circularly shaped P wave front propagating in all directions. Note that the outer model boundary is strongly absorbing, therefore we do not observe reflections emerging from it. In z-direction (downwards) the wavefront is relatively sharp. Scattered parts of the wave field are distributed close behind the P wave front. Such waves are commonly referred to as coda waves. These codas waves are most distinct in the direction which is indicated by the angle Θ, which denotes the deviation to the z-direction. Furthermore we recognise a series of reflected wave fronts travelling upwards to the surface. Between x=0 and 80 km the down going wave field has almost completely left the heterogeneous zone.

isomeric case: In the upper right corner the equivalent wave field in an isomeric medium is illustrated. We can observe the same circularly shaped P wave front but it is not that distinct as in the anisomeric medium. The coda waves are located not only close behind the P wave front. Instead we recognise a dense concentration of the wave field still travelling in the heterogeneous zone. The upward travelling part of the wave field consist of a continuously distributed amount of backscattered energy instead of well defined wave fronts.

20 seconds

anisomeric case: The central image on the left side shows the wave field after 20 seconds of propagation in an anisomeric medium. Within the heterogeneous zone we observe a curved P wave front travelling upwards. This reflected wave front emerges from the deep reflector. A curved S wave front, which emerged due to conversion at the deep reflector, follows approximately 20 km behind. The S wave front disappears for x-coordinates between 20 and 60 km. This is clear as there are no PS conversions for near normal incidence. Furthermore we recognise a series of wave fronts above and beneath the deep reflector for x-coordinates between 60 and 100 km. The angle Θ denotes their direction of propagation in comparison to the z-axis.

isomeric case: The central image on the right side shows the equivalent wave field in an isomeric medium. No distinct wave fronts are visible any more. The wave field is distributed over the whole model. We can observe a slightly higher wave field concentration in the heterogeneous zone. Obviously the wave field tends to remain in the heterogeneous zone. Another wave field concentration is visible above and below the deep reflector for x-coordinates between 60 and 100 km. This concentration corresponds to the series of downward travelling wave fronts in the anisomeric medium, which occur approximately at the same position.

30 seconds

anisomeric case: The lower left image shows the wave field after 30 seconds of propagation in an anisomeric medium. The upward travelling P wave front reached the surface and is not visible any more. Still visible is the converted S wave front right above the heterogeneous zone. The entire wave field almost completely vanished due to outer boundary absorption.

isomeric case: The lower right image shows the equivalent wave field for an isomeric medium. We still observe a distribution of the wave field over the whole model. We notice a distinct higher concentration above the reflector for x-coordinates between 0 and 20 km and between 80 and 100 km and below the reflector for x-coordinates between 80 and 100 km. A slightly higher concentration is visible in the heterogeneous zone. Thus, there is still a small part of the wave field trapped inside the heterogeneities.

Description of Fig. 2.6 (Gaussian medium):

This figure shows snapshots of the propagating wave field in a Gaussian distributed medium. It is structured in the same way as Fig. 2.5. In a Gaussian medium we observe the same trends as in an exponential medium. Therefore we limit our description to the differences. The P wave front in both, the isomeric and the anisomeric medium, remains generally sharper for the snapshot after 10 seconds of propagation. In the Gaussian isomeric medium the scattered part of the wave field is distributed closer behind the P wave front and does not tend to remain in the heterogeneous zone in the same intensity as it does in the exponential isomeric medium. For the 20 seconds snapshot in the isomeric medium we observe a higher concentration of the wave field above the deep reflector for x-coordinates between 70 and 100 km and below the reflector for x-coordinates between 60 and 80 km. We observe this concentration in the isomeric exponential medium as well but not that distinct. In comparison we do not notice a wave field concentration in the heterogeneous medium any more. Generally we recognise for the isomeric medium a stronger trend to forward directed propagation in comparison to the exponential isomeric medium.

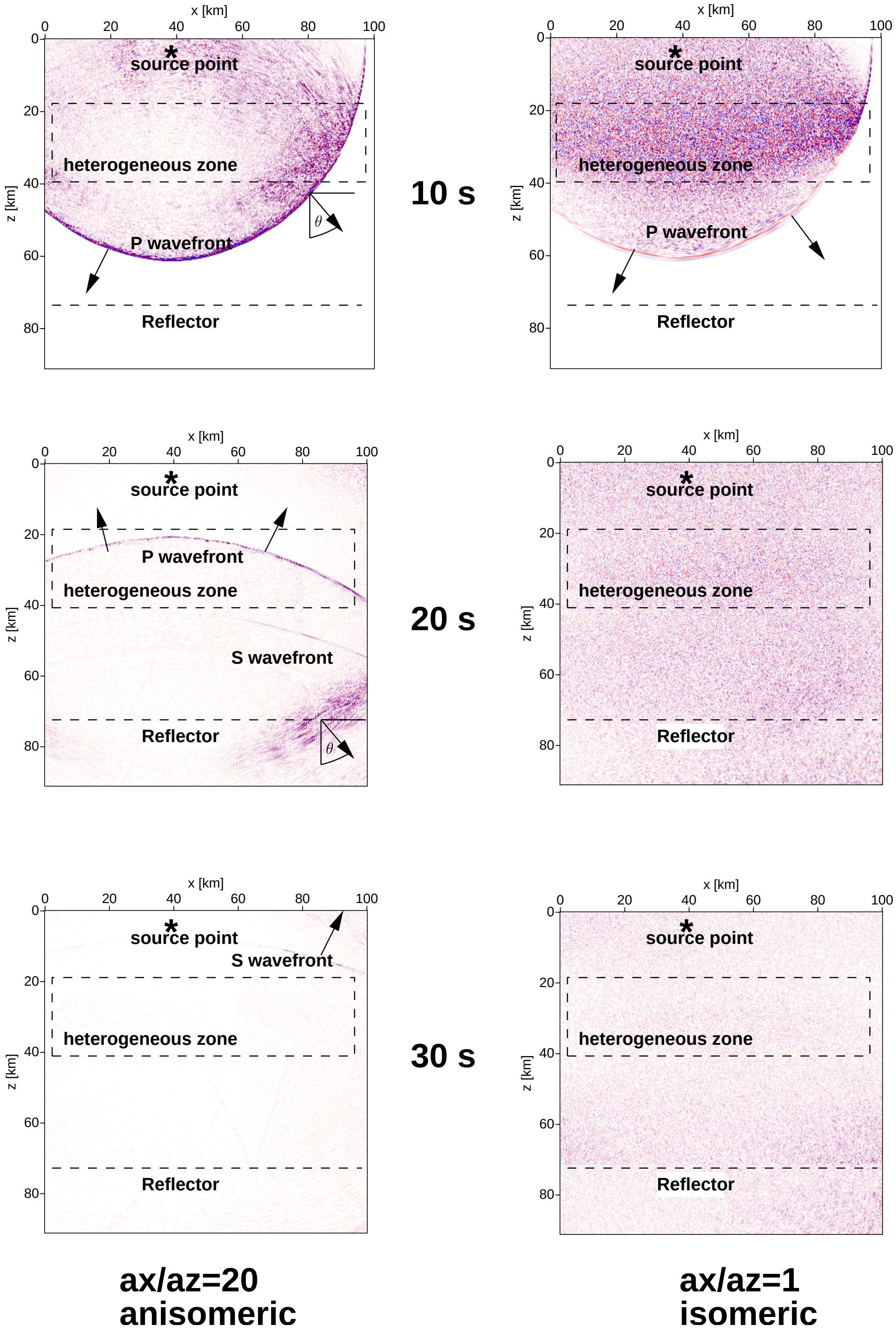

Figure 2.5: Snapshots of wave propagation in exponentially distributed random media.

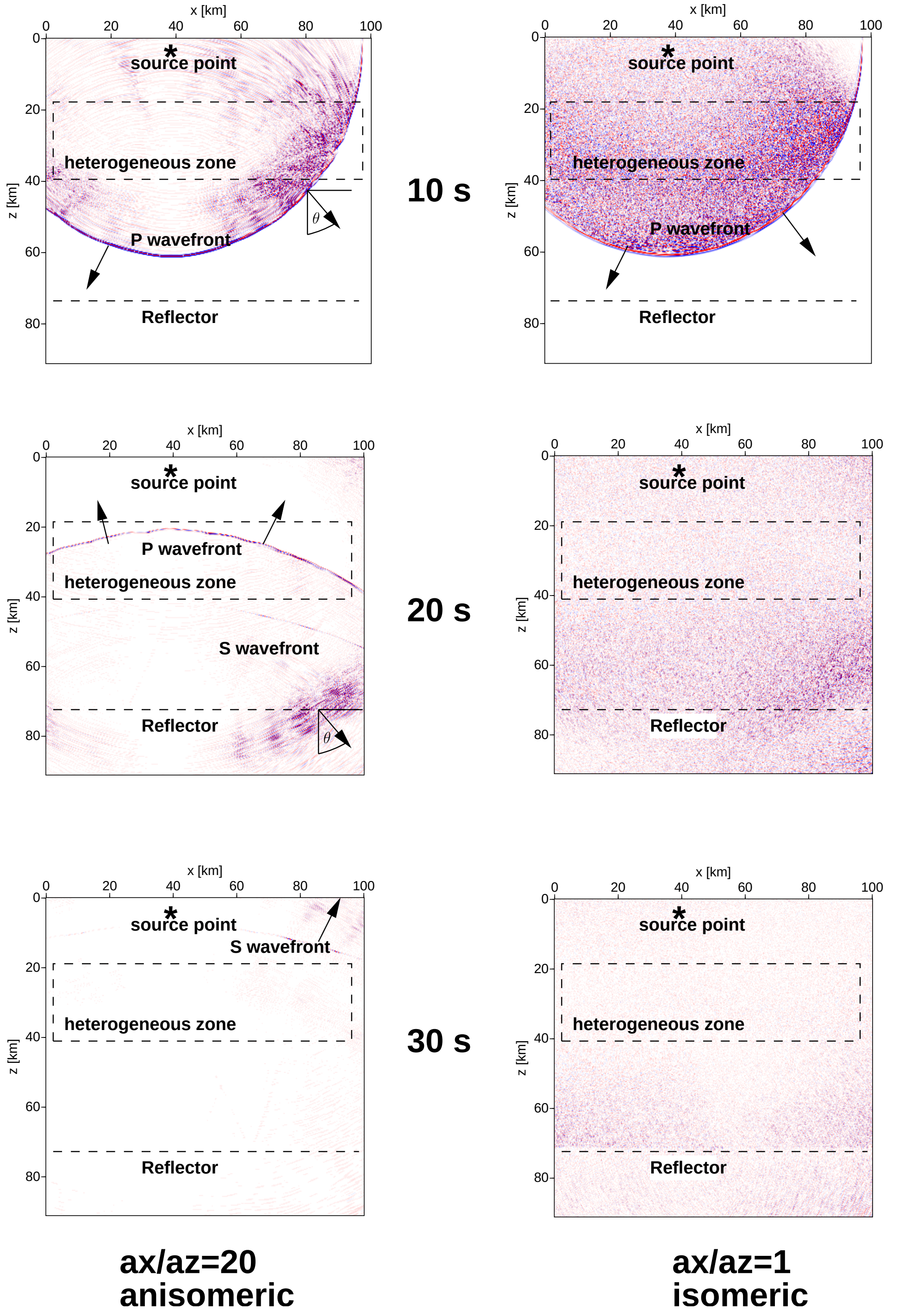

Figure 2.6: Snapshots of wave propagation in Gaussian distributed random media.

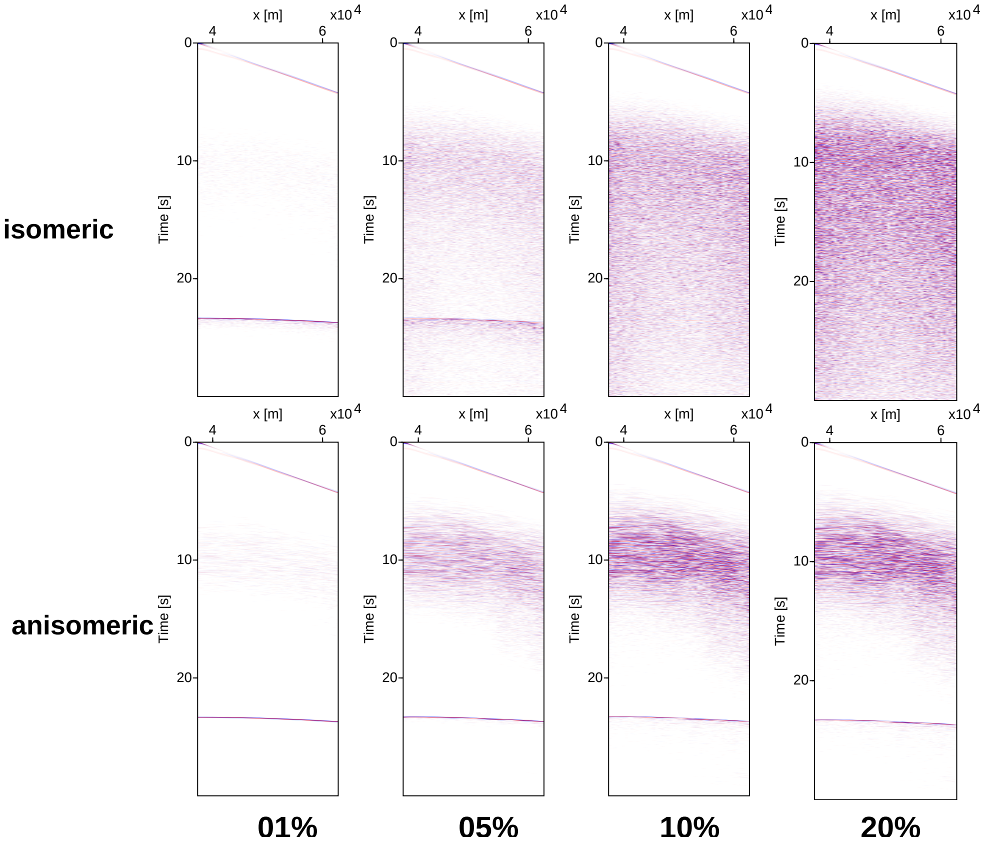

Figure 2.7: Z-component seismogram sections for an exponential medium.

2.1.5 Seismogram Sections

The FD code provides synthetic seismogram sections according to the geophone setup. Eight samples of z-component seismogram time sections recorded in an exponential distributed medium are shown in Fig. 2.7:

Description and interpretation of Fig.2.7: The upper four sections are recorded in isomeric media (i.e. $a_x = a_z = 200$ m) and the lower four in anisomeric media (i.e. $a_x = 4000$ m and $a_z = 200$ m). From left to right the standard deviation of the velocity fluctuation σ is 1%, 5%, 10% and 20%. The amplitude scaling is equal for all sections. The direct wave is clearly visible in all sections as well as arrivals from the heterogeneous zone for travel times of 5 seconds and more. These arrivals have larger amplitudes in media with larger standard deviation σ. In isomeric media we observe arrivals from the heterogeneous zone for travel times down to 30 seconds whereas in anisomeric media there are no arrivals for travel times larger than approximately 15 seconds, except the reflection from the deep boundary at approximately 22 seconds. This reflection is visible in all sections with σ=1% or 5% and in the anisomeric sections with σ=10% or 20% whereas it is invisible in isomeric media with σ=10% or 20%. In the latter case it is not possible to decide, on the basis of the information provided by the seismogram sections, whether the energy from the deep reflection is covered by scattering energy from the heterogeneous zone or whether there is no energy which has reached the reflector and travelled back up again. In all anisomeric sections the reflector appears sharp whereas it appears slightly diffuse in the isomeric section with σ=1% and noticeably diffuse in the isomeric section with σ=5%. Thus, we recognise weak and σ independent disturbing influences of anisomeric overburdens to the signal of the deep reflection and a strong and σ dependent disturbing influence of isomeric overburdens.

2.2 Processing

The following chapter illustrates the processing steps within the RIS work flow. A 'whitening' procedure and frequency bandpass filtering were applied to every seismogram section, which is illustrated in Fig. 2.8:

Description of Fig. 2.8: A sample seismogram section in frequency domain for three different processing stages is displayed. The left image shows the original unfiltered section. The central image illustrates the same section after a whitening filter was applied. Therefore the energy is more uniformly distributed over the frequency spectrum. In the right image a frequency bandpass filter was applied. The filter reduces all frequencies outside its pass-band to zero.

Furthermore a detailed spectral analysis demonstrates the influences of different random media on the seismic records. The central part of RIS is the Kirchhoff depth migration which will be explained in detail in this chapter. The final images will be discussed with respect to the quality of the deep reflector and the image of the heterogeneous zone itself.

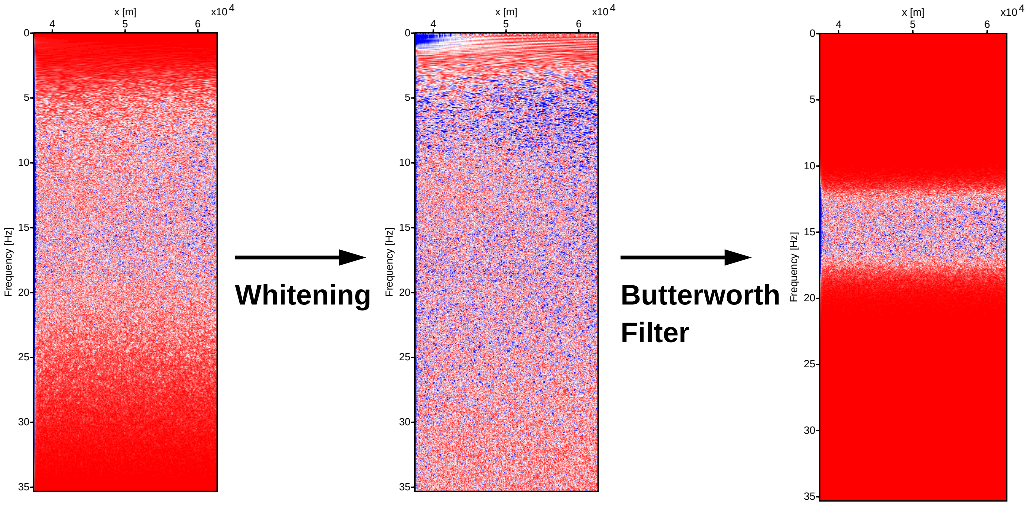

Figure 2.8: Sample seismogram section which demonstrates the applied filter actions: Whitening- and Butterworth frequency filtering. The section is shown in frequency domain. Blue colors indicate large amplitudes and red colors small amplitudes.

2.2.1 Filter Theory and Whitening

A filter is mathematically represented by a convolution of two functions, an input function I_t and a transfer function T_t. The convolution of both functions leads to an output function U_t which corresponds to our seismogram

$$U_t = I_t * T_t = \sum_k I_k T_{t-k}. \tag{2.21}$$

The asterisk denotes the convolution operator. Ideally, the input function would be a delta function. Then U_t is the impulse response of the system

$$U_t = \delta_t * T_t. \tag{2.22}$$

The transfer function itself is a series of successive convolutions representing various factors of the model which influence the wave propagation (Sheriff and Geldart, 1999, p.284)

$$T_t = q_t * r_t * t_t * c_t * p_t \tag{2.23}$$

where q_t is the zone near the source with high stresses and energy absorption, r_t the sequence of reflectors, t_t the scattering part, c_t conversion effects and p_t a combination of additional modifying effects (absorption, multiples ...). To estimate the amount of scattering a filter action is necessary which eliminates all effects but t_t. Of course, the construction of such a filter is only possible in an approximate way. The removal of a particular filter always needs the construction of an inverse filter. The application of an inverse filter is commonly referred to as deconvolution. As convolution is commutative we rearrange equation (2.22) in such a way that we have two new functions, one representing all source factors (W_t) and one representing the model response factors (M_t)

$$W_t * M_t = U_t. \tag{2.24}$$

Next an inverse filter W_t^{-1} is applied. In this thesis W_t^{-1} is simply determined by taking the direct wave of a corresponding homogeneous model and correcting every trace of the seismogram section with it

$$M_t = U_t * W_t^{-1}. \tag{2.25}$$

The deconvolution in time domain can be written as a division in frequency domain

$$M_f = \frac{U_f}{W_f}. \tag{2.26}$$

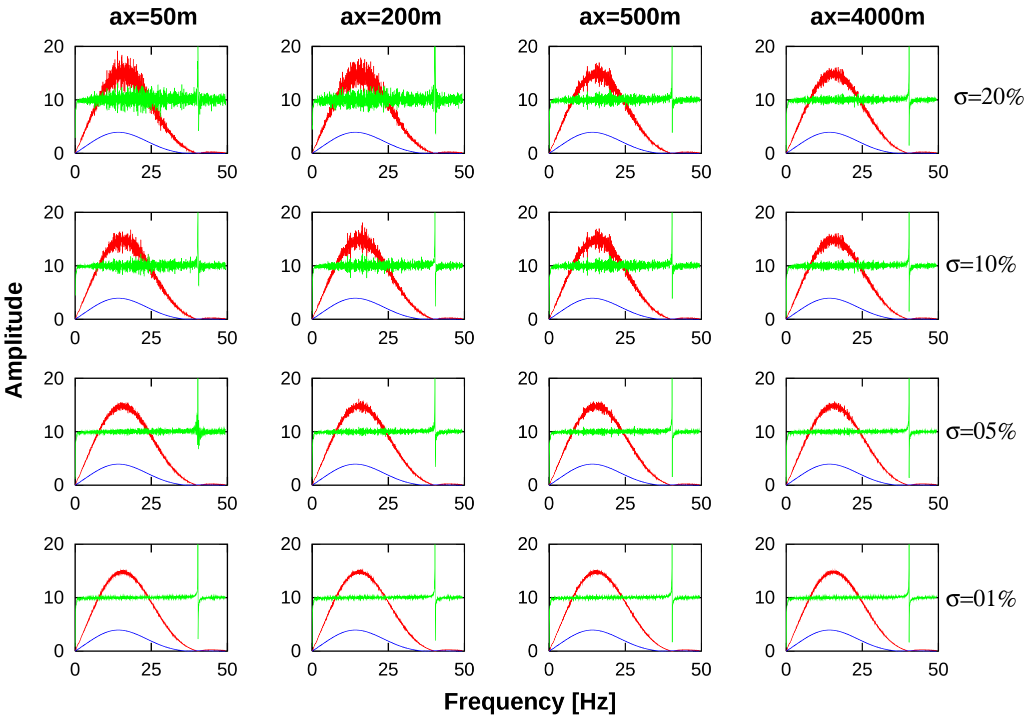

Figure 2.9: Spectral analysis of the first trace in seismogram sections for different **exponentially** distributed random media. Blue is the spectrum of the direct wave for a homogenous model multiplied by a factor of $4 \cdot 10^{10}$. Red is the spectrum of the first trace multiplied by a factor of $5 \cdot 10^{-2}$. Green is the spectrum of the whitened first trace multiplied by a factor of $1 \cdot 10^{-10}$.

where M_f,U_f and W_f are the Fourier transforms of the corresponding time functions. Equation (2.26) can be referred to as 'whitening' because it removes the effect of the input wavelet. After 'whitening' equal probabilities exists that the amplitudes at all frequencies will be equal as they are for 'white' light. For further analysis of frequency dependent scattering, a white spectrum is essential. Without 'whitening' one would observe a concentration of scattered energy around the dominant frequency of the source wavelet.

2.2.2 Spectral Analysis

The used source wavelet has a well defined spectrum with a dominant frequency of about 13 Hz. Naturally, this spectrum is visible in the unfiltered seismogram sections. For a homogeneous model the spectra of the direct wave and the source wavelet are strongly correlated. Therefore, we use the

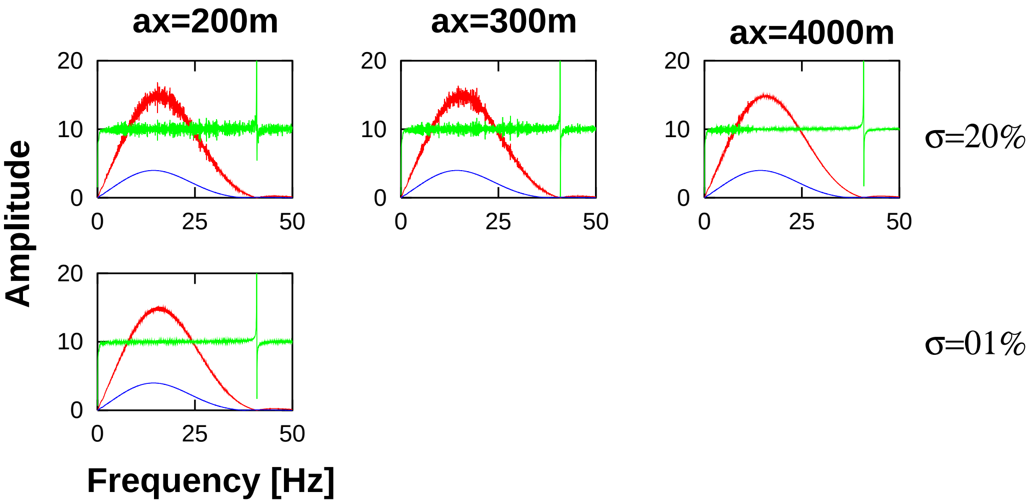

Figure 2.10: Spectral analysis of the first trace in seismogram sections for different **Gaussian** distributed random media. Blue is the spectrum of the direct wave for a homogenous model multiplied by a factor of $4 \cdot 10^{10}$. Red is the spectrum of the first trace multiplied by a factor of $5 \cdot 10^{-2}$. Green is the spectrum of the whitened first trace multiplied by a factor of $1 \cdot 10^{-10}$.

spectrum of the direct wave in a homogeneous model as the Fourier transform of the source term (W_f) in the whitening process (see equation (2.26)). The first trace of the seismogram sections in Fig. 2.7 is the trace closest to the source point. Therefore it is assumed to be less influenced by the medium's heterogeneity, due to short travel paths. We examine the power spectra of first traces in seismogram sections recorded in different exponential distributed heterogeneities in Fig. 2.9.

Description and interpretation of Fig. 2.9: Illustrated are 16 power spectra for first traces of seismogram sections recorded in different exponential distributed model realizations. From left to right the columns indicate model realizations with horizontal correlation lengths of a_x= 50, 200, 500 and 4000 m. From top to bottom the rows indicate model realizations with standard deviations of σ= 20, 10, 5 and 1%. In all plots the blue curve is the spectrum of the direct wave in a corresponding homogeneous model and hence equal for all plots. The red curve is the spectrum before the whitening filter is applied and the green curve is the spectrum after the application of the whitening filter. All green curves illustrate the effect of whitening very well since we have the same average amplitude for all frequencies. The discontinuity at approximately 40 Hz is caused by a zero of W_f, but for further studies we do not take into account frequency ranges of 40 Hz or more. Comparing the

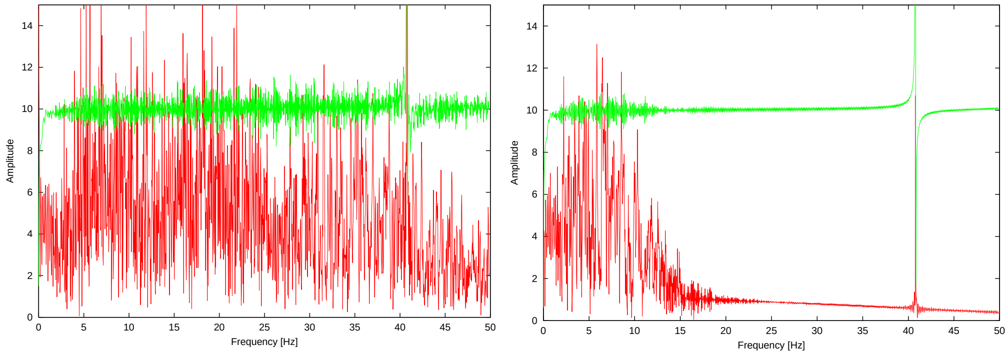

Figure 2.11: Whitened spectrum of trace 1 (green) and trace 100 (red) for a medium with: left: ax=200m fluk=20% and right: ax=4000m fluk=20%

blue curve with the red and green curves we notice deviations from the average amplitude in the red and green curves whereas the blue curve is smooth. These deviations are maximal for σ=20% and isomeric media (i.e. a_x=200 m). Interestingly, in Fig. 2.7 we determined the most disturbing influence to our seismic record in isomeric media with σ=20% as well. Obviously the spectral amplitude deviations and the perturbations of the seismic record are correlated. If we assume that the perturbations of the seismic record are mainly caused by scattering, the observed deviations are correlated to the scattering power as well.

We analyse the spectra of first traces in seismogram sections with Gaussian distributed heterogeneities as well. We do not have as much seismogram sections for Gaussian media as we have for exponential media. Therefore only four spectra are illustrated

Description and interpretation of Fig. 2.10: The figure is structured in the same way as Fig. 2.9. Again the spectra of the direct wave and of unfiltered and whitened first traces for different model realizations are illustrated. We make the same observations as we did for exponential media. Furthermore another interesting effect is visualised here. For anisomeric media (i.e. a_x=4000 m) the amplitude deviation becomes smaller for higher frequencies, i.e. the amplitude reaches its average value. This effect is commonly referred to as self-averaging (see Shapiro and Hubral, 1999, p.14-18). Even for a_x=300 m we observe a slight decrease of the amplitude deviation for higher frequencies in comparison to a_x=200 m. Hence the frequency range for which self-averaging occurs depends on the ratio of a_x to a_z, i.e. the grade of anisometry. We can observe this self averaging effect for exponential media as well, but not that distinct.

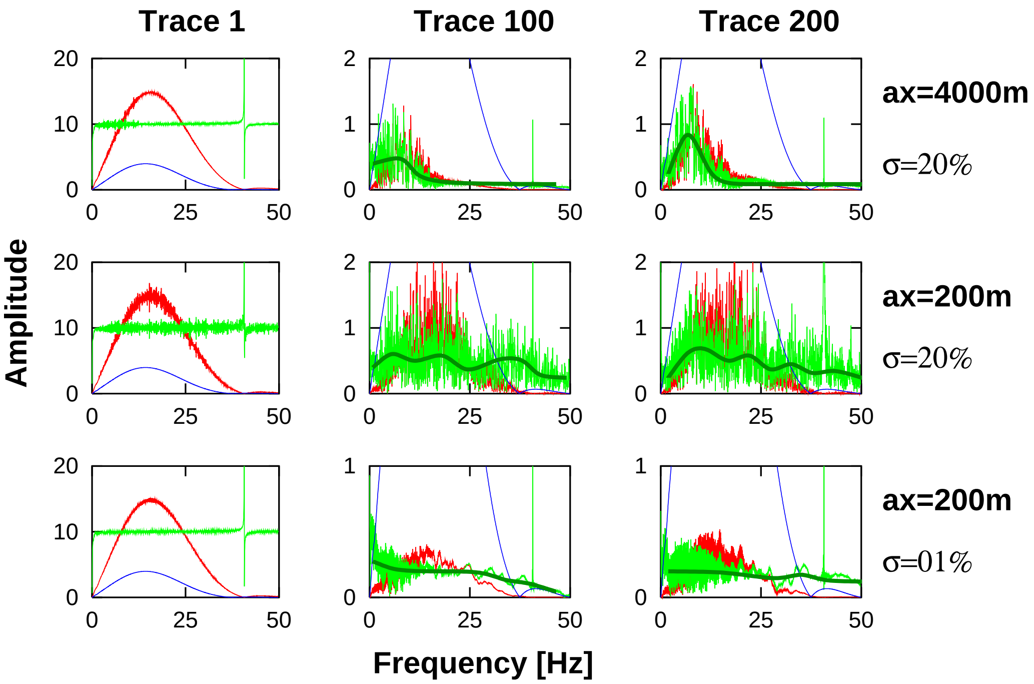

Figure 2.12: Spectra of trace 1, 100 and 200 in seismogram sections for Gaussian distributed media. Red is the spectrum without the whitening filter. Green is the whitened spectrum. Blue corresponds to the spectrum of the direct wave in a homogeneous model. The thick green line indicates the characteristic of the average amplitude in the whitened spectra.

Fig. 2.11 illustrates spectra of the whitened first trace (green curve) and the whitened 100^{th} trace (red curve) recorded in Gaussian media with σ=20%. The left image shows the spectra in an isomeric media (a_x=200 m) and the right image in an anisomeric media (a_x=4000 m). The red curve is multiplied by a factor of 10. Here the strong self averaging effect in anisomeric media is very distinct, due to the bigger size of the plot. The red curve shows significant differences to the green curve. Therefore it is of interest to expand the spectral study to traces which are further away from the source than the first trace. Fig. 2.12 illustrates the spectral analysis of trace 100 and trace 200 in comparison to trace 1 in different Gaussian media.

Description and interpretation of Fig. 2.12: The three columns indicate from left to right the first, the 100th and the 200th trace (10 and 20 km distance to the source). The first row from the top indicates records in an anisomeric model realization with a_x=4000 m and σ=20%. The second and third row indicate records in models with a_x=200 m and σ=20% or 1%. The blue curve is the spectrum of the direct wave in a homogenous model and equal for all plots, the red curve is the unfiltered spectrum of the according trace and the green curve is the whitened spectrum of the according trace. We discuss the differences of trace 100 and trace 200 to trace 1. The amplitude values of trace 100 and 200 are ten percent of the amplitudes in trace 1, which is clear due to geometrical spreading, whereas the amplitude deviation is of the same order as in trace 1. Referring to the red curves we notice in the anisomeric case (i.e. a_x=4000 m) a suppression of frequencies higher than approximately 20 Hz. Obviously the Gaussian anisomeric media acts as a low pass frequency filter. Interestingly the suppressed frequency range correlates with the frequency range for which we observe self averaging in trace 1. In the isomeric case (i.e. a_x=200m) the full range of the spectrum is conserved even for records 10 or 20 km away from the source. Interestingly in the isomeric case with σ=1% (last row in the figure) we observe self averaging effects (i.e. a decrease of the amplitude deviations for higher frequencies) for the red and green curves in trace 100 and 200 which we cannot observe in trace 1. Referring to the green curves in trace 100 and 200 we notice that the whitening filter does not work as accurate as in trace 1. Therefore the average amplitude is not equal for all frequencies. In the anisomeric case the whitened spectrum is almost equal to the unfiltered spectrum whereas in the isomeric case we observe weak fluctuations of the average amplitude of the whitened spectrum. The characteristic of the average amplitude in the whitened spectra is marked by a thick green line.

2.2.3 Frequency Filtering

The aim is to create a series of seismogram sections for different frequency bands from the original whitened seismogram section. Therefore, we need to construct a transfer function $f(\omega)$ with a well defined band-pass and its impulse response $f(t)$. We denote the whitened input seismogram section as $U(x,t)$ and its Fourier transform as $\tilde{U}(x,\omega)$. The filter action can be written as follows

$$U(x,t) * f(t) = \bar{U}(x,t) \quad \text{or} \quad \tilde{U}(x,\omega) \cdot f(\omega) = \bar{\tilde{U}}(x,\omega) \tag{2.27}$$

where $\bar{U}(x,t)$ is the output seismogram section and $\bar{\tilde{U}}(\omega,t)$ its Fourier transform. There are several realisations for $f(\omega)$ with different advantages and disadvantages. A transfer function has either a causal or acausal impulse response, it has a particular amplitude and phase characteristic. There is no ideal filter due to two limitations:

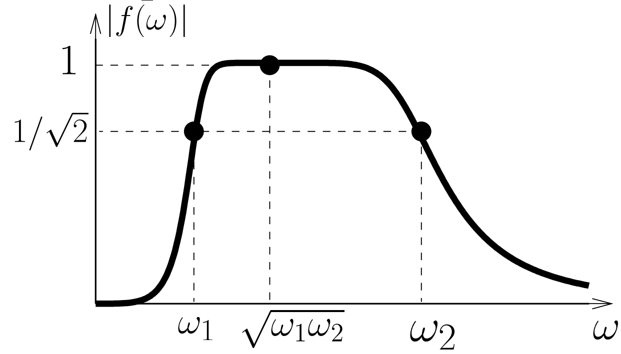

Figure 2.13: Absolute value of the complex Butterworth transfer function.

1. The better the frequency resolution the worse the time resolution:

$$\Delta\omega \cdot \Delta T \geq 2. \tag{2.28}$$

2. A causal impulse response causes phase shifts but a transfer function without phase shifts automatically has an acausal impulse response.

The resolution condition (1) forces to choose frequency windows of a particular width instead of single frequencies. Due to condition (2) we prefer a causal impulse response in order to prevent such problems as time shifts of arrivals in the filtered sections. Hence, a Butterworth band pass filter is chosen for this study which has the following transfer function (Müller, 1994)

$$f(\omega) = \frac{(-i)^n}{\prod_{k=1}^{n} \left(\frac{\omega^2 - \omega_1\omega_2}{\omega(\omega_2 - \omega_1)} - exp[i\pi \frac{2k-1}{2n}] \right)} \tag{2.29}$$

where $\omega_{1,2}$ are the limiting frequencies and n describes the edge steepness. A flat edge would generate a filter of only a small range where $|f(\omega)| = 1$, whereas a steep edge results in wiggles for the impulse response due to the Gibbs phenomena. As a good compromise we choose n=4. The amplitude characteristic of $f(\omega)$ is

$$|f(\omega)| = \frac{1}{\left[1 + \left(\frac{\omega^2 - \omega_1\omega_2}{\omega(\omega_2 - \omega_1)} \right)^2 n \right]^{1/2}}. \tag{2.30}$$

For n=4 equation (2.30) is shown in Fig. 2.13. The amplitude characteristic is asymmetric and reaches its maximum value of 1 at $\omega = \sqrt{\omega_1\omega_2}$.

Filter f_k	$\sqrt{\omega_1\omega_2}$
f_1	2.45
f_2	4.04
f_3	5.45
f_4	6.81
f_5	8.12
f_6	9.42
f_7	10.71
f_8	11.99
f_9	13.27
f_{10}	14.54
f_{11}	15.80
f_{12}	17.07
f_{13}	18.33
f_{14}	19.59
f_{15}	20.85
f_{16}	22.11
f_{17}	23.37
f_{18}	24.62
f_{19}	25.88
f_{20}	27.14
f_{21}	28.39

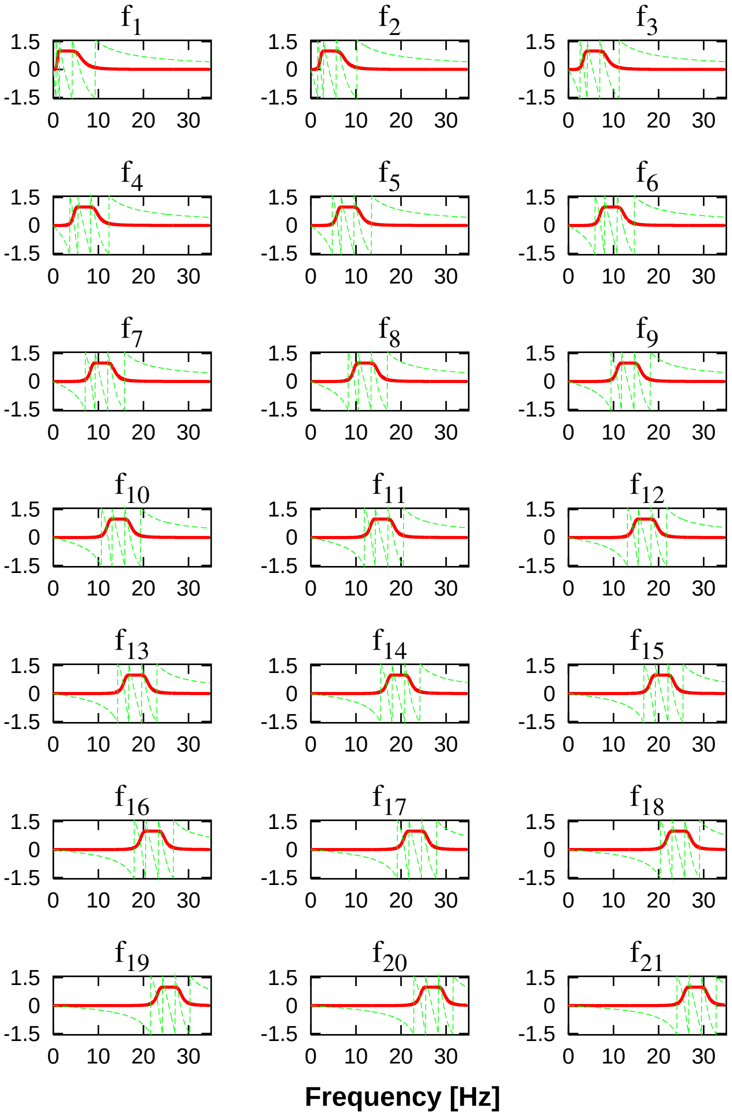

Figure 2.14: All used butterworth transfer functions with their mean frequencies and amplitude (red) and phase (green) characteristics.

In total, 21 different transfer functions for different neighbouring frequency ranges are applied. Fig. 2.14 shows a table where all 21 butterworth transfer functions are listed with their according mean frequencies $\sqrt{\omega_1\omega_2}$. On the right side of the table the corresponding amplitude (red) and phase (green) characteristics are illustrated. According to the 21 transfer functions in Fig. 2.14 we show results for whitened and frequency butterworth filtered seismogram sections in Fig. 2.15 and Fig. 2.16.

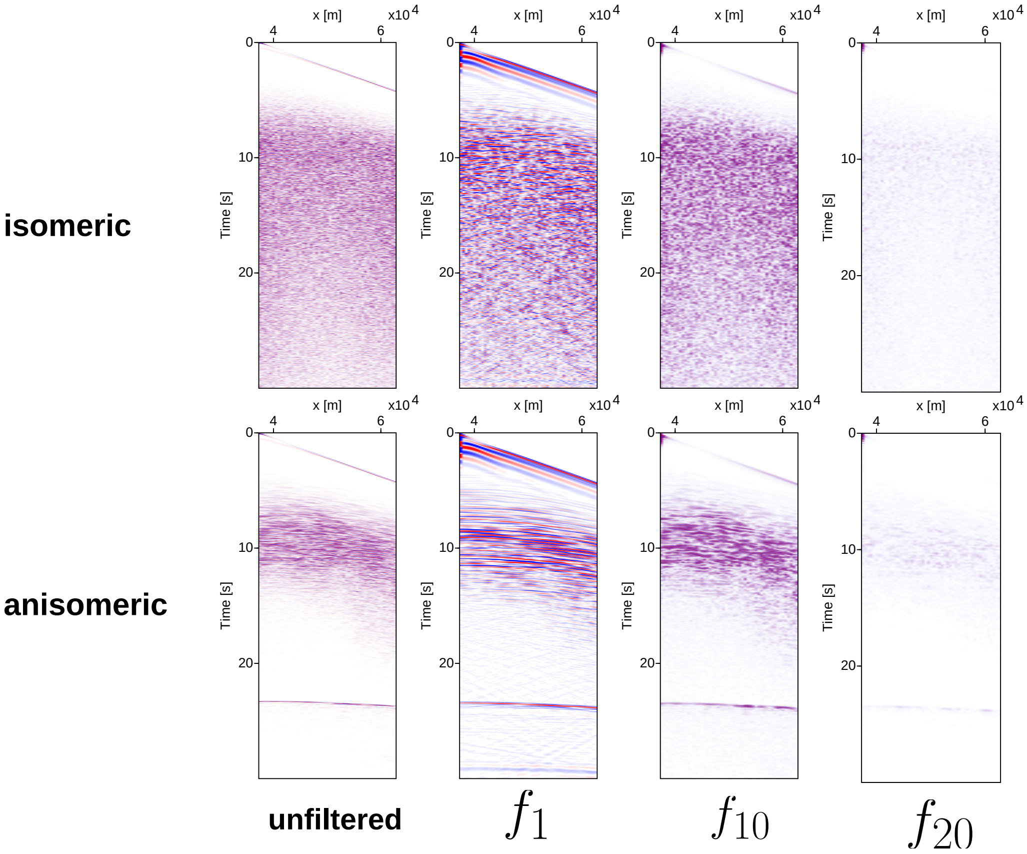

Figure 2.15: The original and three filtered seismogram sections for **exponentially** distributed media and $\sigma = 20$ %. Isomeric means $a_x = a_z = 200$ m. Anisomeric means $a_x = 4000$ m and $a_z = 200$ m. The amplitude scaling is equal for the six filtered sections and for the two unfiltered sections.

Description and interpretation of Fig. 2.15: The following explanations are based on the description of Fig. 2.7. All eight illustrated seismogram sections were recorded in model realizations containing exponential distributed heterogeneities with σ=20%. The figure is structured in two rows and four columns. The upper row displays sections recorded in isomeric media (i.e. $a_x = a_z = 200$ m) and the lower row sections recorded in anisomeric media (i.e. $a_x = 4000$ m and $a_z = 200$ m). The four columns indicate from left to right sections containing the whole frequency spectrum (unfiltered) and sections filtered by a butterworth band pass filter with a mean frequency of 2.45 Hz (f_1), 14.54 Hz (f_{10}) and 27.14 Hz (f_{20}). Every mean frequency f corresponds to a certain wavelength λ. We determine the wavelengths by the fundamental relation $V = \lambda\ f$ and obtain: $\lambda_1 \approx 2400$ m, $\lambda_{10} \approx 400$ m and

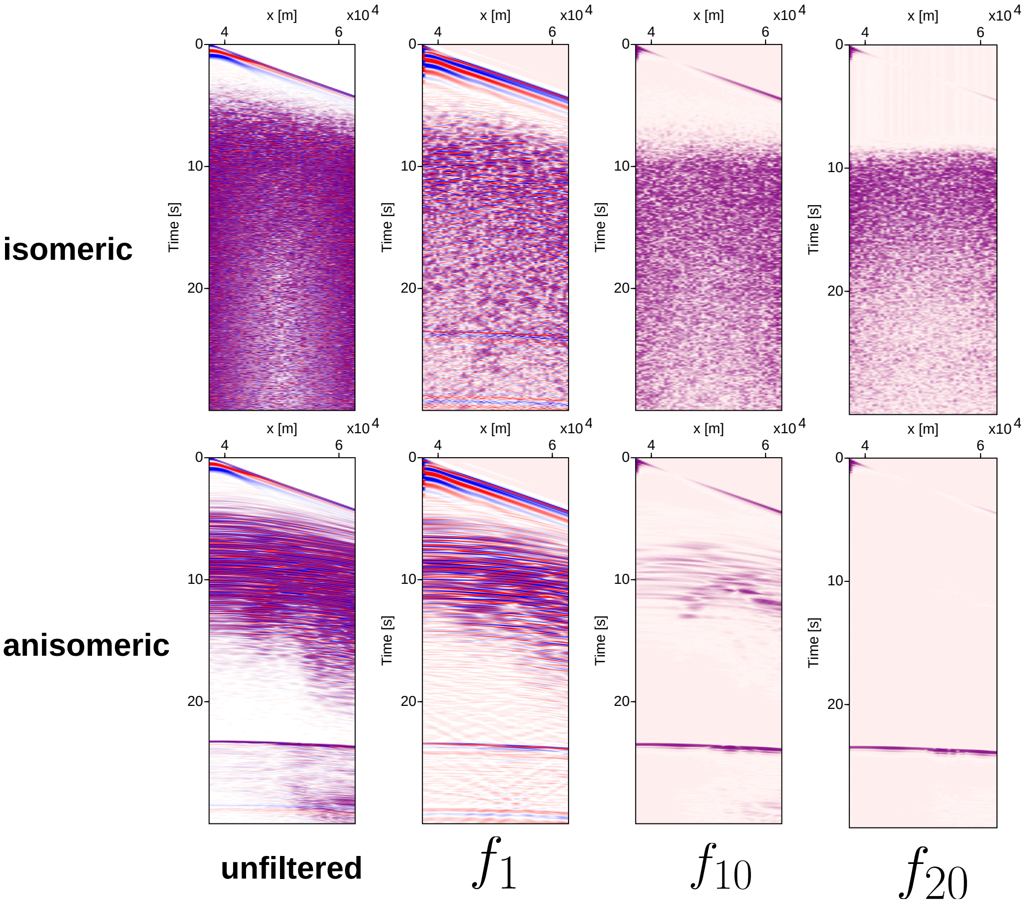

Figure 2.16: The original and three filtered seismogram sections for **Gaussian** distributed media and $\sigma = 20$ %. Isomeric means $a_x = a_z = 200$ m. Anisomeric means $a_x = 4000$ m and $a_z = 200$ m. The amplitude scaling is equal for the six filtered sections and for the two unfiltered sections.

$\lambda_{20} \approx 220$ m. Before application of the band pass filter a whitening filter was applied. The amplitude scaling is equal for the two unfiltered sections and the six filtered sections. At first view we recognise that different amplitude strength exists for different mean frequencies, strong amplitudes for low frequencies (f_1 and f_{10}) and weak amplitudes for high frequencies (f_{20}). Although we applied a whitening filter the energy is concentrated in low frequency ranges. Obviously the whitening filter do not manage to equalise the amplitudes for all frequencies in exponential media, neither isomeric nor anisomeric. We already discussed the accuracy of the whitening filter in Gaussian media in the description of Fig. 2.12. Furthermore we recognise that the direct wave is visible in all sections. Due to a limited resolution it appears broader for low frequencies. The deep reflection at approximately 22 seconds is clearly visible in all sections in anisomeric media but appears diffuse for f_1 and f_{10} due to bad resolution. The deep reflection is not visible in isomeric media in the unfiltered and in the f_{10} and f_{20} sections but slightly visible in the f_1 section. The arrivals from the heterogeneous zone are visible for all three frequency ranges (f_1,f_{10} and f_{20}) in both, isomeric and anisomeric media. This shows that even a seismic wave field with a wavelength ten times larger ($\lambda_1 \approx 2400$m) than the correlation length ($a_x = a_z = 200$ m in the isomeric case) is influenced in its propagation by reflection and backscattering.

Description and interpretation of Fig. 2.16: The figure is structured in the same way and shows the same seismogram sections as Fig. 2.15 but for Gaussian media. We observe the same qualitative trends as in an exponential medium. Therefore only the differences are discussed. In the isomeric case the amplitudes are of the same magnitude in all three displayed frequency ranges (f_1,f_{10} and f_{20}). In contrast, in the anisomeric case the amplitudes for a high frequency range (f_{20}) are such small that the arrivals of the heterogeneous zone are not visible with the given amplitude scaling. The deep reflection in the isomeric f_1 section is of better quality than in the corresponding section in exponential media. Furthermore we observe in the unfiltered isomeric section for 15 seconds and more smaller amplitudes for the arrivals of the heterogeneous zone in central traces in comparison to traces on the left or right side of the section. The same is true for the isomeric f_{10} and f_{20} section but not for the f_1 section.

2.2.4 Kirchhoff Migration

Migration is a repositioning process which moves the recorded energy to the position of the reflecting or diffracting elements in the subsurface. There are different migration techniques which involve the solution of the wave equation by e.g. the frequency-wavenumber method (Gazdag, 1978), the finite-difference method (Claerbout, 1970) or the Kirchhoff method (Schneider, 1978). All techniques are divided into two steps: Wave field **extrapolation** and **imaging**. Wave field extrapolation means to propagate the wave field recorded at the surface $U(x, z = 0, t)$ back in time and space down into the subsurface

$$U(x, z = 0, t) \rightarrow U(x, z, t). \tag{2.31}$$

Imaging means to assign the elements of the extrapolated wave field to subsurface points for certain imaging times $t_I(x, z)$, where t_I depends on the

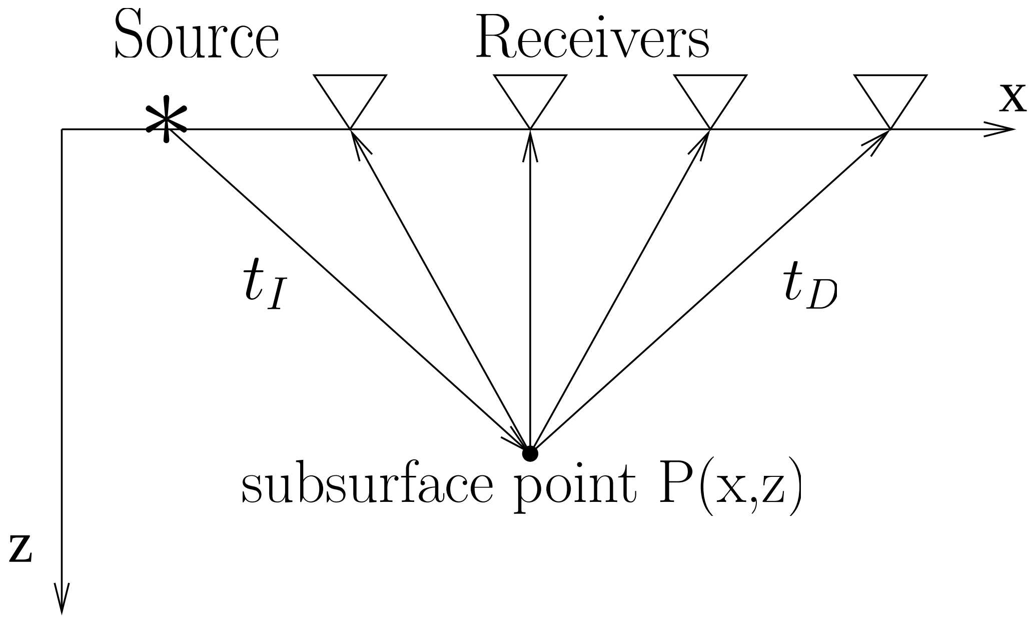

Figure 2.17: The imaging time t_I corresponds to the travel time between source and subsurface point, whereas t_D corresponds to the travel time between subsurface point and receiver.

particular type of wave field, e.g. S or P waves (see Fig. 2.17 for definition of t_I and t_D)

$$M(x,z) = U(x,z,t_I). \tag{2.32}$$

$M(x,z)$ is the migrated section. In this thesis the Kirchhoff migration method was used. Kirchhoff migration is based on an integral solution of the wave equation. The solution is commonly referred to as the Kirchhoff formula. The Kirchhoff formula is derived by a solution of the Helmholtz equation. The following derivation is taken from Buske (1994). The Helmholtz equation corresponds to the wave equation of the Fourier transformed wave field $\mathcal{F}[U] = \tilde{U}$:

$$\Delta\tilde{U}(x,z,\omega) \quad + \quad k^2\tilde{U}(x,z,\omega) = 0 \tag{2.33}$$

where k is the wavenumber vector. The solution of equation (2.33) for an area with the surface S and the boundary L (Fig. 2.18) can be obtained referring to the theorem of Green

$$\int_S [\tilde{U}\Delta\tilde{G} - \tilde{G}\Delta\tilde{U}]dS = \int_L [\tilde{U}\nabla\tilde{G} - \tilde{G}\nabla\tilde{U}]dL. \tag{2.34}$$

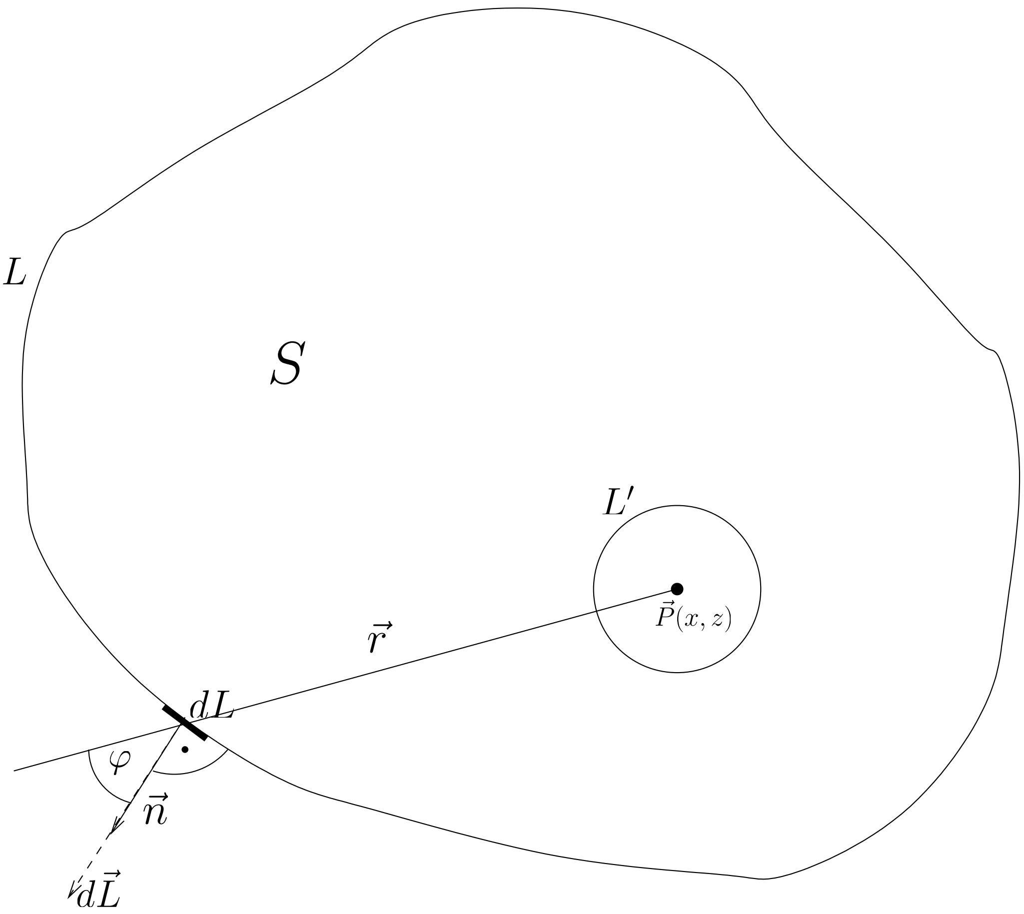

Figure 2.18: The Helmholtz equation is solved in an arbitrary area with the surface S and the boundary L. We exclude the singularity at the subsurface point $P(x, z)$ by a circle with the boundary L'.

where $\tilde{G}$ is the Fourier transform of the Greens function G and therefore a known solution of equation (2.33). G depends on the particular problem. As $\tilde{G}$ and $\tilde{U}$ are solutions of equation (2.33) we can assume

$$\Delta\tilde{U} = -k^2\tilde{U} \qquad \text{and} \qquad \Delta\tilde{G} = -k^2\tilde{G}. \tag{2.35}$$

Therefore the surface integral in equation (2.34) becomes zero. The validity of the theorem of Green is only given for areas without singularities. G is singular at the source point. Hence we exclude the source point by a circle with the boundary L' (Fig. 2.18). Thus equation (2.34) becomes

$$0 = \int\limits_{L} [\tilde{U}\nabla\tilde{G} - \tilde{G}\nabla\tilde{U}]dL + \int\limits_{L'} [\tilde{U}\nabla\tilde{G} - \tilde{G}\nabla\tilde{U}]dL'. \tag{2.36}$$

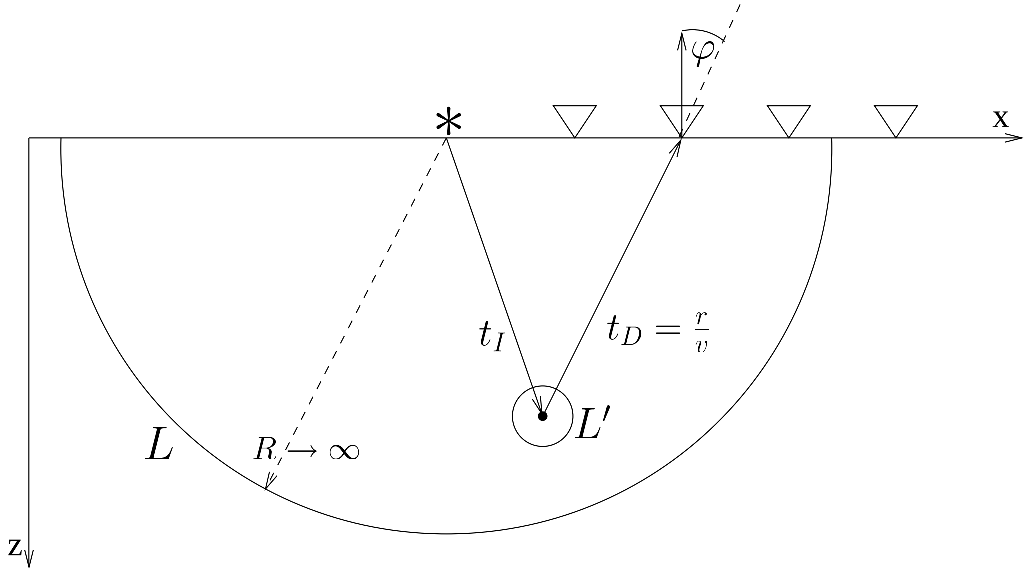

Figure 2.19: The semicircle surface for the derivation of the Kirchhoff formula.

The solution of the Helmholtz equation is reduced to the solution of two line integrals. The inverse Fourier transformation yields the solution of the wave equation. For seismic Kirchhoff migration we chose a semicircle with the radius R as the area enclosed by L (see Fig. 2.19). With $R \to \infty$ and an appropriate Greens function $\tilde{G}$ the solution for the wave field $U(x, z, t)$ is given by

$$U(x,z,t) = \frac{1}{\pi} \int\limits_{-\infty}^{\infty} \frac{\partial U}{\partial t} * \frac{tH(-t - \frac{r}{v})}{r\sqrt{t^2 - \frac{r^2}{v^2}}} cos\varphi dx \qquad (2.37)$$

where H is the Heavy Side step function, r the distance between subsurface point and receiver, v the seismic velocity, φ the angle of incidence and $*$ symbolises a convolution. When the wave field at the surface along the x-axes is known, the complete wave field for the subsurface can be calculated assuming known seismic velocities v. The convolution can be written as an integral with respect to space and time

$$g(x,t) * h(x,t) = \int\limits_{-\infty}^{\infty} \int\limits_{-\infty}^{\infty} g(x',t')h(x-x',t-t')dx'dt'. \qquad (2.38)$$

Then the formula for the Kirchhoff migration is:

$$M(x,z) = U(x,z,t_I(x,z)) = \int_{-\infty}^{\infty}\int_{-\infty}^{\infty} \frac{\partial U(x',z=0,t')}{\partial t'} W(x'-x,t'-t_I)dt'dx' \tag{2.39}$$

with the weighting function

$$W(\xi,\tau) = \frac{-z\tau H(\tau-\frac{r}{v})}{\pi r^2\sqrt{\tau^2-\frac{r^2}{v^2}}} \tag{2.40}$$

with

$$\xi = x'-x \quad ; \quad \tau = t'-t_I \quad ; \quad r^2 = \xi^2+z^2 \quad ; \quad cos\varphi = \frac{z}{r}. \tag{2.41}$$

As the amplitudes are summed along a diffraction hyperbola Kirchhoff migration is also referred to as a weighted diffraction stack. Due to the weighting function W traces closer to the imaging point are more relevant than traces further away. W also corrects for obliquity φ and geometrical spreading. In this thesis we use an approximation of the filter operator in equation (2.37),

$$\begin{aligned} \frac{tH(-t-\frac{r}{v})}{\sqrt{t^2-\frac{r^2}{v^2}}} &\approx -\sqrt{\frac{r}{2v}}f(t)*\delta(t+\frac{r}{v}) \\ \text{with} \quad f(t) &= \frac{H(-t)}{\sqrt{-t}} \end{aligned} \tag{2.42}$$

which reduces the solution to one integral along the x-axis:

$$M(x,z) \approx U(x,z,t_I(x,z)) = \int_{-\infty}^{\infty} U_f(x',z=0,t_I+\frac{r}{v})V(x')dx' \tag{2.43}$$

with the approximative weighting function V

$$V(x') = \frac{-1}{\pi\sqrt{2v}}\;\frac{z}{r^{\frac{3}{2}}} \tag{2.44}$$

and

$$U_f(x',z=0,t) = \frac{\partial U(x',z=0,t)}{\partial t} * f(t). \tag{2.45}$$

The numerical implementation of equation (2.43) is divided into two steps:

1. Travel time calculation:
   The travel times from the source to every subsurface point ($t_I(x,z)$) and

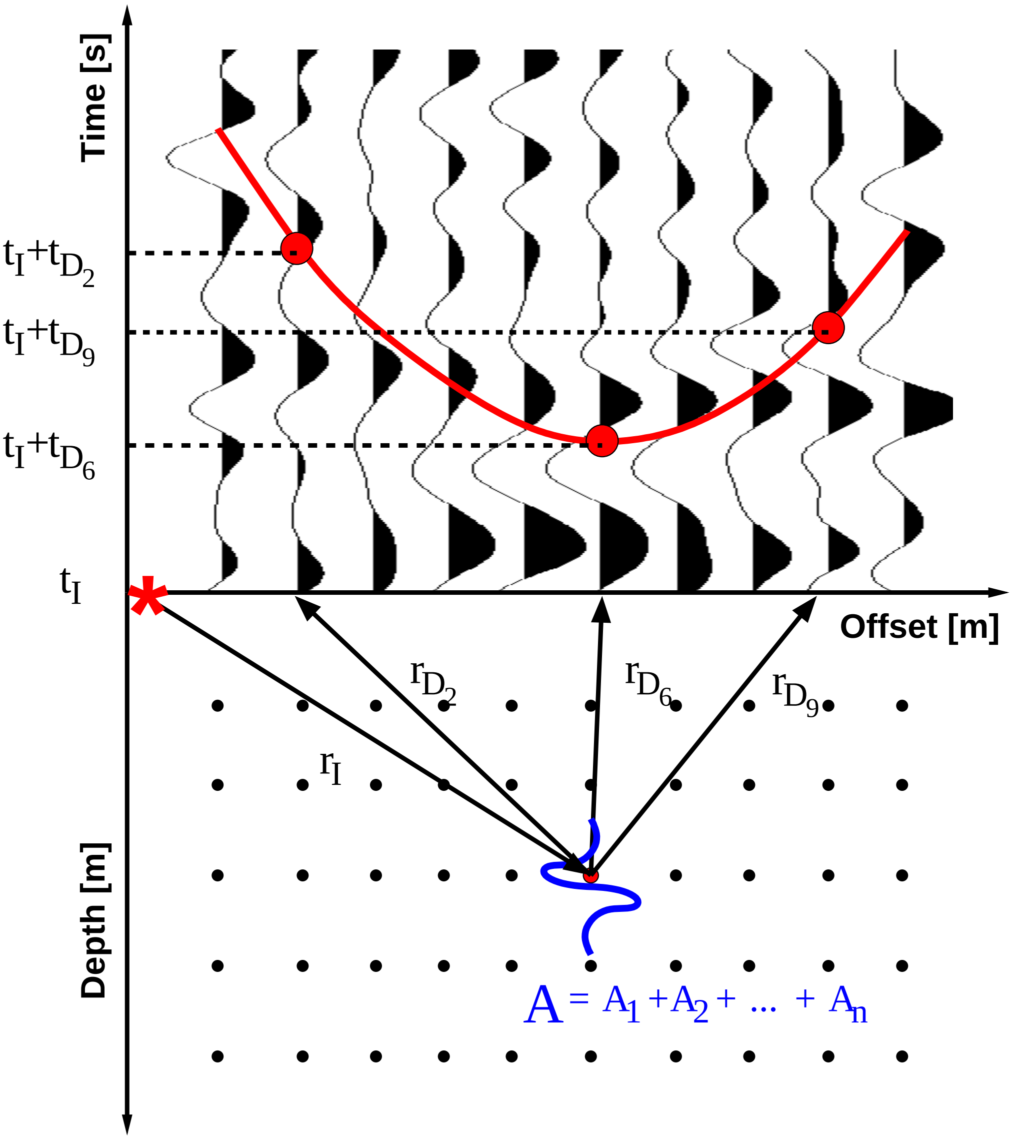

Figure 2.20: Principle of Kirchhoff Migration. For every subsurface point t_I and every t_D are calculated. The amplitudes along the resulting diffraction hyperbola are summed up and placed at the particular subsurface point.

from every subsurface point to every receiver ($t_D(x,z)$) are calculated. In our case this turned out to be very simple as we assumed for the velocity model:

$$\langle V(x,z)\rangle = V_0 = 6000 \quad m/s \tag{2.46}$$

Therefore:

$$t_I(x,z) = \frac{\sqrt{(x-x_{src})^2 + (z-z_{src})^2}}{V_0} \tag{2.47}$$

$$t_D(x,z) = \frac{\sqrt{(x-x_{rcv})^2 + (z-z_{rcv})^2}}{V_0} \tag{2.48}$$

2. Integration:
   Before integrating we apply a filter to every trace of the seismogram time section. The filter is defined by $f(t)$ in equation (2.42). The integration process consists of a summation of all amplitudes along the diffraction hyperbola $t_D + t_I = \frac{r_D + r_I}{V_0}$. Every single amplitude is multiplied with the weighting factor V (see equation (2.44)) before summation.

The implementation of the Kirchhoff migration is illustrated in Fig. 2.20. In the upper half the figure shows a random seismogram time section with 10 traces. The lower half shows a depth section realized by several grid points. The source is denoted by the red asterisk. For every grid point the according amplitude value A is calculated. This is exemplarily shown for the red marked grid point. For the calculation of A all amplitudes along the red diffraction hyperbola are summed up and placed to the red grid point. In a homogeneous velocity model the diffraction curve is effectively a hyperbola whereas it deviates from a hyperbola for heterogeneous velocity models.

Fig. 2.21 and Fig. 2.22 show the results of Kirchhoff migration for the sections in Fig. 2.15 and Fig. 2.16.

Description and interpretation of Fig. 2.21: Illustrated are two unfiltered and six frequency band pass filtered samples, of Kirchhoff migrated depth sections in isomeric and anisomeric exponential media. Furthermore the figure is structured in the same way as Fig. 2.15. The amplitude scaling is equal for the two unfiltered sections and the six filtered sections. In all sections the strong amplitudes between depths of 0 and 10 km corresponds to the migrated direct wave. In the isomeric case we observe that the energy of the arrivals of the heterogeneous zone (see Fig. 2.15) is mainly repositioned to depths between z=20 and z=40 km. Therefore ,in the isomeric

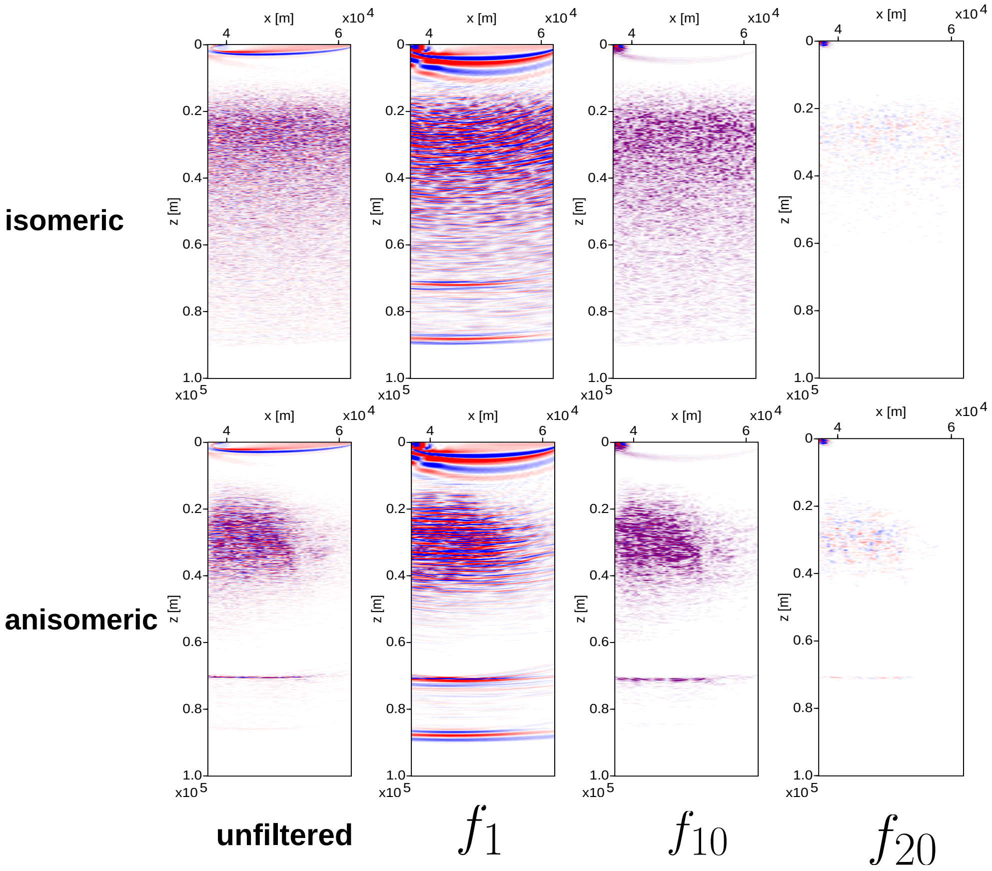

Figure 2.21: Migration results for **exponential** media for the section containing the whole frequency range and three bandpass filtered sections. Isomeric means $a_x = a_z = 200$ m and anisomeric means $a_x = 4000$ m and $a_z = 200$ m. Two amplitude scales are used. One for the two unfiltered sections and another for the six filtered sections.

case, the deep reflector at 70 km depth is no longer covered by scattered energy and clearly visible in the f_1 section. It is not visible in the f_{10} and f_{20} section, hence we assume that in this case there is no energy emerging from the deep reflector. The heterogeneous zone in the isomeric f_1 section appears as a thin layered media due to bad horizontal resolution in comparison to better vertical resolution (Sheriff and Geldart, 1999, p.177). In all anisomeric sections we recognise the heterogeneous zone between 20 and 40 km depth and the deep reflection at 70 km depth. In both f_1 sections, isomeric and anisomeric, we observe a second deep reflection at 90 km depth. This reflection emerges from the lower model boundary. Another interesting observation indicates that there is no repositioned energy in the image of the

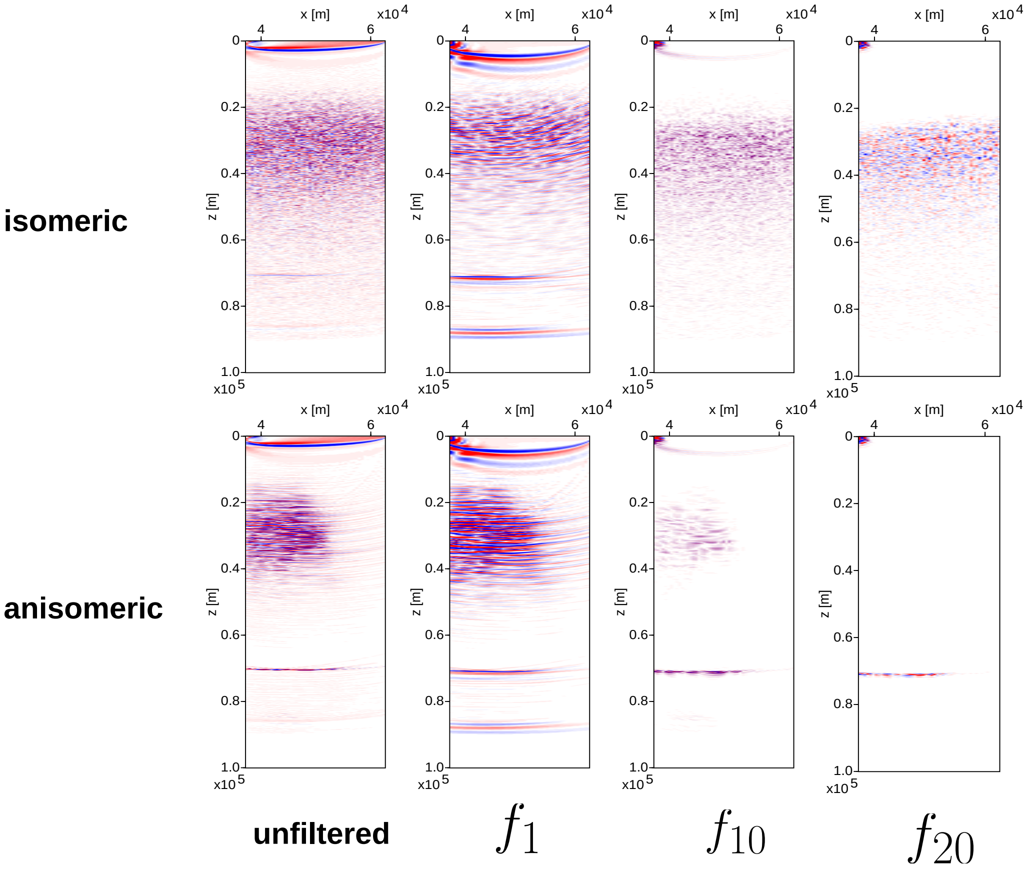

Figure 2.22: Migration results for **Gaussian** media for the section containing the whole frequency range and three bandpass filtered sections. Isomeric means $a_x = a_z = 200$ m and anisomeric means $a_x = 4000$ m and $a_z = 200$ m. Two amplitude scales are used. One for the two unfiltered sections and another for the six filtered sections.

anisomeric heterogeneities for x coordinates of more than approximately 55 km. Fig. 2.23 illustrates a possible interpretation. In isomeric media the recorded scattered energy emerges from heterogeneities beneath receivers at the end of the profile, whereas in anisomeric media the scattered energy from such heterogeneities reaches the surface outside the profile. The propagation of the backscattered or reflected wave in anisomeric media is similar to normal reflection at a stack of thin layers where Snells law is applicable. This assumption is assured by snapshots in Fig. 2.5 and Fig. 2.6. There we observe in the anisomeric case and 10 seconds of propagation a series of reflected wavefronts, similar to those of simple reflection processes. For snapshots in an isomeric media and 10 seconds of propagation we do not observe

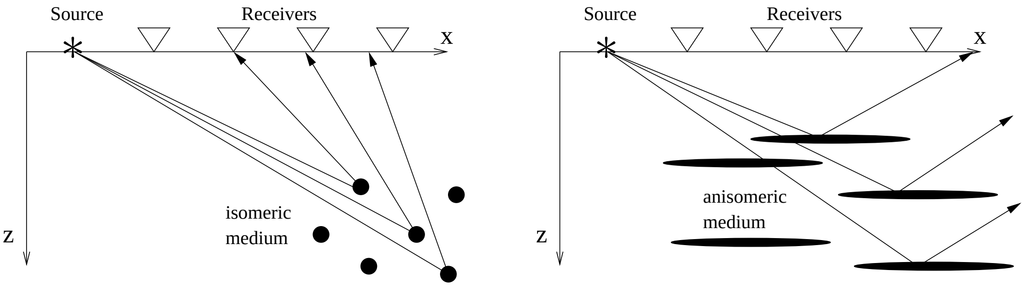

Figure 2.23: Illustration of scattering and reflection in isomeric and anisomeric media in order to explain the migration results.

such wavefronts but scattered energy where no direction of propagation is recognisable.

Description and Interpretation of Fig. 2.22: Illustrated are two unfiltered and six frequency band pass filtered samples, of Kirchhoff migrated depth sections in isomeric and anisomeric Gaussian media. The figure is based on the description of Fig. 2.16 and is structured in the same way as Fig. 2.21. We observe the same characteristic trends as in Fig. 2.21 and therefore only the differences are discussed. The deep reflector at 70 km depth is visible for the unfiltered isomeric section as well. As we have already observed in the unmigrated sections the amplitudes in the isomeric case are of the same magnitude in all three frequency ranges (f_1,f_{10} and f_{20}), whereas in the anisomeric case the amplitudes in the f_{20} section are that weak that for the given amplitude scaling the heterogeneous zone is not visible.

2.3 Analysis of the depth image of the heterogeneous zone

In this chapter we quantify the migrated depth sections in terms of mean energy within the heterogeneous zone. We calculate this energy for all 21 frequency ranges and plot it versus frequency. The idea is to observe a dependency between the statistical parameters of the heterogeneous medium and the mean energy.

2.3.1 Determination of the Scattering Energy

The square of the amplitude is proportional to the energy of the seismic wave. To determine the scattering energy we calculate the mean energy A_k by defining a window W in the depth section and sum up the squared amplitudes inside this window divided by the number of samples N:

$$A_k = \sum_{i=x_1}^{x_2} \sum_{j=z_1}^{z_2} \frac{1}{N} \mid M_k(x_i, z_j) \mid^2 \tag{2.49}$$

where subscript k indicates the index of the RIS section (see Fig. 2.14). $M_k(x, z)$ is the corresponding amplitude at the position (x, z) in the section. To take into account the size of the area W we define three different windows (see Fig. 2.24) with $dx = x_2 - x_1$ and $dz = z_2 - z_1$.

We illustrate A_k for different exponential distributed heterogeneities and different windows W in Fig. 2.25. From top to bottom the figure shows A_k for large, medium and small windows W.

large window All curves for all realizations have the same qualitative characteristic whereas the absolute values of the curves differs. The common qualitative characteristic is expressed in a maximum for low frequencies at approximately 5 Hz and a continuous decay to higher frequencies. The different absolute values of A_k are expressed in a dependency on σ and a_x. For increasing σ and a_x we observe a trend to larger A_k values. Interestingly the curves for $a_x = 500$ m, $a_x = 4000$ m and $a_x = 6000$ m are close together. This indicates a saturation of the mean energy for $a_x \geq 500$ m.

medium window We observe the same qualitative and quantitative trends as for the large window with the following exceptions: The values of

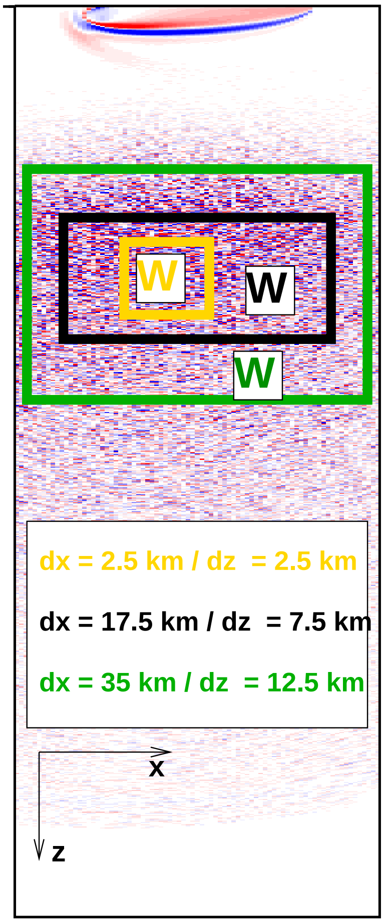

Figure 2.24: Three different windows are used for the determination of A_k

A_k in all frequency ranges are approximately twice as large as in the large window. This is reasonable as the large window takes into account amplitudes at the upper and lower boundary of the image of the heterogeneous zone, where the amplitudes weaken. Furthermore we recognise that only the curves for $a_x \geq 4000$ m are close together anymore whereas the curve for $a_x = 500$ m has distinctly smaller A_k values. Obviously, in contrast to the large window, the saturation of the mean energy occurs for correlation lengths not less than 4000 m. The maximum of all curves is slightly shifted to higher frequencies.

small window Only the differences to the previous case are discussed. The shift to higher frequencies is larger especially for all curves with $a_x \geq$ 4000 m. The characteristic of this curves significantly differ to that of the remaining curves. This is obvious as the x dimension of the small window is smaller than the horizontal correlation length $a_x = 4000$ m.

In Fig. 2.26 we illustrate A_k for Gaussian distributed heterogeneities with a standard deviation $\sigma = 20$ % and different horizontal correlation lengths a_x. Again we take into account three different window sizes. We only realized three different models with Gaussian distributed heterogeneities.

large window The maximum of all three curves is at frequencies of approximately 5 Hz. We observe a decay to higher frequencies. In contrast to the results in exponential distributed media the intensity of the decay depends on a_x. The larger a_x is the stronger is the decay. This results in A_k values of almost zero for the heterogeneities with $a_x = 4000$ m. We already realized this behaviour in the depth images in Fig. 2.21 and Fig. 2.22. There, the isomeric heterogenous zone is visible even in the section for high frequencies ($f_{20} \approx 27$ Hz) whereas it is not visible in the anisomeric f_{20} section. All three curves have a common intersection point at ≈ 11 Hz.

medium window Only the differences to the results for a large window are discussed. The A_k values are approximately 30% larger than in the large window. The maximum and the intersection point are slightly shifted to higher frequencies. The maximum is at about 6 Hz and the intersection point at about 13 Hz.

small window Only the differences to the previous case are discussed. The characteristic of the curve for $a_x = 4000$ m changes for frequencies between 0 and 10 Hz. There is no isolated maximum any more, but A_k is approximately constant (half as large as the maximum in the large or medium window) for this frequency range. The maximum of the other two curves is slightly shifted to higher frequencies and is at about 7 Hz. The intersection point at 13 Hz is a minimum of the curves with $a_x = 200$ m or $a_x = 300$ m. Furthermore there is another maximum of A_k between frequencies of 18 and 24 Hz.

A comparison of this results with the depth sections in Fig. 2.21 and Fig. 2.22 shows that high energies (i.e. A_k) in the heterogeneous zone do not indicate a bad quality of deep reflections below this zone as we observed the best quality of the deep reflector image for strongly anisomeric media. Furthermore our motivation to find a maximum of A_k which is correlated to the horizontal correlation length is not satisfied as we observe the same maxima for all a_x.

But in exponential media we found a dependency between A_k, a_x and the window size as the maximum of A_k for media with a_x greater than the x dimension of the window is distinctly shifted towards higher frequencies in comparison to the common maxima of A_k for media with smaller a_x. The same is true for Gaussian media where the shifted isolated maxima is replaced by a frequency range for which A_k becomes constant. This could be a method to classify the heterogeneous media in terms of correlation lengths. However, the concluding question is how large the scattering part in A_k is? Therefore we take into account common scattering theories and formulate an expression for the scattering coefficient in Chapter 3.

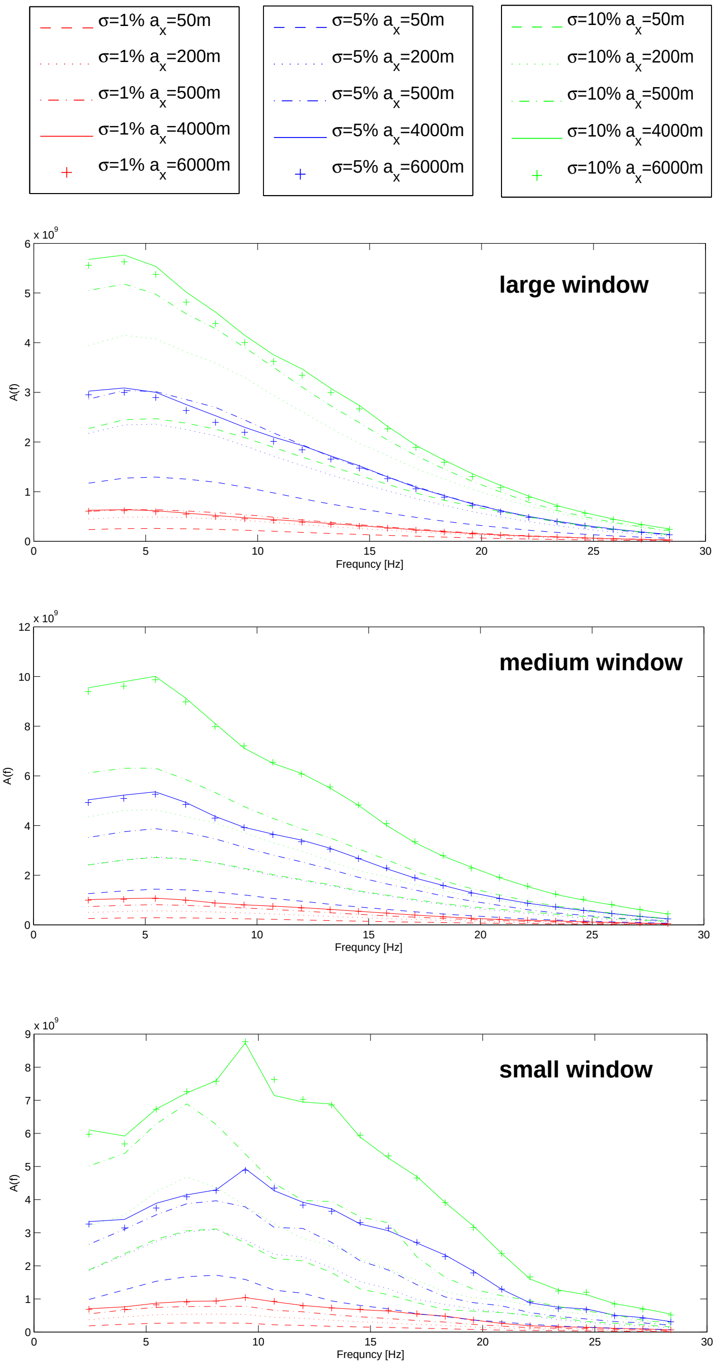

Figure 2.25: Mean energy A_k versus frequency for **exponential** distributed heterogeneities with different standard deviations σ and horizontal correlations lengths a_x. The vertical correlation length is $a_z = 200\ m$ for all realizations. Each plot corresponds to a certain window W in the migrated section.

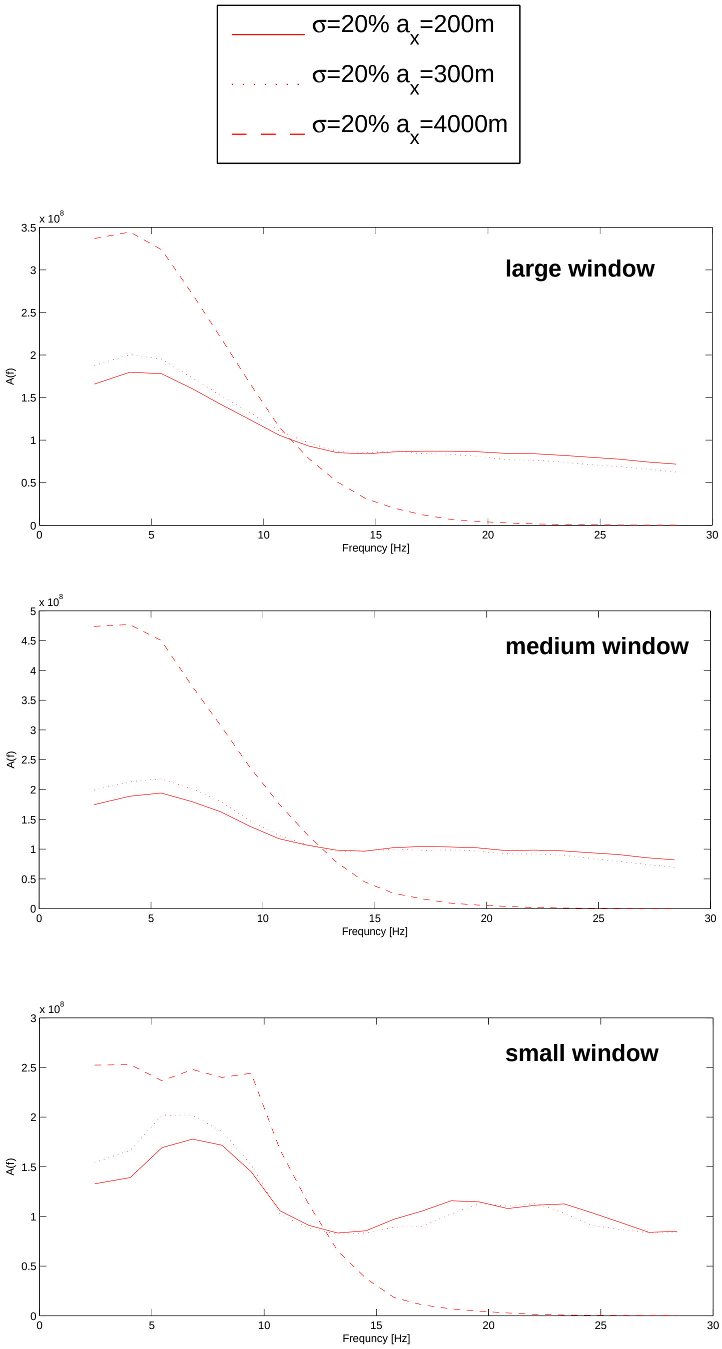

Figure 2.26: Mean energy A_k versus frequency for **Gaussian** distributed heterogeneities with a standard deviations $\sigma = 20\%$ and different horizontal correlations lengths a_x. The vertical correlation length is $a_z = 200\ m$ for all realizations. Each plot corresponds to a certain window W in the migrated section.

Chapter 3

Analytical Studies

In this section we introduce theoretical approaches in order to explain phenomena which occurred for our numerical experiment. In particular this is the high quality of the deep reflector for anisomeric media in comparison to the bad quality for isomeric media. Therefore we derive an analytical solution for the scattering power in isomeric as well as anisomeric media. A comparison of the analytical solution for backscattering with our summation curves shall bring insights into the nature of our results. Furthermore we discuss the averaging effect in anisomeric media for high frequencies.

3.1 Scattering Regimes

Scattering is a phenomena depending on three regulating parameters: The scatterer scale described by the correlation length a, the frequency ω described by the wave number k and the travel distance L. Referring to these parameters we introduce the $ka - L/a$ plane (see Fig. 3.1) and differentiate several scattering regimes.

If $ka = 1$, the scatterer dimension and the wavelength of an incident wave field are of the same order. This regime is often referred to as the **Mie Scattering** regime or resonance regime due to the common assumption that strongest scattering is localised in this regime. Moving to lower frequencies with $ka < 0.1$ leads to the **Rayleigh Scattering** regime. Here, the wavelength is larger than the scatterer dimension and the scattering power is proportional to k^{d+1} with d equal to 1,2 or 3 for a 1D, 2D or 3D medium. Moving to higher frequencies with $ka > 10$, scattering occurs dominantly in

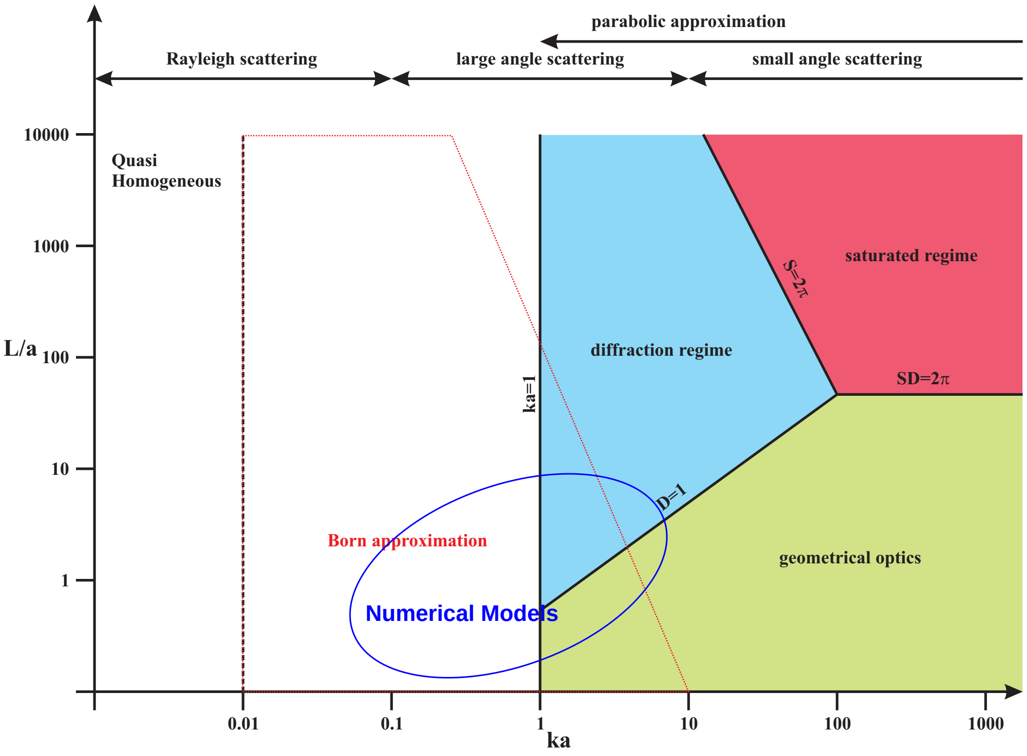

Figure 3.1: Classification of scattering into different regimes. For this plot we set $\sigma = 10\%$. The image is taken from Sick (2002).

forward direction. Since the forward scattering direction is characterised by a scattering angle of 0°, it is identical to **small angle scattering**. Here, for short travel distances, the laws of geometrical optics are relevant. We can speak of simple reflection and transmission interactions and the usage of Snells law is allowed. For the Mie and the small angle scattering regime two more parameters separate further sub-regimes:

$$S = \sigma\zeta ka\sqrt{\frac{L}{a}} \tag{3.1}$$

$$D = 2L/ka^2. \tag{3.2}$$

S denotes the scattering strength and D is a wave parameter. Furthermore σ denotes the standard deviation of the velocity fluctuation and $\zeta = a_z/a$ the ratio of the characteristic scale in propagation direction to the overall correlation length. This definition of S indicates the strongest scattering power for isomeric media with $a_z = a$. The size of σ denotes whether we can speak of weak or strong wave field fluctuations. Most scattering theories are based on a weak fluctuation assumption characterised by $|u^I| \gg |u^S|$, with u^I the incident wave field and u^S the scattered field. For $ka > 1$, $D > 1$ and $SD < 2\pi$ diffraction has a strong influence on the wave propagation, hence we call this regime the diffraction regime. The saturated regime is defined by $S > 2\pi$ and $SD > 2\pi$. It is dominated by multiple scattering and coherent backscattering. Localisation effects can occur (Müller, 2001).

3.2 Seismic scattering using the Born Approximation

The Born approximation is based on the solution of the wave equation for a wave field $u(\vec{r}, t) = u^I(\vec{r}, t) + u^S(\vec{r}, t)$ where $|u^I| \ll |u^S|$. u^I is the incident undisturbed wave field and u^S is the scattered wave field. Therefore it is a weak fluctuation theory. In our models we have chosen σ to be 1% and 5%, which is suitable for the Born approximation, and 10% and 20%, which becomes critical for the application of the Born approximation. Furthermore, we need a large distance r to the scattering object by accomplishing $r \gg (1/\pi)a^2k$. In our case the heterogeneous zone is located 31 km away from the receivers, our maximum correlation length is 4km and our central frequency is about 13 Hz. This results in 31 km > 11 km. For higher frequencies we move further away from the Born conditions. In Fig. 3.1 the range of the Born approximation is marked by a red dotted line. Additionally the location of the numerical models in the ka-L/a plane is marked in Fig. 3.1 assuming a minimum frequency of 3 Hz and a maximum frequency of 30 Hz. We notice that the Born approximation is applicable except for high frequencies and large correlation lengths as it is for models with $a_x \geq 4000$ m and frequencies larger than approximately 15 Hz. Furthermore the classification of scattering, as it is shown in Fig.3.1, is based on an isomeric assumption.

3.3 Scattering Coefficient

The scattering coefficient g is an appropriate quantity in order to describe scattering characteristics. It is the scattering power per unit volume. Fig. 3.2 illustrates the quantities which are necessary for the formulation of the scattering coefficient g. An incident wave with energy-flux density J_0 inter-

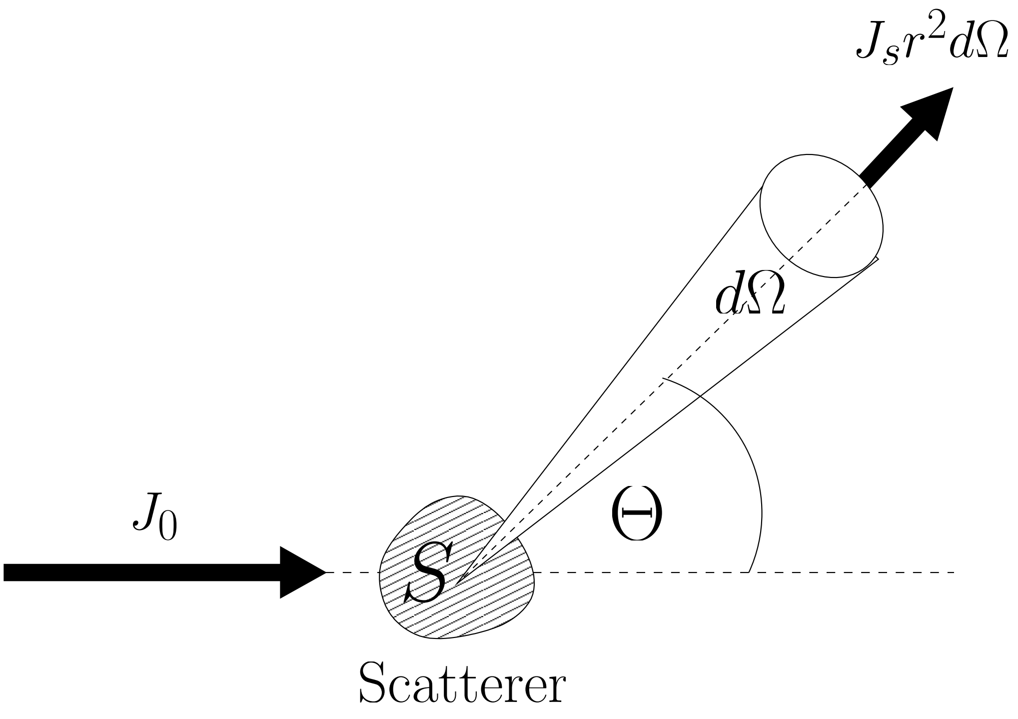

Figure 3.2: Differential cross section for a single scattering surface S.

acts with a scattering volume and creates an outgoing wave. The outgoing wave has the energy-flux density J_s. The energy-flux density is the amount of energy passing a unit surface perpendicular to the propagation direction per unit time. The energy scattered per unit time into the solid angle $d\Omega$ is given by $J_s r^2 d\Omega$. The ratio of the incoming intensity to the outgoing intensity per solid angle is commonly referred to as the differential scattering cross section:

$$d\sigma = \frac{J_s r^2 d\Omega}{J_0}. \tag{3.3}$$

For a medium filled with point like scatterers, g is defined as the product of 4π times the scatterer density n with the differential scattering cross section

$$g = 4\pi\ n\ d\sigma. \tag{3.4}$$

The total scattering coefficient g_0 is the average over all solid angles

$$g_0 = \frac{1}{4\pi} \oint g \; d\Omega = n \oint d\sigma \; d\Omega = n \; \sigma_0. \tag{3.5}$$

g has the dimension of a reciprocal length and can therefore considered as the undisturbed free mean path.

For a continuous medium we define $g(\theta)$ as 4π times the average scattered power in θ direction per unit solid angle by a unit volume V of a random medium for a unit incident field (i.e. unit flux density) (Wu and Aki, 1985)

$$g(\theta) = \frac{4\pi r^2}{V} \langle |\vec{U}^S(x, y, z, t|^2 \rangle. \tag{3.6}$$

where U^S is the scattered wave field and r the scatterer-receiver distance. In our numerical experiment the scattered wave field consists of P-wave and converted S-wave parts. Therefore the total scattered field is $\vec{U}^S = \vec{U}^S_{pp} + \vec{U}^S_{ps}$. Furthermore we have to consider a 2D case. Then equation (3.6) becomes

$$g(\theta) = \frac{2\pi r}{S} \langle |\vec{U}^S(x, z, t)|^2 \rangle. \tag{3.7}$$

where S denotes a unit surface.

3.4 Derivation of the scattering coefficient using the Born Approximation for Elastic Single Scattering

The aim is to extract the scattered wave field for both, direct PP and conversional PS scattering ($\vec{U}^S_{pp}, \vec{U}^S_{ps}$). The scattered wave emerges due to the interaction of an incident wave with a distributed elastic heterogeneity characterised by a specific auto correlation function, either Gaussian or exponential. The Born approximation for elastic scattering is based on the solution of the isotropic elastodynamic wave equation. One important component is the separation of the wave field $\vec{u}$ into an undisturbed incident part $\vec{u^I}$ and a disturbed scattered part $\vec{u^S}$. The complete wave field is the sum of both parts

$$\vec{u} = \vec{u^I} + \vec{u^S} \tag{3.8}$$

where we assume that $|\vec{u^S}| \ll |\vec{u^I}|$. For the elastic case we have to take into account the spatial variation of all elastic parameters which are

$$\begin{aligned} \lambda(x,z) &= \lambda_0 + \delta\lambda(x,z) \quad \text{with} \quad \left|\frac{\delta\lambda}{\lambda_0}\right| \ll 1 \\ \mu(x,z) &= \mu_0 + \delta\mu(x,z) \quad \text{with} \quad \left|\frac{\delta\mu}{\mu_0}\right| \ll 1 \\ \rho(x,z) &= \rho_0 + \delta\rho(x,z) \quad \text{with} \quad \left|\frac{\delta\rho}{\rho_0}\right| \ll 1 \end{aligned} \tag{3.9}$$

where subscript 0 indicates the average value.

The following derivation of $\vec{U}_{pp}^S$ and $\vec{U}_{ps}^S$ for a 2D case is taken from Sato and Fehler (1998) and Hong and Kennet (2003).

The elastodynamic wave equation for $\vec{u^I}$ is homogeneous

$$\begin{aligned} \rho_0 \frac{\partial^2 u_x^I}{\partial t^2} &= \frac{\partial \sigma_{xx}^I}{\partial x} + \frac{\partial \sigma_{xz}^I}{\partial z}, \\ \rho_0 \frac{\partial^2 u_z^I}{\partial t^2} &= \frac{\partial \sigma_{xz}^I}{\partial x} + \frac{\partial \sigma_{zz}^I}{\partial z}. \end{aligned} \tag{3.10}$$

ρ_0 is the background density. The undisturbed stress components σ_{xx}^I, σ_{zz}^I and σ_{xz}^I are related with the average Lamé parameters λ_0 and μ_0 by the theory of elasticity:

$$\begin{aligned} \sigma_{xx}^I &= (\lambda_0 + 2\mu_0)\frac{\partial u_x^I}{\partial x} + \lambda_0 \frac{\partial u_z^I}{\partial z}, \\ \sigma_{zz}^I &= (\lambda_0 + 2\mu_0)\frac{\partial u_z^I}{\partial z} + \lambda_0 \frac{\partial u_x^I}{\partial x}, \\ \sigma_{xz}^I &= \mu_0 \left(\frac{\partial u_x^I}{\partial z} + \frac{\partial u_z^I}{\partial x}\right). \end{aligned} \tag{3.11}$$

The next step is the essential step characterising the Born approximation. We obtain the elastic wave equation for $\vec{u}$ by substituting $\vec{u}^I$ in equation (3.10) by $\vec{u}^I + \vec{u}^S$ in equation (3.8). For $\vec{u}^S$ the corresponding Lamé parameters are $\delta\mu$ and $\delta\lambda$ and the corresponding density is $\delta\rho$. We neglect terms including only $\delta\lambda$, $\delta\mu$, $\delta\rho$ and $\vec{u}^S$ as we have assumed them to be small. Furthermore we consider the homogeneity of equation (3.10). With these assumptions we obtain

$$\begin{aligned}\rho_0\frac{\partial^2 u_x^S}{\partial t^2} &- \frac{\partial\sigma_{xx}^S}{\partial x}+\frac{\partial\sigma_{xz}^S}{\partial z}=F_x^S,\\ \rho_0\frac{\partial^2 u_z^S}{\partial t^2} &- \frac{\partial\sigma_{xz}^S}{\partial x}+\frac{\partial\sigma_{zz}^S}{\partial z}=F_z^S\end{aligned}\tag{3.12}$$

where σ^S are the disturbed stress parameters. The external force $F_i^S(i=x,z)$ represents the scattering effects of the heterogeneous medium and can be obtained from the incident P-wave and the fluctuation of Lamé parameters and density. It is of the form (Sato and Fehler, 1998, equation (4.35)):

$$\begin{aligned}F_i^S(x,z,t)= &-\delta\rho\tfrac{\partial^2 u_i^I}{\partial t^2}+\partial_i\delta\lambda\partial_j u_j^I+\partial_j\delta\mu(\partial_i u_j^I+\partial_j u_i^I)\\ &+\delta\lambda\partial_i\partial_j u_j^I+\delta\mu\partial_j(\partial_i u_j^I+\partial_j u_i^I).\end{aligned}\tag{3.13}$$

Although we use a pressure point source in our numerical models, we assume that the undisturbed wave $\vec{u^I}$ is a plain P wave propagating in z-direction.

$$u_x^I=0 \quad \text{and} \quad u_z^I=e^{i(k_p z-\omega t)}\tag{3.14}$$

where k_p is the P-wave number ($=\omega/V_{0p}$), ω the angular frequency and V_{0p} is the P-wave background velocity. With equation (3.14) equation (3.13) becomes

$$\begin{aligned}F_x^S &= -ik_p\frac{\partial}{\partial x}\delta\lambda u_z^I\\ F_z^S &= -\left[k_p^2(V_{0p}^2\delta\rho-\delta\lambda-2\delta\mu)+ik_p\frac{\partial}{\partial z}(\delta\lambda+2\delta\mu)\right]u_z^I.\end{aligned}\tag{3.15}$$

In chapter 2.1.2 we introduced the fractional fluctuation term $\xi(x,z)$ which describes velocity field fluctuations. We related the P-wave and the S-wave velocity by a factor of $\sqrt{3}$. Hence, the fluctuations of both are equal. The density was related to the P-wave velocity by the empirical Nafe-Drake relation

$$\rho=1.755+0.155v_p\;[g/cm^3].\tag{3.16}$$

Therefore the density fluctuation differs to the velocity fluctuation by a factor K.

$$\xi(x,z) = \frac{\delta V_p}{V_{0p}} = \frac{\delta V_s}{V_{0s}} = \frac{1}{K}\frac{\delta\rho}{\rho_0}. \tag{3.17}$$

K can be calculated referring to equation (3.16):

$$\frac{\delta\rho}{\rho_0} = \left(\frac{V_{0p}}{V_{0p}+1.755}\right)\frac{\delta V_p}{V_{0p}} \tag{3.18}$$

Relating to the numerical experiment where V_{0p} was 6 km/s, K is approximately 0.78. The elastic parameters and the seismic velocities are related by

$$V_p = \sqrt{\frac{\lambda(x,z)+2\mu(x,z)}{\rho(x,z)}} \quad \text{and} \quad V_s = \sqrt{\frac{\mu(x,z)}{\rho(x,z)}}. \tag{3.19}$$

With equation (3.14), (3.17) and (3.19) we can rewrite equations (3.15):

$$\begin{aligned} F_x^s &= -ik_pV_{0p}^2\,\rho_0\,C_1\frac{\partial\xi}{\partial x}\,\exp[i(k_pz-\omega t)], & (3.20)\\ F_z^s &= \left(2k_p^2V_{0p}^2\,\rho_o\,\xi - ik_pV_{0p}^2\,\rho_0\,C_2\frac{\partial\xi}{\partial z}\right)\,\exp[i(k_pz-\omega t] & (3.21)\end{aligned}$$

where C_1 and C_2 are:

$$\begin{aligned} C_1 &= (K+2)\left(1-\frac{2V_{0s}^2}{V_{0p}^2}\right)\\ C_2 &= K+2. \end{aligned} \tag{3.22}$$

With the information we obtained until now a solution for u_i^s in equation (3.12) can be expressed using the principle of Green functions. Generally, the Greens function is the response of the system to a point source which is mathematically described by the δ-function. In our case the system is described by the elastodynamic wave equation (3.12). We denote the Greens function $G_{jk}(x,z,t)$ as the jth component of the displacement field caused by a point source directed in the kth direction. Therefore G satisfies equation (3.12):

$$\begin{aligned} \rho_0 \frac{\partial^2 G_{xk}}{\partial t^2} &= \frac{\partial \sigma_{xx}(G_{xk})}{\partial x} + \frac{\partial \sigma_{xz}(G_{xk})}{\partial z} = \delta_{xk}\delta(t)\delta(x), \\ \rho_0 \frac{\partial^2 G_{zk}}{\partial t^2} &= \frac{\partial \sigma_{xz}(G_{xk})}{\partial x} + \frac{\partial \sigma_{zz}(G_{zk})}{\partial z} = \delta_{zk}\delta(t)\delta(z). \end{aligned} \tag{3.23}$$

The principle of superposition states that the response to a sum of single point forces is equal to the sum of the responses. Furthermore we can express every force as a sum of different point forces. Therefore, we can express the response to an arbitrary force as a convolution integral between the Greens function and the arbitrary force. The application to this case yields:

$$\begin{aligned} u_x^S(x,z,t) &= \sum_{k=1}^{2} \int_S F_k^S G_{xk} dS \\ u_z^S(x,z,t) &= \sum_{k=1}^{2} \int_S F_k^S G_{zk} dS. \end{aligned} \tag{3.24}$$

with $k = (x, z)$. The surface S is the area of heterogeneity. For the 2D case $G_{jk}(x, z, t)$ is a tensor of the form

$$\begin{pmatrix} G_{xx} & G_{xz} \\ G_{zx} & G_{zz}. \end{pmatrix} \tag{3.25}$$

The analytical solution of G is given by (Hudson, 1980, p.45):

$$\begin{aligned} G_{jk}(x,z,t) = \tfrac{1}{4\pi\rho} \Bigg\{ & \|P_{jk}\| \tfrac{H(t-r/V_p)}{V_p^2\sqrt{t^2-r^2/V_p^2}} + (\mathcal{I}_{jk} - \|P_{jk}\|) \tfrac{H(t-r/V_s)}{V_s^2\sqrt{t^2-r^2/V_s^2}} \\ & -\tfrac{1}{r^2}(\mathcal{I}_{jk} - 2\|P_{jk}\|) \Big[H(t-r/V_p)(V_p^2\sqrt{t^2-r^2/V_p^2}) \\ & -H(t-r/V_s)(V_s^2\sqrt{t^2-r^2/V_s^2})) \Big] \Bigg\} \end{aligned} \tag{3.26}$$

with $j = x, z$, $k = x, z$, $\mathcal{I}$ is the unit matrix , $\|P_{jk}\|$ is a polarisation matrix and $H(t-r/V)$ is the Heavyside step function. The argument of H describes the causality by setting $H = 0$ for $t < r/V$. The solution is therefore a retarded solution. The first term in equation (3.26) describes the P-wave far field, the second term the S-wave far field and the third mixed term

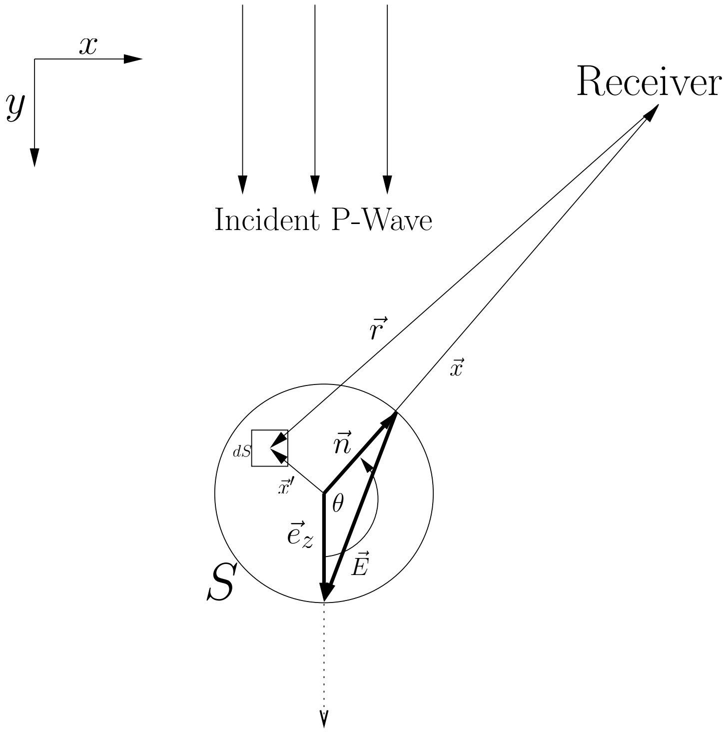

Figure 3.3: An incident P-wave in z-direction interacts with the scatterer dS, a part of the heterogeneous zone S. The scattered wave is propagating in the direction of $\vec{r}$ and the scattering angle is θ. $\vec{E}$ denotes the exchange vector whereas $\vec{n}$ is a unit vector in $\vec{x}$ direction and $\vec{e}_z$ a unit vector in z-direction. $\vec{x}$ and $\vec{x}'$ denote the position of the receiver and the scatterer, respectively.

the near field. In this case, the near field term becomes extremely small as the observation distance is a lot larger than the dimension of the scattering elements and can therefore be neglected. With respect to the scattering angle θ between the vertical axes and the scattered wave propagation direction, the polarisation matrix $\|P_{jk}\|$ is:

$$\|P_{jk}\| = \begin{pmatrix} sin^2\theta & sin\theta cos\theta \\ cos\theta sin\theta & cos^2\theta \end{pmatrix}. \tag{3.27}$$

Then, for a vertical directed point force the far field term of G for P-waves and S-waves can be written as

$$\begin{pmatrix} G^P_{xz} \\ G^P_{zz} \end{pmatrix} = \frac{cos\theta}{4\pi V_p^2 \rho} \begin{pmatrix} sin\theta \\ cos\theta \end{pmatrix} \frac{H(t - r/V_p)}{\sqrt{t^2 - r^2/V_p^2}} \tag{3.28}$$

and

$$\begin{pmatrix} G^S_{xz} \\ G^S_{zz} \end{pmatrix} = \frac{sin\theta}{4\pi V_s^2 \rho} \begin{pmatrix} -cos\theta \\ sin\theta \end{pmatrix} \frac{H(t - r/V_p)}{\sqrt{t^2 - r^2/V_p^2}}. \tag{3.29}$$

Following Roth and Korn (1992), the Fourier transform of $H(t-r/V)/\sqrt{t^2 - (r/V)^2}$ can be replaced by the Hankel function of the first order $H_0^{(1)}$

$$\mathcal{F}\left[\frac{H(t - r/V)}{\sqrt{t^2 - r^2/V^2}}\right] = i\pi H_0^{(1)}(\omega r/V). \tag{3.30}$$

ω is the angular frequency and V the wave velocity. Applying equation (3.30) to equations (3.28) and (3.29) and writing $r = |\vec{x} - \vec{x'}|$ we obtain:

$$\begin{pmatrix} \tilde{G}^P_{xz} \\ \tilde{G}^P_{zz} \end{pmatrix} = \frac{icos\theta}{4V_p^2 \rho} H_0^{(1)}(k_p|\vec{x} - \vec{x'}|) \begin{pmatrix} sin\theta \\ cos\theta \end{pmatrix}, \tag{3.31}$$

and

$$\begin{pmatrix} \tilde{G}^S_{xz} \\ \tilde{G}^S_{zz} \end{pmatrix} = \frac{isin\theta}{4V_s^2 \rho} H_0^{(1)}(k_s|\vec{x} - \vec{x'}|) \begin{pmatrix} -cos\theta \\ sin\theta \end{pmatrix}. \tag{3.32}$$

If the distance $|\vec{x} - \vec{x'}|$ is large compared to the wavelength the asymptotic approximation of $H_0^{(1)}$ can be used (Roth and Korn, 1992)

$$H_0^{(1)}(k|\vec{x} - \vec{x'}|) \approx \sqrt{\frac{2}{\pi k|\vec{x} - \vec{x'}|}} \exp\left[-i\left(k|\vec{x} - \vec{x'}| - \frac{\pi}{4}\right)\right]. \tag{3.33}$$

For a large observation distance we may use the approximations $1/|\vec{x} - \vec{x'}| \approx 1/|\vec{x}|$ for the denominator and $|\vec{x} - \vec{x'}| \approx |\vec{x}| - \vec{n} \cdot \vec{x'}$ for the exponent where $\vec{n}$ is the unit vector in scattering direction. Then, together with equation (3.33), equations (3.31) and (3.32) become

$$\begin{pmatrix} \tilde{G}^P_{xz} \\ \tilde{G}^P_{zz} \end{pmatrix} = \frac{i}{4V_p^2 \rho}\sqrt{\frac{2}{\pi k_p|\vec{x}|}} \exp\left[i\left(k_p|\vec{x}| - k_p\vec{n} \cdot \vec{x'} - \frac{\pi}{4}\right)\right] \begin{pmatrix} sin\theta cos\theta \\ cos^2\theta \end{pmatrix}, \tag{3.34}$$

and

$$\begin{pmatrix} \tilde{G}^S_{xz} \\ \tilde{G}^S_{zz} \end{pmatrix} = \frac{i}{4V_s^2\rho}\sqrt{\frac{2}{\pi k_s|\vec{x}|}}\,\exp\left[i\left(k_s|\vec{x}| - k_s\vec{n}\cdot\vec{x'} - \frac{\pi}{4}\right)\right]\begin{pmatrix} -sin\theta cos\theta \\ sin^2\theta \end{pmatrix}. \tag{3.35}$$

The components G_{xx} and G_{zx} of the Greens function tensor for a horizontally directed point source can be obtained in the same way. Following Hong and Kennet (2003) a complete formulation of the Greens function for the far field can be written as

$$\begin{aligned} \tilde{G}^P_{jk} &= \frac{i}{4V_p^2\rho}\sqrt{\frac{2}{\pi k_p|\vec{x}|}}\,\exp\left[\left(k_p|\vec{x}| - k_p\vec{n}\cdot\vec{x'} - \frac{\pi}{4}\right)\right]A^P_{jk}(\theta), \\ \tilde{G}^S_{jk} &= \frac{i}{4V_s^2\rho}\sqrt{\frac{2}{\pi k_s|\vec{x}|}}\,\exp\left[\left(k_s|\vec{x}| - k_s\vec{n}\cdot\vec{x'} - \frac{\pi}{4}\right)\right]A^S_{jk}(\theta) \end{aligned} \tag{3.36}$$

The coefficient A specifies the polarisation of the scattered wave field where index j indicates the spatial component of u^s and index k the direction of the point force.

$$\begin{array}{lllllll} A^P_{xx}(\theta) &=& sin^2\theta &,& A^P_{xz}(\theta) &=& sin\theta cos\theta, \\ A^P_{zx}(\theta) &=& -sin\theta cos\theta &,& A^P_{zz}(\theta) &=& cos^2\theta, \\ A^S_{xx}(\theta) &=& cos^2\theta &,& A^S_{xz}(\theta) &=& -sin\theta cos\theta, \\ A^S_{zx}(\theta) &=& sin\theta cos\theta &,& A^S_{zz}(\theta) &=& sin^2\theta, \end{array} \tag{3.37}$$

Referring to equations (3.24) and (3.20) an integral formulation for the scattered P and S-wave field is given by

$$\begin{aligned} u_j^{PP} = & \sqrt{\frac{k_p}{8\pi|\vec{x}|}}\,\exp\left[-i\left(\omega t - k_p|\vec{x}| + \frac{\pi}{4}\right)\right] \\ & \left\{C_1A^P_{jx}(\theta)\int_S \frac{\partial\xi}{\partial x}e^{ik_p(z-\vec{n}\cdot\vec{x'})}dS(\vec{x'})\right. \\ & +2ik_pA^P_{jz}(\theta)\int_S \xi e^{ik_p(z-\vec{n}\cdot\vec{x'})}dS(\vec{x'}) \\ & \left.+C_2A^P_{jz}(\theta)\int_S \frac{\partial\xi}{\partial z}e^{ik_p(z-\vec{n}\cdot\vec{x'})}dS(\vec{x'})\right\}, \end{aligned} \tag{3.38}$$

and

$$\begin{aligned} u_j^{PS} &= \sqrt{\frac{k_p(\gamma)^3}{8\pi|\vec{x}|}} \exp\left[-i\left(\omega t - k_s|\vec{x}| + \frac{\pi}{4}\right)\right] \\ & \left\{C_1 A_{jx}^S(\theta) \int_S \frac{\partial\xi}{\partial x} e^{ik_s(z-\gamma\vec{n}\cdot\vec{x'})} dS(\vec{x'}) \right. \\ & +2ik_p A_{jz}^P(\theta) \int_S \xi e^{ik_p(z-\gamma\vec{n}\cdot\vec{x'})} dS(\vec{x'}) \\ & \left. +C_2 A_{jz}^S(\theta) \int_S \frac{\partial\xi}{\partial z} e^{ik_p(z-\gamma\vec{n}\cdot\vec{x'})} dS(\vec{x'}) \right\}, \end{aligned} \tag{3.39}$$

where $\gamma = (V_p/V_s)$. Integration by parts yields:

$$\begin{aligned} u_j^{PP} &= i\sqrt{\frac{k_p^3}{8\pi|\vec{x}|}} \exp\left[-i\left(\omega t - k_p|\vec{x}| + \frac{\pi}{4}\right)\right] \\ & \left\{C_1 A_{jx}^P(\theta) sin\theta + 2A_{jz}^P(\theta) + C_2 A_{jz}^P(\theta)(cos\theta - 1)\right\} \\ & \int_S \xi e^{ik_p(z-\vec{n})\cdot\vec{x'}} dS(\vec{x'}), \end{aligned} \tag{3.40}$$

and

$$\begin{aligned} u_j^{PS} &= i\sqrt{\frac{k_p^3\gamma^3}{8\pi|\vec{x}|}} \exp\left[-i\left(\omega t - k_s|\vec{x}| + \frac{\pi}{4}\right)\right] \\ & \left\{C_1 A_{jx}^S(\theta)\gamma cos\theta + 2A_{jz}^S(\theta) + C_2 A_{jz}^S(\theta)(\gamma cos\theta - 1)\right\} \\ & \int_S \xi e^{ik_p(z-\vec{n})\cdot\vec{x'}} dS(\vec{x'}). \end{aligned} \tag{3.41}$$

The rotation of the coordinate axes by θ into the scattering direction enables a limitation of U_j^{PP} to a single radial component and of U_j^{SS} to a single tangential component (see Fig. 3.3)

$$\begin{aligned} u_r^{PP} &= sin(\theta)u_x^{PP} + cos(\theta)u_z^{PP} \\ u_t^{PS} &= cos(\theta)u_x^{PS} - sin(\theta)u_z^{PS} \end{aligned} \tag{3.42}$$

where subscript t denotes the tangential and subscript r the radial component. We simplify equations (3.40) and (3.41) by introducing two parameters $C_r(\theta)$ and $C_t(\theta)$:

$$\begin{array}{rcll} C_r(\theta) & = & sin\theta & \Big\{C_1 A^P_{xx}(\theta) sin\theta + 2A^P_{xz}(\theta) + C_2 A^P_{xz}(\theta)\Big(cos\theta - 1\Big)\Big\} \\ & & +cos\theta & \Big\{C_1 A^P_{zx}(\theta) sin\theta + 2A^P_{zz}(\theta) + C_2 A^P_{zz}(\theta)\Big(cos\theta - 1\Big)\Big\}, \\ C_t(\theta) & = & cos\theta & \Big\{C_1 A^S_{xx}(\theta)\gamma sin\theta + 2A^S_{xz}(\theta) + C_2 A^S_{xz}(\theta)\Big(\gamma cos\theta - 1\Big)\Big\} \\ & & -sin\theta & \Big\{C_1 A^S_{zx}(\theta)\gamma sin\theta + 2A^S_{zz}(\theta) + C_2 A^S_{zz}(\theta)\Big(\gamma cos\theta - 1\Big)\Big\}. \end{array} \tag{3.43}$$

We remember our goal to calculate the scattering coefficient. We need the average scattered power of the wave field for the calculation of g (see equation (3.7)). To extract it we consider an ensemble average over different realizations of the random medium:

$$\begin{array}{rcl} \langle |u_r^{PP}|^2\rangle & = & \frac{k_p^3}{8\pi|\vec{x}|}[C_r(\theta)]^2 \int\limits_S \int\limits_S \langle \xi(\vec{x'})\xi(\vec{y'})\rangle \\ & & \exp\Big[ik_p\Big(\vec{e_z}\cdot(\vec{x'}-\vec{y'}) - \vec{n}\cdot(\vec{x'}-\vec{y'})\Big)\Big]dS(\vec{x'})dS(\vec{y'}), \\ \langle |u_t^{PS}|^2\rangle & = & \frac{k_p^3\gamma^3}{8\pi|\vec{x}|}[C_t(\theta)]^2 \int\limits_S \int\limits_S \langle \xi(\vec{x'})\xi(\vec{y'})\rangle \\ & & \exp\Big[ik_p\Big(\vec{e_z}\cdot(\vec{x'}-\vec{y'}) - \gamma\vec{n}\cdot(\vec{x'}-\vec{y'})\Big)\Big]dS(\vec{x'})dS(\vec{y'}). \end{array} \tag{3.44}$$

We replace $\vec{x'}$ and $\vec{y'}$ by the center of mass coordinate $\vec{x}_c = \frac{1}{2}(\vec{x'}+\vec{y'})$ and the relative coordinate $\vec{x}_d = \vec{y'} - \vec{x'}$. Also, we introduce the exchange wave number vectors $\vec{E}_r = k_p\vec{e}_z - k_p\vec{n}$ and $\vec{E}_t = k_p\vec{e}_z - k_p\gamma\vec{n}$ (see Fig. 3.3). The surface integral over $\vec{x_c}$ yields the area S and the fluctuation average can be described by an Auto Correlation Function $R(\vec{x}_d)$. Thus, we obtain:

$$\begin{array}{rcl} \langle |u_r^{PP}|^2\rangle & = & \frac{Sk_p^3}{8\pi|\vec{x}|}[C_r(\theta)]^2 \int\limits_S R(\vec{x_d})\exp\Big[-i\Big(\vec{E}_r\cdot\vec{x}_d\Big)\Big]dS(\vec{x}_d), \\ \langle |u_r^{PS}|^2\rangle & = & \frac{Sk_p^3\gamma^3}{8\pi|\vec{x}|}[C_t(\theta)]^2 \int\limits_S R(\vec{x_d})\exp\Big[-i\Big(\vec{E}_t\cdot\vec{x}_d\Big)\Big]dS(\vec{x}_d). \end{array} \tag{3.45}$$

The surface integral in equation (3.45) is the Fourier transform of $R(x_d)$ and therefore the corresponding 'power spectral density function' $P(\vec{E}_r)$ and $P(\vec{E}_t)$ respectively, with the exchange wave number vector as it's argument. We write the exchange wave number vector in terms of the scattering angle θ:

$$\begin{aligned} \vec{E}_r &= \begin{pmatrix} k_x \\ k_z \end{pmatrix} = k_p \begin{pmatrix} -sin\theta \\ 1 - cos\theta \end{pmatrix} \\ \vec{E}_t &= \begin{pmatrix} k_x \\ k_z \end{pmatrix} = k_p \begin{pmatrix} -\gamma sin\theta \\ 1 - \gamma cos\theta \end{pmatrix} \end{aligned} \tag{3.46}$$

and rewrite equation (3.45)

$$\begin{aligned} \langle |u_r^{PP}|^2 \rangle &= \tfrac{Sk_p^3}{8\pi|\vec{x}|}[C_r(\theta)]^2 \; P\Big(\vec{E}_r(k_x, k_z)\Big), \\ \langle |u_t^{PS}|^2 \rangle &= \tfrac{Sk_p^3\gamma^3}{8\pi|\vec{x}|}[C_t(\theta)]^2 \; P\Big(\vec{E}_t(k_x, k_z)\Big). \end{aligned} \tag{3.47}$$

In the numerical study a 2D Gaussian and a 2D exponential PSDF were used:

$$P_{gauss}^{2D}(k_x, k_z) = \frac{\sigma^2(a_x a_z)}{4\pi} e^{-\frac{(k_x^2 a_x^2 + k_z^2 a_z^2)}{4}} \tag{3.48}$$

$$P_{exp}^{2D}(k_x, k_z) = \frac{\sigma^2(a_x a_z)}{2\pi(1 + (k_x^2 a_x^2 + k_z^2 a_z^2))^{\frac{3}{2}}}. \tag{3.49}$$

For further consideration of the heterogeneities a 90° rotated autocorrelation function R^* with the corresponding PSDF $P^*(\vec{E}^*)$ is used (Hong and Wu, 2005)

$$\begin{aligned} \vec{E}_r^* &= \begin{pmatrix} k_x^* \\ k_z^* \end{pmatrix} = k_p \begin{pmatrix} 1 - cos\theta \\ -sin\theta \end{pmatrix} \\ \vec{E}_t^* &= \begin{pmatrix} k_x^* \\ k_z^* \end{pmatrix} = k_p \begin{pmatrix} 1 - \gamma cos\theta \\ -\gamma sin\theta \end{pmatrix}. \end{aligned} \tag{3.50}$$

For the calculation of the average scattered energy we have to put the rotated form of equation (3.48) or equation (3.49) into equations (3.47):

$$\begin{aligned}
\langle|u_r^{PP}|^2\rangle_{exp} &= \frac{Sk_p^3\sigma^2 a_x a_z}{(4\pi)^2|\vec{x}|}\frac{1}{[1+k_p^2((1-cos\theta)^2a_x^2+a_z^2sin^2\theta)]^{\frac{3}{2}}}[C_r(\theta)]^2 \\
\langle|u_r^{PS}|^2\rangle_{exp} &= \frac{S\gamma^3k_p^3\sigma^2 a_x a_z}{(4\pi)^2|\vec{x}|}\frac{1}{[1+k_p^2((1-\gamma cos\theta)^2a_x^2+a_z^2\gamma^2sin^2\theta)]^{\frac{3}{2}}}[C_t(\theta)]^2 \\
\langle|u_t^{PP}|^2\rangle_{gauss} &= \frac{Sk_p^3\sigma^2 a_x a_z}{32\pi^2|\vec{x}|}\exp\left[\frac{[k_p^2(a_x^2(1-cos\theta)^2+a_z^2sin^2\theta)]}{4}\right][C_r(\theta)]^2 \\
\langle|u_t^{PS}|^2\rangle_{gauss} &= \frac{S\gamma^3k_p^3\sigma^2 a_x a_z}{32\pi^2|\vec{x}|}\exp\left[\frac{[k_p^2(a_x^2(1-\gamma cos\theta)^2+a_z^2\gamma^2sin^2\theta}{4}\right][C_t(\theta)]^2
\end{aligned} \quad . \quad (3.51)$$

On the following pages we explain and illustrate equations (3.51) for the whole range of θ from $0-\pi$. The variation of $g(\theta)$ for different frequencies is such enormous that it wasn't possible to give all plots the same scaling. a_x, a_z, σ and k are chosen according to the numerical models in chapter 2. We show solutions for three different frequencies, corresponding to the geometrical means of three used butterworth filters ($f_1 = 2.45$ Hz, $f_{10} = 14.54$ Hz, $f_{20} = 27.14$ Hz). These frequencies correspond to the following wave lengths: $\lambda_1 = 2448$ m, $\lambda_{10} = 412$ m and $\lambda_{20} = 221$ m. The standard deviation of the velocity fluctuation is $\sigma = 1$ %. Both, exponential and Gaussian media, are taken into account for four different horizontal correlation lengths ($a_x = 200$ m (isomeric), $a_x = 500$ m, $a_x = 1000$ m, $a_x = 4000$ m) whereas a_z is set constant (200 m). Fig. 3.4 - 3.8 are structured in the same way: Three images on the left side illustrates the scattering coefficient in exponential distributed media and three images on the right side in Gaussian distributed media. From top to bottom three different frequency ranges with certain central frequencies are considered: $f_1 = 2.45$ Hz, $f_{10} = 14.54$ Hz and $f_{20} = 27.14$ Hz. The red line denotes PP scattering, the blue line PS scattering and the broad green line the total scattering coefficient, which is the sum of PP and PS scattering. 0° denotes the forward direction and 180° the backward direction. The incident wave approaches from the left interacts with the heterogeneous zone and a scattered wave is emitted with the illustrated characteristic. Backward directions include angles between 120° and 240° and forward directions include angles between 300° and 60°.

Fig. 3.4: Illustrated is a polar plot of the scattering coefficient $g(\theta)$ in an isomeric medium with $a_x = a_z = 200$ m. We recognise in all cases, (i.e. all three frequency ranges in exponential as well as in Gaussian media) that maximum PP scattering is always oriented in forward and backward direction (i.e. 0° and 180°) and minimum PP scattering always in sidewards direction (i.e. 90° and 270°) whereas PS scattering

is maximal for 45°, 135°, 225° and 315° and is always zero for 0°, 90°, 180° and 270°.

In the f_1 images the wavelength is approximately 2000 m and hence ten times larger than the correlation length. In both f_1 images, exponential and Gaussian, we observe relative to PP scattering stronger PS scattering, except in the forward direction in the Gaussian media where PS and PP scattering are almost equally strong. The scattering coefficient in backward directions is approximately ten times larger than in forward directions.

In the f_{10} case the wavelength is approximately 400 m. We still observe stronger PS scattering in comparison to PP scattering, except in the forward direction in Gaussian media where PP scattering is approximately of the same order as PS scattering. In both media the backward directions are still more dominant than the forward directions. This difference is more distinct in the Gaussian than in the exponential case.

In the f_{20} case the wavelength is approximately 200 m and of the same dimension as the correlation length. We observe the strongest scattering for this frequency range. In the exponential case scattering in forward and backward directions are almost equally strong where PS scattering dominates over PP scattering. In the Gaussian case backward directed scattering is approximately twice as large as forward directed scattering where PP and PS scattering are approximately of the same order.

Fig. 3.5: Only the important differences to Fig. 3.4 are discussed. Illustrated is a polar plot of the scattering coefficient $g(\theta)$ in an anisomeric medium with $a_x = 500$ m and $a_z = 200$ m.

In the f_1 images we recognise the same characteristic as in Fig. 3.4 but g is approximately twice as large.

In the f_{10} case the wavelength is 400 m and approximately of the same dimension as the horizontal correlation length. In the exponential medium forward directed scattering dominates over backward directed scattering whereas in the Gaussian medium backward and forward directed scattering are of the same order.

In the f_{20} case the wavelength is half the size of the horizontal correlation length. Forward scattering is strongly dominant in comparison to backward scattering. PS scattering in forward direction in the exponential case is approximately equally strong compared to PP scattering whereas PP scattering in forward direction in the Gaussian medium is distinctly stronger than PS scattering.

Fig. 3.6: Only the important differences to Fig. 3.5 are discussed. Illustrated is a polar plot of the scattering coefficient $g(\theta)$ in an anisomeric medium with $a_x = 1000$ m and $a_z = 200$ m.

In the f_1 images we recognise the same characteristic as in Fig. 3.5 but in the Gaussian medium g is approximately 50 % larger than in Fig. 3.5.

In the f_{10} case forward oriented scattering dominates in both media where PS scattering dominates in the exponential case and PP scattering slightly dominates in the Gaussian case. The horizontal correlation length is 2.5 times larger than the wavelength.

In the f_{20} case forward scattering is such dominant, that we do not recognise any backscattering with the given scaling. Indeed there is some backscattered energy but it is very small compared to forward scattered energy. In both media PP scattering becomes more dominant in comparison to Fig. 3.5.

Fig. 3.7: Only the important differences to Fig. 3.6 are discussed. Illustrated is a polar plot of the scattering coefficient $g(\theta)$ in an anisomeric medium with $a_x = 4000$ m and $a_z = 200$ m.

In the f_1 images the wavelength is half as large as the horizontal correlation length. Backscattering is not dominant any more. Instead we recognise in the exponential medium an equally distributed PP and PS forward scattering and in the Gaussian medium dominant PP forward scattering and an only slightly smaller PP scattering coefficient in backward direction.

In the f_{10} case forward scattering is strongly dominant in both media where PS scattering dominates in the exponential case and PP scattering in the Gaussian case. Furthermore in both media the forward scattering coefficient is larger than in Fig. 3.6. Interestingly the angle in which PS forward scattering occurs becomes narrower. Therefore PS forward scattering is almost restricted to a direction of approximately 55°. The wavelength is ten times smaller than the horizontal correlation length.

In the f_{20} case the forward scattering coefficient is larger than in Fig. 3.6. The narrowing of the PS forward scattering direction to approximately 55° can be observed, too. The wavelength is 20 times smaller than the horizontal correlation length.

Fig. 3.8: This image show polar plots for heterogeneities with a vertical correlation length of 4000 m and a horizontal correlation length of 200 m. We did not realize such heterogeneities in our numerical models but it

is of general interest how the scattering coefficient behaves under such conditions. It represents a structure similar to vertical dykes.
In the f_1 images we recognise dominant backward directed scattering where PS scattering dominates in the exponential case and PP and PS scattering are of the same dimension in Gaussian media. The wavelength is ten times larger than the horizontal correlation length and half as large as the vertical correlation length.
In the f_{10} case in both media PP scattering absolutely dominates over PS scattering where backscattering is slightly stronger in the exponential case and noticeably stronger in the Gaussian case.
In the f_{20} case the situation is similar to the f_{10} case where forward scattering becomes more dominant. The wavelength is of the same order as the horizontal correlation length.

Overall we recognise:

- PP scattering is generally more dominant in Gaussian media than in exponential media.
- If the wavelength is larger than the horizontal correlation length we observe a tendency to backward directed scattering.
- The largest scattering coefficient in backward directions occur in the isomeric case (i.e. $a_x = a_z = 200$ m) if the wavelength is of the same order as the correlation length.
- If the wavelength is smaller than the horizontal correlation length forward scattering dominates.
- The largest scattering coefficient in forward directions occur in the strongly anisomeric case (i.e. $a_x = 4000$ m and $a_z = 200m$) for wavelengths smaller than the correlation length.
- If the wavelength is of the same order as the horizontal correlation length, forward and backward scattering is balanced in exponential media. The same balancing occurs in Gaussian media for horizontal correlation lengths which are slightly larger than the wavelength.
- For wavelengths much smaller than the horizontal correlation length we observe a narrowing of PS scattering to directions of approximately 55°. In this case scattering can be described by the geometrical optics regime (Fig. 3.1) and the wave propagation can be described by ray

theoretical approaches. This strong conversional forward scattering is visible in the snapshots for anisomeric media in Fig. 2.5 and 2.6 where it is indicated by the angle Θ.

- A change of the vertical correlation length has influences to the scattering coefficient as well.

A comparison of this results with the filtered synthetic seismogram time sections (Fig. 2.15 and Fig. 2.16) yields:

- In all cases where the Born scattering theory predicts small scattering coefficients in backward directions, the deep reflector is visible in the seismogram sections, e.g. in all anisomeric sections and in the isomeric f_1 section. This is true for exponential as well as for Gaussian media.
- A direct comparison between the two f_1 (i.e. exponential and Gaussian) sections in isomeric media supports this statement. The theoretical backscattering coefficient is larger in the exponential medium and the deep reflector is more visible in the Gaussian section.
- Apparently strong forward scattering has no influences on the quality of the deep reflector.

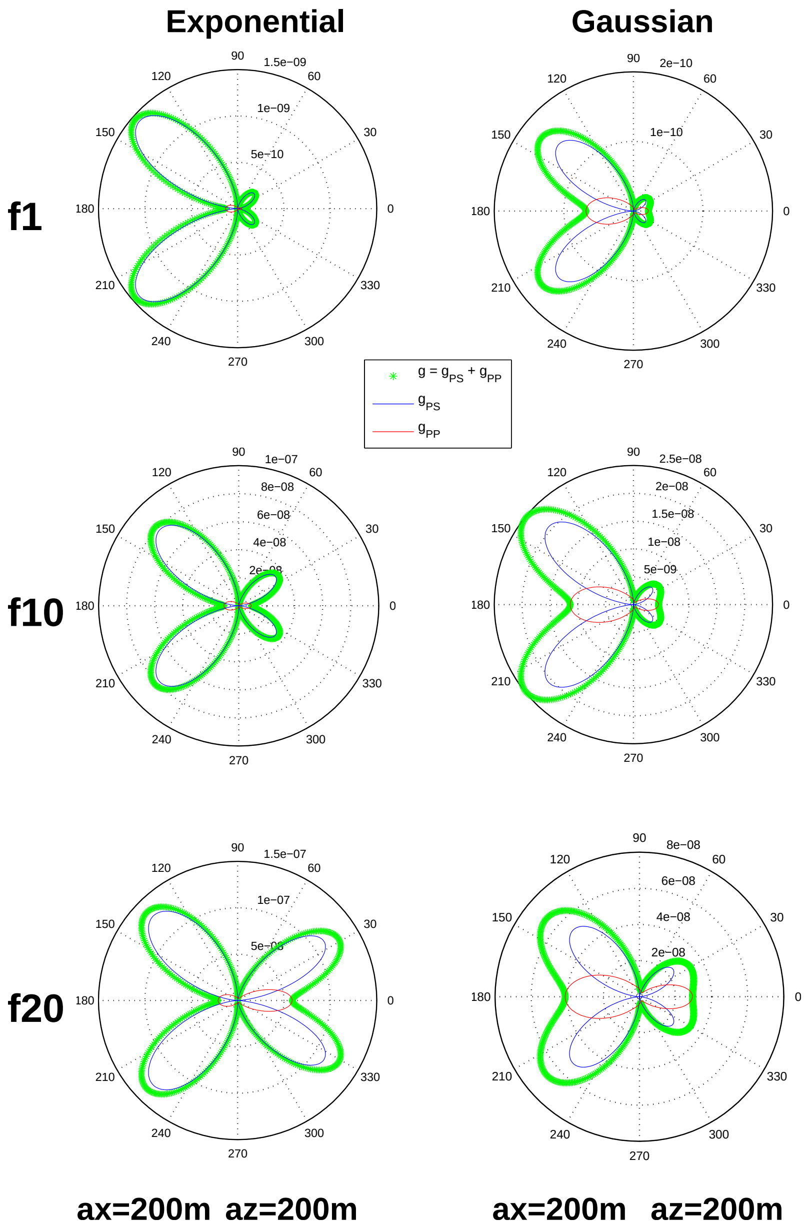

Figure 3.4: Scattering coefficient $g(\theta)$ for exponential and Gaussian media and for three different frequencies corresponding to the geometrical mean of three used band pass filters. This example shows the solution for an isomeric medium with $a_x = 200m$ and $a_z = 200m$ and $\sigma = 1\%$. $0°$ denotes the forward direction. Note that the scaling for the different plots is not equal. The plot corresponds to equations (3.51).

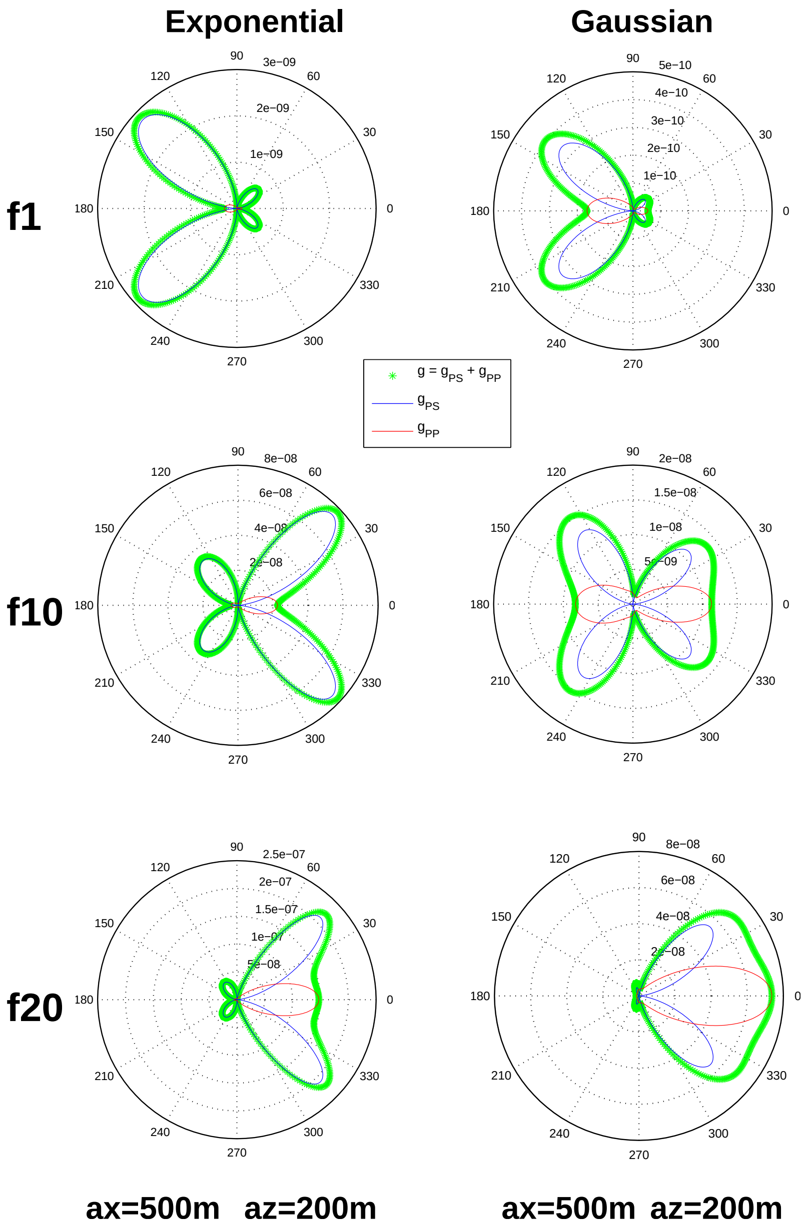

Figure 3.5: Scattering coefficient $g(\theta)$ for exponential and Gaussian media and for three different frequencies corresponding to the geometrical mean of three used band pass filters. This example shows the solution for an anisomeric medium with $a_x = 500m$ and $a_z = 200m$ and $\sigma = 1\%$. 0° denotes the forward direction. Note that the scaling for the different plots is not equal. The plot corresponds to equations (3.51).

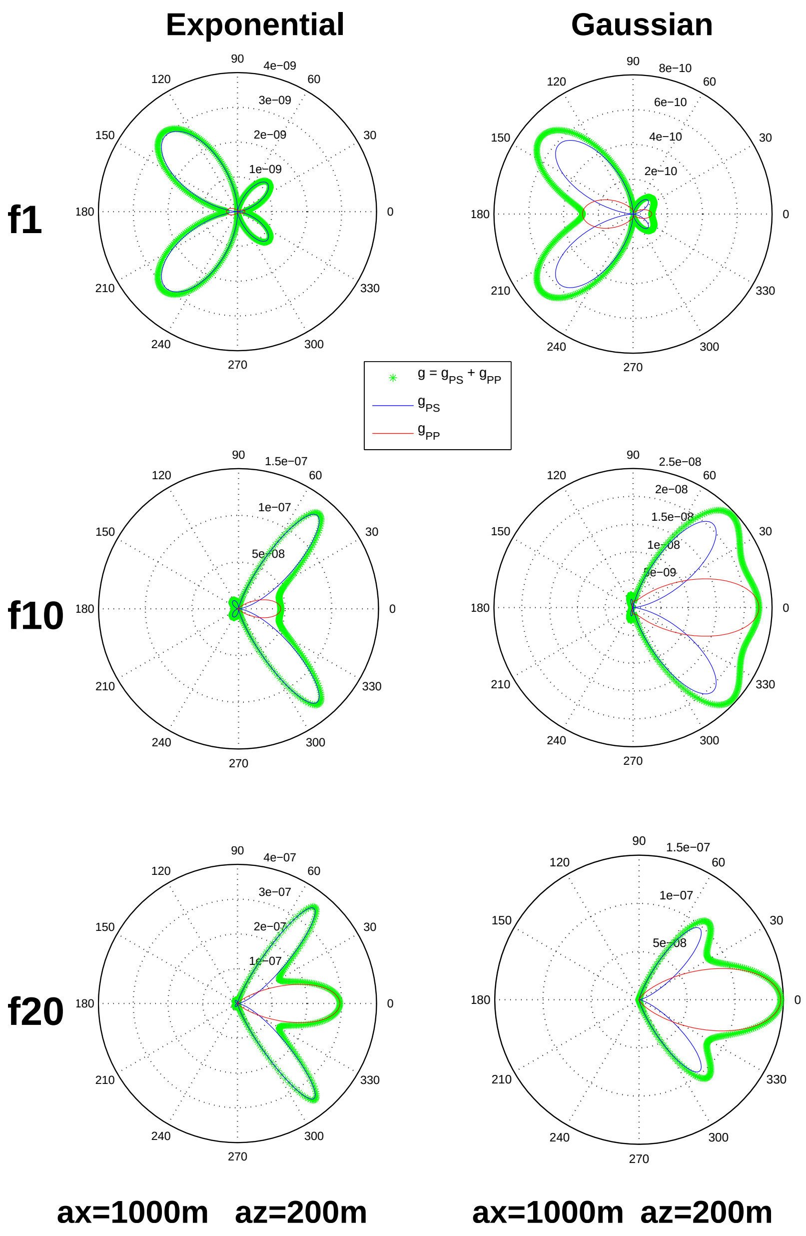

Figure 3.6: Scattering coefficient $g(\theta)$ for exponential and Gaussian media and for three different frequencies corresponding to the geometrical mean of three used band pass filters. This example shows the solution for an anisomeric medium with $a_x = 1000m$ and $a_z = 200m$ and $\sigma = 1\%$. 0° denotes the forward direction. Note that the scaling for the different plots is not equal. The plot corresponds to equations (3.51).

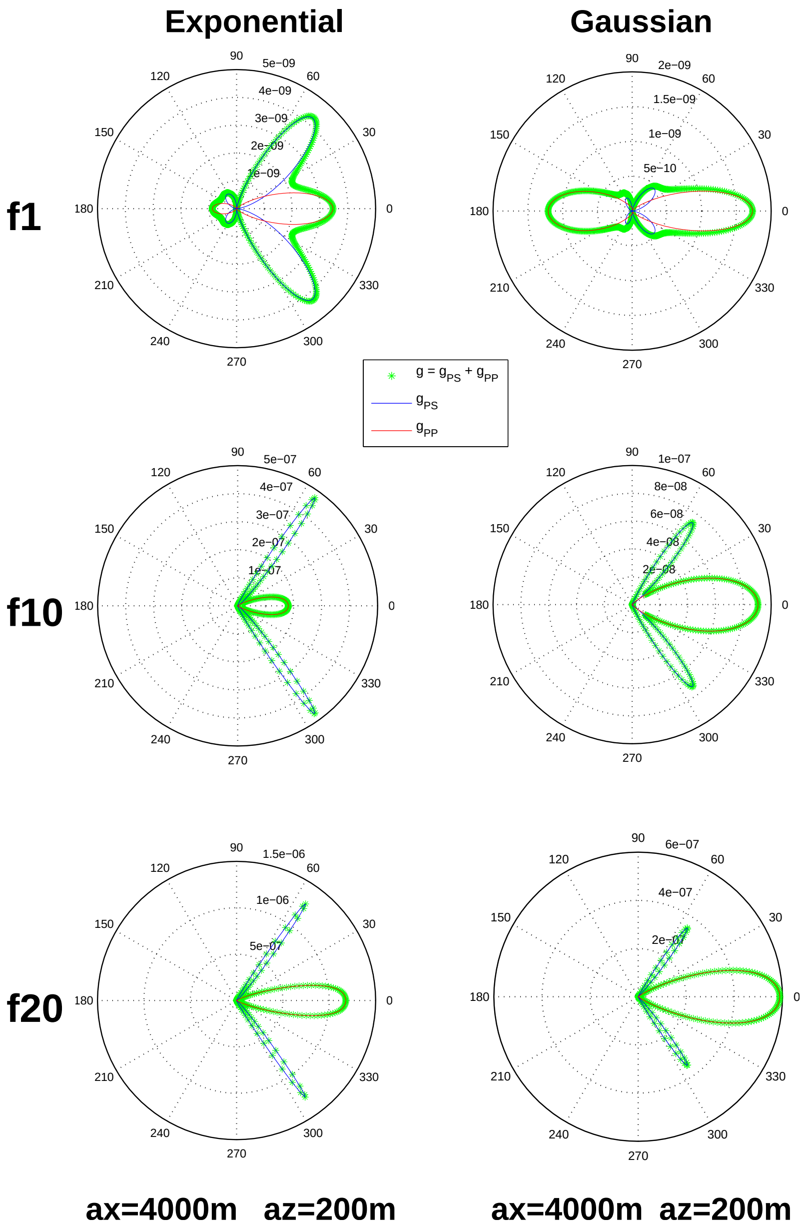

Figure 3.7: Scattering coefficient $g(\theta)$ for exponential and Gaussian media and for three different frequencies corresponding to the geometrical mean of three used band pass filters. This example shows the solution for an anisomeric medium with $a_x = 4000m$ and $a_z = 200m$ and $\sigma = 1\%$. $0°$ denotes the forward direction. Note that the scaling for the different plots is not equal. The plot corresponds to equations (3.51).

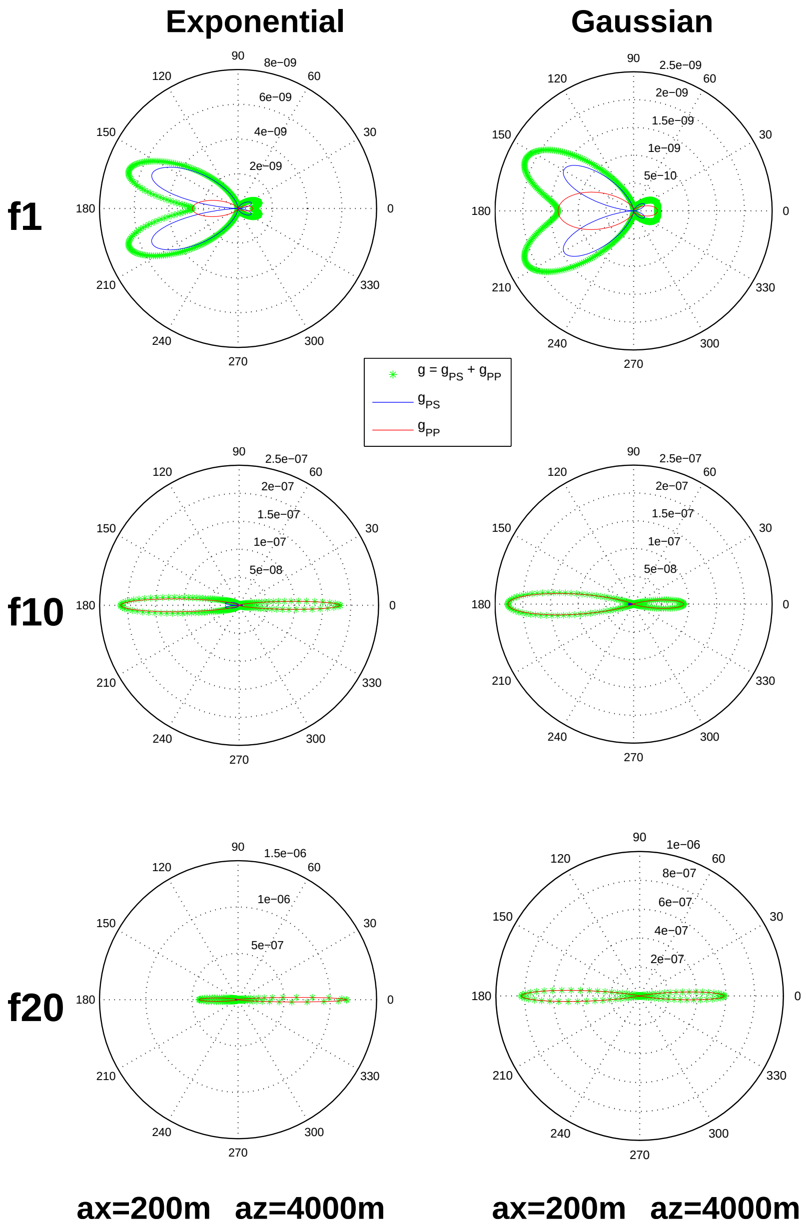

Figure 3.8: Scattering coefficient $g(\theta)$ for exponential and Gaussian media and for three different frequencies corresponding to the geometrical mean of three used band pass filters. This example shows the solution for an anisomeric medium with $a_x = 200m$ and $a_z = 4000m$ and $\sigma = 1\%$. $0°$ denotes the forward direction. Note that the scaling for the different plots is not equal. The plot corresponds to equations (3.51).

3.5 Backscattering coefficient

We assume that the image of the heterogeneous zone only exists due to backscattering, i.e. scattering in a direction with $\theta \approx 180°$. Therefore we set $\theta = \pi$ in equation (3.51) and obtain:

$$\begin{aligned}
\langle |u_r^{PP}|^2 \rangle_{exp}(\pi) &= \tfrac{S k_p^3 \sigma^2 a_x a_z}{(4\pi)^2 |\vec{x}|} \tfrac{1}{[1+4a_x^2 k_p^2]^{\frac{3}{2}}}\, 4K^2 \\
\langle |u_t^{PS}|^2 \rangle_{exp}(\pi) &= 0 \\
\langle |u_r^{PP}|^2 \rangle_{gauss}(\pi) &= \tfrac{S k_p^3 \sigma^2 a_x a_z}{32\pi^2 |\vec{x}|} \exp\left[k_p^2 a_x^2\right] 4K^2 \\
\langle |u_t^{PS}|^2 \rangle_{gauss}(\pi) &= 0
\end{aligned} \tag{3.52}$$

Pure backscattering would not cause conversion scattering. However, we put equation (3.52) into equation (3.7) and obtain:

$$\begin{aligned}
g_\pi(k_p)_{exp} &= \frac{k_p^3 \sigma^2 a_x a_z}{8\pi(1+4a_x^2 k_p^2)^{\frac{3}{2}}}\, 4K^2, \\
g_\pi(k_p)_{gauss} &= \frac{k_p^3 \sigma^2 a_x a_z e^{k_p^2 a_x^2}}{16\pi}\, 4K^2,
\end{aligned} \tag{3.53}$$

where $K \approx 0.78$ and $k_p = \omega / V_0$. The backscattering coefficient for an exponential medium becomes $g_\pi = 8\sigma^2 a_x a_z k^3$, which is constant, for $a_x k \gg 1$. For $a_x k \ll 1$ g_π becomes $\sigma^2 / 2a_x$. The backscattering coefficient for a Gaussian medium has a located maximum at $a_x k = \sqrt{3/2}$. We rewrite equation (3.53):

$$\begin{aligned}
g_\pi(\omega)_{exp} &= \frac{(\omega/V_0)^3 \sigma^2 a_x a_z}{8\pi(1+4a_x^2(\omega/V_0)^2)^{\frac{3}{2}}}\, 9.73, \\
g_\pi(\omega)_{gauss} &= \frac{(\omega/V_0)^3 \sigma^2 a_x a_z e^{(\omega/V_0)^2 a_x^2}}{16\pi}\, 9.73.
\end{aligned} \tag{3.54}$$

These formulas are illustrated in Fig. 3.9. The left image shows the backscattering coefficient for exponential media and four different horizontal correlation lengths ($a_x = 200$ m (blue), $a_x = 500$ m (green), $a_x = 1000$ m (red)

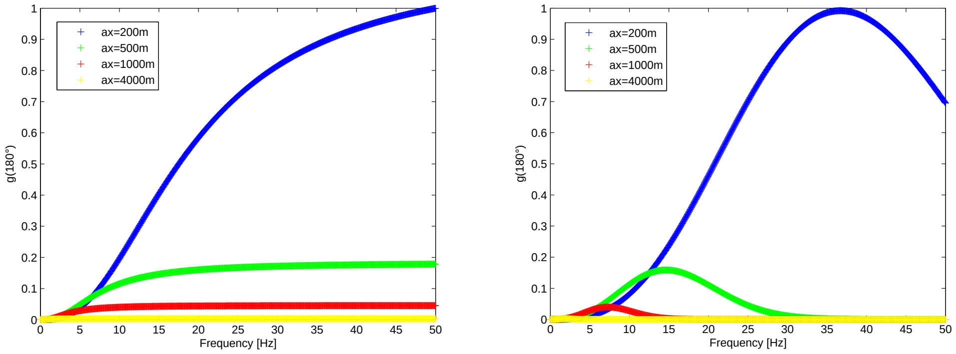

Figure 3.9: Backscattering coefficient $g(\pi)$ for an exponential medium (left) and a Gaussian medium (right) for different horizontal correlation lengths. The plot corresponds to equations (3.54) and is normalised with the maximum of the blue curve.

and $a_x = 4000$ m (yellow)). All four curves increase to higher frequencies and reach a constant maximum from a certain frequency on. This frequency depends on the horizontal correlation length and is as smaller as larger the correlation length is. In low frequency ranges (0-7 Hz) anisomeric media show the largest scattering coefficient. From 7 Hz on the largest backscattering coefficient occurs for isomeric media with $a_x = a_z = 200$ m.
The right image shows the equivalent curves in Gaussian distributed media. We no longer observe a constant maximum but an isolated maximum for a certain frequency, which depends on the horizontal correlation length as well. Again, in low frequency ranges (0-12 Hz) the largest backscattering coefficient occurs for anisomeric media. In high frequency ranges for 12 Hz and more the isomeric medium shows the largest backscattering coefficient. The maximum of the backscattering coefficient is at $a_x = \sqrt{3/2}\,\lambda$.

3.6 Comparison of numerical and analytical results

With the help of the Born scattering theory we wanted to decide how strongly the curves in Fig. 2.25 and Fig. 2.26 are influenced by scattering, in other words how strong A_k and $g(\pi)$ are correlated. It is not necessary to plot both results in one image, as the following differences are obvious.

Comparison between analytical results $g(\pi)$ (chapter 3.6 Fig. 3.9) and numerical results A_k (chapter 2.3 Fig. 2.25) in exponential media:

- The trends of $g(\pi)$ (Fig. 3.9) and A_k (Fig. 2.25) are in the opposite direction. A_k show the smallest values in high frequencies whereas $g(\pi)$ reaches a constant maximum from a certain frequency on.
- The constant maximum of $g(\pi)$ depends on the horizontal correlation length whereas the maximum of A_k is equally located at approximately 5 Hz for all correlation lengths.
- In all frequencies A_k is maximal for larger horizontal correlation lengths, whereas $g(\pi)$ is maximal from 7 Hz on for the smallest correlation length of 200 m.

Comparison between analytical results $g(\pi)$ (chapter 3.6 Fig. 3.9) and numerical results A_k (chapter 2.3 Fig. 2.26) in Gaussian media:

- Both, A_k and $g(\pi)$, show an isolated maximum. The maximum of A_k is located at 5 Hz and is independent on the horizontal correlation length. Whereas the maximum of $g(\pi)$ depends on the correlation length and is at $a_x k = \sqrt{3/2}$.
- Both, largest A_k and largest $g(\pi)$ values, occur in low frequency range in anisomeric media and in high frequency range in isomeric media.
- There is only one intersection point where all curves coincide at approximately 11 Hz for A_k and several intersection points for the different curves of $g(\pi)$.

Interpretation: The scattering coefficient g is a measure for the percentage of scattered energy relative to the energy of an incident wave. If the image of the heterogeneous zone mainly exists due to scattered energy, there should be a correlation between the mean energy in the heterogeneous image and the scattering coefficient g. The following considerations give an explanation why we did not find a correlation:

- The whitening filter (see chapter 2.2.1.) is not accurate enough to equalise all frequencies. Therefore the characteristic of A_k still reflects the spectral influence of the source signal which covers all scattering effects.

- Conventional reflection and transmission is not considered by the scattering coefficient g whereas A_k includes energy caused by such conventional reflections. Especially in the strongly anisomeric case it is probable that reflection dominates scattering.

- It is not well understood how accurate the Born approximation works in the anisomeric case.

Chapter 4

Summary and perspectives

4.1 Summary

The propagation of seismic waves in isomeric and anisomeric random media was studied. A main focus was on the understanding of scattering processes in order to ease the interpretation of RIS seismogram depth sections. For this purpose we performed numerical FD simulations and used common scattering theories to provide an analytical solution of the scattering coefficient.

Numerical studies:
For the computation of synthetic seismogram sections we used models containing a heterogeneous overburden and a deep reflector. The heterogeneous overburden is realized by using either an exponential or a Gaussian, isomeric or anisomeric Auto Correlation Function (ACF). Three parameters determine the characteristics of the overburden: the standard deviation of the velocity fluctuation σ and the horizontal and vertical correlation length a_x and a_z respectively. The ratio of a_x to a_z determines the grade of anisometry. a_z was set to a constant value of 200 m and a_x varied between 200 m in the isomeric media and 6000 m in the strongest anisomeric media. The central frequency of the source signal is about 13 Hz which corresponds in our case to a wavelength of $\approx$ 500 m.

We observed clear and distinct images of the heterogeneous overburden and the deep reflector in seismogram time sections for anisomeric media. In contrast, seismogram time sections in isomeric media show a continuously distributed amount of scattered energy throughout the section. As a consequence the image quality of the deep reflector is bad or it is not visible at all.

Thus, we assume strong disturbing influences due to scattering in isomeric media with heterogeneities of the same magnitude as the wavelength of the propagating wave.

A detailed spectral analysis revealed a self averaging effect in the power spectrum of seismograms recorded in anisomeric media. This is expressed in the decrease of strong spectral fluctuations to higher frequencies. The larger the grade of anisometry is, the smaller the frequencies are for which the spectral fluctuations disappear. Furthermore, the intensity of these spectral fluctuations depends on the standard deviation σ.

In order to interpret the results in terms of frequency we applied the 'Reflection Image Spectroscopy' method to all seismogram sections. Additionally we used a whitening filter to adjust for the spectrum of the source signal. We compared migrated depth sections for different frequency ranges. In migrated sections the deep reflector is no longer covered by energy caused by scattering in the overburden. In anisomeric media the heterogeneous zone and the deep reflector is accurately located and visible in depth sections for all frequencies. In isomeric media we observed the deep reflector in depth sections for low frequency ranges whereas it is not visible in sections containing higher frequencies. In these cases scattering is too strong for a coherent wavefront to reach the deep reflector. It depends on the scale of the heterogeneities, whether a frequency is too "high" or too "low". "Low" includes frequencies with wavelengths much larger than the correlation length and "high" includes frequencies with wavelengths much smaller than the correlation length. Exponential and Gaussian media differ in the sense that the deep reflector is better imaged in Gaussian media.

In order to quantify the RIS depth sections in terms of reflected and backscattered energy emerging from the heterogeneous overburden we determined the average squared amplitude A_k in a defined window in the image of the overburden for every frequency range f_k. A_k increases with the standard deviation of the velocity fluctuation and the grade of anisometry. The plots of A_k over frequency show the same qualitative characteristic for every overburden realization. The observed location of the maximum of A is independent of the horizontal correlation length. This is true for realizations with an exponential or a Gaussian ACF. The characteristic of the plots changes for window sizes smaller than the correlation length. In this case the maximum is shifted to higher frequencies. For all realisations and all window sizes A decreases with increasing frequencies. For an exponential overburden this happens equally for all realizations whereas in a Gaussian overburden the decay depends on the horizontal correlation length. The decay is stronger for anisomeric overburdens.

Analytical studies:
We used a single scattering theory for 2D heterogeneous media described by an ACF, based on the Born approximation in the elastodynamic wave equation to formulate a solution for the scattering coefficient g. The solution is valid for an ensemble average over different realizations of heterogenous media. For the calculation of g we considered PP and PS scattering. The solution states that for low frequencies and isomeric media backscattering is dominant whereas forward scattering is dominant in the case of high frequencies and anisomeric media. As we recorded mainly back propagated waves in our numerical study, we considered the backscattering coefficient g_π separately. For low frequencies g_π is small in the isomeric case whereas for high frequencies the isomeric case is the one with the largest g_π. For exponential media the solution of g_π is constant from a certain frequency on whereas in Gaussian media there is an isolated maximum of g_π. The saturation frequency in an exponential medium or the maximum frequency in a Gaussian medium, depends on the horizontal correlation length i.e. on the grade of anisometry. Although we assumed that the depth image of the heterogeneous zone exists due to backscattered energy, there is no correlation between g_π and A. Apparently the amount of backscattering included in A is to small to visualise it in the way as it was performed in this thesis. Furthermore the Born approximation reaches its limit for high frequencies and large correlation lengths. The validity of the Born approximation for the calculation of g in anisomeric media is still not well understood.

4.2 Perspectives

Maybe this work poses more questions rather than giving answers. Nevertheless I hope this approach and the results may stimulate further research in the following directions.

- Currently it is not possible to extract the scattering strength in heterogeneous media with the help of RIS seismogram depth sections. It is questionable if the amount of scattering is large enough to separate it from all other effects which occur e.g. reflection and transmission, the remaining influence of the source wavelet (after whitening) and further filter effects in the medium. A quantitative comparison of all effects which occur would be of interest.

- It is not well understood how accurate the Born approximation describes the scattering power for anisomeric media. A description with the help of other theoretical methods like the Bourret approximation (e.g. Rytov et al., 1989) or the Rytov approximation (e.g. Ishimaru, 1978) would perhaps lead to further insights.

- We noticed the change of A versus f_k for window sizes smaller than the correlation length. A further study in this direction could provide a method to characterise the medium in terms of correlation lengths. Therefore it is necessary to investigate the changes in more detail.

- The determination of the average energy A for RIS depth sections from real data sets would be of interest.

Bibliography

ANCORP Working Group, 1999, Seismic reflection image revealing offset of andean subduction zone earthquake locations into ocenaic mantle: Nature, **397**, 341–344.

Buske, S., Lüth, S., Meyer, H., Patzig, R., Reichert, C., Shapiro, S., Wigger, P., and Yoon, M., 2002, Broad depth range seismic imaging of the subducted nazca slab, north chile.: Tectonophysics, **350(4)**, 273–282.

Buske, S., Shapiro, S., and Yoon, M., 25 Sept.-1.Oct 2004, Reflection-image-spectroscopy of a subducting plate. Deep Seismix 04, 11th International Symposium on deep seismic profiling of the continents and their margins, 118pp.

Buske, S., 1994, Kirchhoff Migration von Einzelschußdaten: Master's thesis, Johann Wolfgang Goethe - Universität, Frankfurt.

Claerbout, J., 1970, Coarse grid calculations of wave in inhomogenous media with application to delineation of complicated seismic structure: Geophysics, **35**, 407–418.

Gazdag, J., 1978, Wave equation migration by phase-shift: Geophysics, **43**, 1342–1351.

Holberg, O., 1987, Computational aspects of the choice of operator and sampling interval for numerical differentiation in large-scale simulation of wave phenomena.: Geophysical Prospecting, **35**, 629–655.

Hong, T.-K., and Kennet, B., 2003, Scattering attenuation of 2d elastic waves: Theory and numerical modeling using a wavelet-based method: Bull. seism. Soc. Am., **93**, 922–938.

Hong, T.-K., and Wu, R.-S., 2005, Scattering of elastic waves in geometrically anisotropic random media and its implication to sounding of heterogeneity in the earth's deep interior: Geophys. J. Int., **163**, 324–338.

Hudson, J., 1980, The excitation and propagation of elastic waves: Cambridge University Press.

Ishimaru, A., 1978, Wave propagation and scattering in random media: Academic Press Inc., New York.

Levander, A. R., 1988, Fourth-order finite-difference p-sv seismograms.: Geophysics, **53**, 1425–1436.

Ludwig, W., Nafe, J., and Drake, C., 1970, Seismic refraction *in* Maxwell, A., Ed., The Sea:: Wiley-Interscience, 53–84.

Müller, G., Digitale Signalverarbeitung:, lecture notes of the institute for Meteorology and Geophysics of the University Frankfurt, 1994.

Müller, T., 2001, Seismic pulse propagation in statistically heterogeneous geological strucutres: Ph.D. thesis, Freie Universität Berlin.

Press, W., Flannery, B., Teukolsky, S., and Vetterling, W., 1993, Numerical recipes in fortran 77 : The art of scientific computing - second edition: Cambridge University Press.

Roth, M., and Korn, M., 1992, Single scattering theory versus numerical modelling in 2-d random media: Geophys. J. Int., **112**, 124–140.

Rytov, S., Kravtsov, Y., and Tatarskii, V., 1989, Wave propagation through random media, principles of statistical radiophysics, volume 4: Springer, New York.

Saenger, E., 2000, Wave propagation in fractured media: Theory and applications of the rotated staggered finite-difference grid: Ph.D. thesis, Universität Karlsruhe.

Sato, H., and Fehler, M., 1998, Seismic wave propagation and scattering in the heterogeneous earth: Springer-Verlag New York.

Schneider, W., 1978, Integral formulation for migration in two and three dimensions: Geophysics, **43**, 49–76.

Shapiro, S., and Hubral, P., 1999, Elastic waves in random media: Springer-Verlag Berlin-Heidelberg.

Sheriff, R., and Geldart, L., 1999, Exploration seismology: Cambridge University Press.

Sick, C., 2002, Analysis and numerical modeling of seismic wave fields in random media: Master's thesis, Freie Universität Berlin.

Virieux, J., 1986, Velocity-stress finite difference method.: Geophysics, **51**, 889–901.

Wu, R.-S., and Aki, K., 1985, Elastic wave scattering by a random medium and the small-scale inhomogeneities in the lithosphere: J. Geophys. Res., **90**, 10,261–10,273.

Wu, R.-S., and Aki, K., 1988, Scattering and attenuation of seismic waves: Birkhäuser Verlag, Basel.

Yilmaz, O., 1987, Seismic data processing: Society of Exploration Geophysicists.

Yoon, M., 2005, Deep seismic imaging in the presence of a heterogeneous overburden: Numerical modelling and case studies from the central andes and southern andes: Ph.D. thesis, Freie Universität Berlin.

List of Figures

Danksagung

Ich bedanke mich bei Prof. Shapiro für die Möglichkeit meine Diplomarbeit in der Seismikarbeitsgruppe der Fachrichtung Geophysik der FU Berlin durchzuführen.

Desweiteren bedanke ich mich bei Stefan Buske für die Betreuung und das Korrekturlesen meiner Diplomarbeit.

Fachliche und moralische Unterstützung habe ich darüberhinaus von Kolja Groß erhalten. Auch danke ich ihm für das Korrekturlesen einiger Kapitel.

Bei Prof. Kind bedanke ich mich für die Übernahme des Zweitgutachtens.

Erik Saenger stand für Fragen zur FD Modellierung jederzeit zur Verfügung.

Für diverse Anregungen über dir Struktur meiner Arbeit und partielles Korrekturlesen danke ich Susi Rentsch, Carsten Dinske und Maike Buddensiek.

Einen besonderen Stellenwert haben natrlich meine Diplomleidensgenossen Marco Heigel, Florian Karpfinger, Tamara Worcewski, Kirsten Borchardt und Katharina Becker.

Meinen Zimmerkollegen Oliver Gaede und Judith Andersen danke ich für jeden aufheiternden Schwatz.

Meine Kommilitonen Lutz, Dirk und Felix haben stets für Erheiterung und positive Ablenkung von der Arbeit gesorgt, was manche Verzweiflungsstunde am Institut erträglicher machte.

Zu guter letzt aber insbesondere danke ich meinen Eltern, ohne deren Unterstützung mein Studium nicht möglich gewesen wäre.

Erklärung

Hiermit versichere ich, dass ich die vorliegende Arbeit selbstständig verfasst und keine anderen als die angegebenen Hilfsmittel benutzt habe. Die Stellen der Arbeit, die anderen Werken wörtlich oder inhaltlich entnommen sind, wurden durch die entpsrechenden Angaben der Quellen kenntlich gemacht.

Diese Arbeit hat in gleicher oder ähnlicher Form noch keiner Prüfungsbehörde vorgelegen.